

Onset of Spontaneous Imbibition



Master Thesis in Reservoir Physics

by

Tore Lyngås Føyen

Department of Physics and Technology

University of Bergen

June 2016

SUMMARY

The spontaneous imbibition process in porous media is an important recovery mechanism and is governed by capillary forces that arise when two immiscible fluids are present in the pore space. This thesis presents new observations where the displacement process deviates from the widespread assumption of a uniformly shaped saturation front and the square root of time behavior proposed by Washburn. The influence of flow patterns during the onset period, a term used to describe the initial period of spontaneous imbibition, has been studied in different aspects of spontaneous imbibition, such as scaling of results from different systems and measurement of capillary pressure and wettability, in this experimental thesis.

Co-current spontaneous imbibition experiments were performed on sand packed imbibition tubes applying a TEOFSI (Two-Ends-Open Free spontaneous imbibition) boundary condition, with one end face in contact with water and one in contact with oil. The spontaneous imbibition process was unaffected by any onset period for all imbibition tube experiments with a range of fluid viscosities and initial water saturations at strongly water-wet sand, except with an initial water saturation $S_{w,i} = 0.25 \pm 0.01$.

Access to local flow patterns during the onset period was achieved in three different porous systems: unconsolidated sands packed in glass tubes, epoxy-coated two-dimensional paper models, and cylindrical sandstone core plugs. A methodology was developed to compare experimental saturation development data with analytical solutions to investigate their assumptions and validity during the onset period.

Two-dimensional paper models with a limited area open for imbibition showed that conventional one end open scaling groups are suitable in a limited case where the effect from the onset is suppressed due to the total duration of the spontaneous imbibition process. The saturation front in the models transformed as anticipated from the geometrical shaped of the samples.

Positron emission tomography demonstrated the impact of non-uniform wettability in the epoxy-coated core plug, with long induction times and significantly deviating saturation fronts and development. A similar effect was observed using dyed non-wetting phase, to enhance identification of advancing displacement fronts in the packed sand columns. The dye changed wettability locally and resulted in irregular saturation development.

ACKNOWLEDGMENTS

First of all, I would like to express my gratitude to my supervisors Professor Martin Fernø and Dr. Bergit Brattekås at the Department of Physics and Technology at the University of Bergen, for the opportunity to work on an interesting research subject. Thank you for the support, guidance and valuable discussions. In addition, I would like to thank Professor Arne Graue, Associate Professor Geir Ersland and Dr. Marianne Steinsbø for their contributions to the Reservoir Physics group.

A special thanks go to my dear friend and fellow master student Andreas G. Polden, our rivalry, where I am always a step ahead of you is an endless source of motivation. You have ensured my sanity throughout the semester, through entertaining procrastination, and thank you Solveig Carlsen for restricting it and keeping our progress on track.

I would like to thank fellow students in the reservoir physics group for useful discussions, a good atmosphere, and a productive working environment. Thanks to Håkon K. Haugland for willingly sharing experience and knowledge.

Thanks to all my friends contributing to five memorable years at the University of Bergen, several people have contributed to making this a good time and wish you all good luck on the road ahead.

Finally, a special thanks go to my mother and father for the unconditional support and motivation.

Bergen, June 2017

Tore L. Føyen

TABLE OF CONTENTS

Summary	II
Acknowledgments.....	III
Part I. Introduction and Theory	1
1 Introduction	2
2 Fundamentals.....	4
2.1 Pressure acting during spontaneous imbibition	4
2.2 Wettability.....	6
2.2.1 Wettability measurements.....	6
3 Spontaneous imbibition in idealized porous media.....	8
4 Spontaneous Imbibition in Porous Material.....	11
4.1 Direction of flow during spontaneous imbibition	11
4.2 Piston-like flow in porous media.....	12
4.3 Linear counter- current imbibition.....	13
4.4 Radial counter-current imbibition.....	15
4.5 Spherical counter-current imbibition.....	16
4.6 Free spontaneous co-current imbibition	17
5 Boundary Conditions	20
6 Scaling of Spontaneous Imbibition	21
6.1 Dimensionless time	21
6.2 The characteristic length.....	22
6.3 A new scaling group incorporating the effect from varying viscosity	23
7 Onset of Spontaneous Imbibition.....	24
8 Unconsolidated Sand	26
9 Capillary Flow in Paper	28

9.1	Capillary Flow in Paper	28
Part II Methods and Experimental Setups.....		29
10	Preparation of Sand and Fluids.....	30
10.1	Sand preparation and properties	30
10.2	Fluids preparations and properties	31
10.2.1	Wetting fluids	31
10.2.2	Non-wetting fluids.....	32
11	The Imbibition Tube Setup	33
11.1	Preparations of sand pack spontaneous imbibition experiments.....	33
11.2	Permeability measurements and drainage	36
11.3	Pressure in the continuously flushing inlet.	37
11.4	Initiating and measuring the spontaneous imbibition experiments.....	39
12	Transparent Two-Dimensional Porous Models.....	40
12.1	Preparation of the two-dimensional paper models.....	40
12.2	Initiating and measuring spontaneous imbibition into two-dimensional paper models.....	41
Part III Results and Discussion.....		43
13	Overview of the Experiments	44
14	The Porous Media Used in the Experiments.....	47
14.1	The sand packed imbibition tubes	47
14.2	Paper as an analogue to rock material when investigating spontaneous imbibition	48
15	The Saturation Profile and the Saturation Front Shape	50
15.1	The Effect of an Initial Water Saturation on Spontaneous Imbibition.....	52
16	Capillary Pressure and Wettability.	54
16.1	Capillary pressure estimated from free spontaneous imbibition	54
16.2	The effect of wettability on the onset.....	55

17	Developing Saturation Front Shape	58
17.1	The initial radial period of spontaneous imbibition	59
17.2	Transition from a radial to a dragging shaped saturation front.....	61
17.3	Multiple open areas	64
18	The Viscous Resistance Location	66
18.1	Multiple number of limited open areas	70
18.2	Correlations between the transforming saturation front shape and the imbibed area versus time curve	71
19	In-Situ Observations of Limited Open Area Initialization	72
20	Identifying Different Causes for the Onset.....	77
21	The Onset Influencing Scaling of Spontaneous Imbibition	79
21.1	The effect from the onset period in the two dimensional models	80
21.2	Induction times.....	83
Part IV Conclusion and Further Work		85
22	Conclusions	86
23	Future Work.....	87
Part V Appendices and Bibliography		89
Appendix I. Uncertainty Estimation.....		90
Appendix II - Nomenclature and Abbreviations		92
Appendix III Additional Results		94
Bibliography.....		101

PART I. INTRODUCTION AND THEORY

1 INTRODUCTION

Spontaneous imbibition is a displacement process where a non-wetting fluid is displaced out of a porous material by a more-wetting fluid due to capillary actions. Capillary action forms a pressure difference between the two fluids called the capillary pressure. This pressure difference transports the wetting fluid into the porous medium and at the same time expels the non-wetting fluid out of it (Morrow and Mason, 2001) . This process is relevant to numerous practical problems and can be observed in several everyday phenomena, as stain formation on fabrics and absorption of fluids using paper towels (Beuther et al., 2010). On a larger scale, spontaneous imbibition affects multiphase flow in hydrocarbon reservoirs, especially in low-permeability fractured reservoirs, where a major part of the recovery can be a result of spontaneous imbibition (Fernø et al., 2011).

Spontaneous imbibition experiments are often presented as production versus time curves. The shape of the saturation development curve and the duration of the experiments are dependent on sample shape, boundary condition and several rock and fluid properties. Different scaling factors have been suggested to scale production data obtained during spontaneous imbibition experiments with dimensionless time. The scaling groups are based on analytical models assuming piston-like displacement (Schmid and Geiger, 2012). A water-oil displacement is referred to as “piston-like” when the entire saturation change during the displacement occur as a sharp front-define. During a piston-like displacement, the saturation and relative permeability for each of the two phases will be constant on each side of the front, and its therefore simple to derive analytical scaling equations based on the Darcy model (Mason et al., 2009b).

The characteristic length is a parameter representing the effects of the boundary cases, shape, and size of a sample. The characteristic length is calculated from the distance between the open face and the no-flow boundary (Ma et al., 1997). However, the front position is not dependent on the location of the no-flow boundary until it reaches it. The formula used to calculate the characteristic length assumes that the front follows a predetermined trajectory given by the no-flow boundary and shape of the sample as it moves through the sample, and therefore the production can be calculated for an intermediate position (Mason et al., 2009b). It is necessary to scale laboratory spontaneous imbibition data when predicting recovery from hydrocarbon reservoirs, where the recovery mechanism is influenced by spontaneous imbibition.

Some spontaneous imbibition experiments, however, indicate that the trajectory of the frontal advance might not be governed by the sample shape and boundary conditions. The observations indicate that the onset of spontaneous imbibition is unsymmetrical and non-uniform over the surface exposed to the wetting phase, and it exists a period associated with forming and developing the front before the front can be described as piston-like. It might be valuable to separate the imbibition process into two periods, the onset period and piston-like period. The observations include spontaneous imbibition experiments using magnetic resonance imaging performed by (Fernø et al., 2013). The imbibition started from single points at the wetted face, advancing as hemispheres until they merged or reached the cylinder wall and then forming a piston-like shape. The trajectory of the frontal advance was independent of the no-flow boundary until it reached it. Measurements of the capillary pressure acting during spontaneous imbibition were performed by (Li et al., 2009). The pressure measurements

needed a significant period to stabilize, and he proposed that this period might be associated with the forming and development of a stable front.

Induction time is a period of the spontaneous imbibition process where the imbibition does not start immediately after the sample is exposed to the wetting fluid, or the initial imbibition rate is extremely low. No precise and reproducible explanation clarifying this phenomenon has been published (Mason and Morrow, 2013). Some suggestions have been proposed; it might be related to the development of interface curvatures at the open face (Morrow and McCaffery, 1978), extremely low relative permeability at low saturations for the wetting fluid (Behbahani and Blunt, 2005) or local heterogeneities (Mason et al., 2012). The induction time is an important aspect of the onset period, however, with the current understanding and lack of reproducibility, it appears difficult to include it to any model describing the onset period. Backward extrapolation, where the time until the induction period is removed from the dataset, is a conventional method to compensate for the induction time in the production versus time data.

How the existence of an onset period will influence applications of spontaneous imbibition measurements, as scaling, capillary pressure and wettability measurements is the subject of this paper.

2 FUNDAMENTALS

2.1 PRESSURE ACTING DURING SPONTANEOUS IMBIBITION

When a porous material is saturated with two immiscible fluids, there will be a pressure difference between the two fluids called the capillary pressure P_c . This pressure difference occurs due to intermolecular forces between the fluids and the solid surface, contracting the surface of each fluid to a minimum and resulting in a curved interface between the two immiscible fluids. The curvature of the interface is proportional to the pressure difference across the liquid-liquid interface and can be described by Young-Laplace's equation (Shaw, 1992):

$$P_c = \sigma \left(\frac{1}{r_1} + \frac{1}{r_2} \right) \quad (1)$$

,where the curvature of the interface is described by the radii r_1 and r_2 , and σ is the interfacial tension between the fluids. The capillary pressure can be defined as the difference between the non-wetting phase pressure p_{nw} and the wetting phase pressure p_w . (Anderson, 1986a)

$$P_c = p_{nw} - p_w \quad (2)$$

In a small capillary tube, the interface between the two fluids can be described as a part of a sphere with a radius r_s . **Figure 1** shows that the radius of the sphere r_s is larger than the radius of the tube r_t . The contact angle θ relates to the relationship between r_s and r_t .

$$\frac{1}{r_s} = \frac{\cos \theta}{r_t} \quad (3)$$

Substituted r_1 and r_2 with r_s into Young-Laplace's equation (9), gives

$$P_c = \frac{2\sigma \cos \theta}{r_t} \quad (4)$$

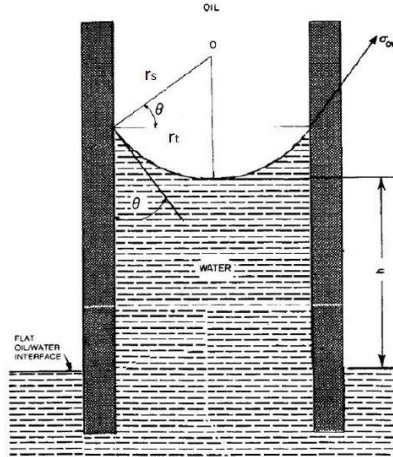


Figure 1: Oil-Water interface in a small capillary tube. From Anderson (1986a)

The capillary pressure at the saturation front $P_{c,f}$ is the governing pressure during spontaneous imbibition. However, another capillary pressure also exists, related to formation of non-wetting droplets during production at a surface covered with the wetting fluids. This is often referred to as the bubble pressure, and in this paper denoted as the capillary back pressure $P_{c,o}$, illustrated in **Figure 2**. The mechanism involved in forming the bubbles is similar to a drainage process, and the non-wetting phase must overcome a threshold pressure to be produced into the wetting liquid (Mason and Morrow, 2013). The capillary back pressure $P_{c,o}$ has been estimated and compared with the front capillary pressure $P_{c,f}$, for brine-oil displacement process in Berea sandstone Li et al. (2006) estimated that the ratio between the oil-water capillary back pressure and the front capillary pressure, $\left(\frac{P_{c,o}}{P_{c,f}}\right)$ from $\left(\frac{1}{9}\right)$ to $\left(\frac{1}{4}\right)$ in Berea sandstone. Fernø et al. (2015b) reported the capillary back pressure in Bentheim sandstone to be $\left(\frac{1}{4}\right)$ of the front capillary pressure. The oil-water capillary backpressure at a surface wetted with the non-wetting phase will be zero. The zero-capillary back pressure at an outlet surface exposed to the non-wetting phase will influence the flow regime during spontaneous imbibition, promoting co-current production (Haugen et al., 2014). The capillary back pressure has been suggested to be the reason for asymmetrical production during spontaneous imbibition into cylindrical cores with two ends open (Mason et al., 2010; Meng et al., 2016).

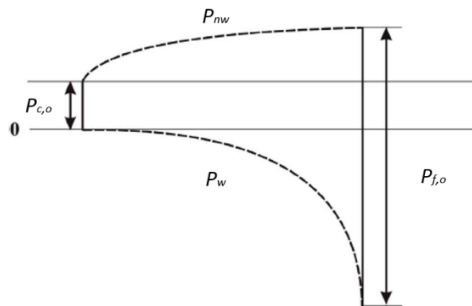


Figure 2: Illustrates the pressure profiles for the wetting fluid P_w and non-wetting fluid P_{nw} during spontaneous imbibition into a core with one end open. The pressure profiles start from the front position, with the front capillary pressure $P_{c,f}$ and end at the wetted face with the capillary back pressure P_{cb} . From Meng et al. (2017).

2.2 WETTABILITY

Wettability is defined as “the tendency of one fluid to spread on or adhere to a solid surface in the presence of other immiscible fluids” (Forrest, 1993). There are several degrees of wettability, varying from strongly water-wet to strongly oil-wet. In a strongly water-wet porous rock, most of the surfaces will be coated with a layer of water, and the smallest pores will be fully saturated with water. In a strongly oil-wet porous rock, oil will saturate the smallest pores, and the surfaces will be coated with oil. Some rock systems show no preference for neither water or oil and are characterized as intermediate or neutrally-wet (Anderson, 1986b). Mixed- and fractional-wet are two additional types of wettability, where the wettability is heterogenic through. In a fractional wet system, the wettability will randomly vary through. In mixed wet, the wettability will be dependent on the pore size (Brown and Fatt, 1956).

Wettability is an important parameter when predicting reservoir behavior, because of its influence on capillary pressure, relative permeability, location, and distribution of the fluids (Anderson, 1986a). McCaffery (1973) and Morrow and McCaffery (1978) studied the effect of wettability on spontaneous imbibition rates into Teflon core plugs, using a range of contact angles between the wetting fluid and the core material. Experiments were performed with and without initial wetting saturation. **Figure 3 (a)** display experiments with zero initial saturation. **Figure 3 (b)** display experiments with 30% initial saturation. As seen in **Figure 3** it is a clear relationship between the wetting strength and imbibition rate for increasing contact angles, i.e., reduced wetting strength the imbibition rate decreased.

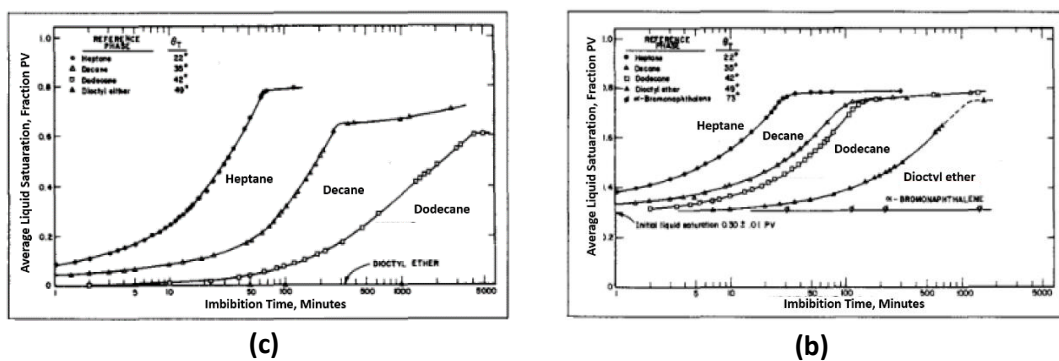


Figure 3: (a) Spontaneous imbibition rate into Teflon cores initially saturated with air for different fluids, with a range of contact angle from 22 to 49 degrees. (b) Spontaneous imbibition rate into Teflon cores with an initial oil saturated of 30% for different fluids, with a range of contact angle from 22 to 73 degrees. Dioctyl with $\theta = 49$ did only imbibe when the core was pre-saturated to 30%. Both figures show spontaneous imbibition time in minutes vs. liquid saturation as fraction of pore volume PV. From Morrow and McCaffery (1978)

2.2.1 Wettability measurements

Two different indices are commonly used to characterize and quantify the average wettability of a porous material: the Amott-Harey index and the USBM index. The Amott-Harvey index compares the volume of fluid produced during spontaneous imbibition and forced imbibition for both phases. The test is performed in four steps: equation (5) gives the Amott oil Indice:

$$\delta_o = \frac{V_{wsp}}{V_{wt}} \quad (5)$$

, where V_{wsp} is the volume of water produced during spontaneous imbibition of oil and V_{wt} is the total volume of water produced, and equation (6) gives the Amott water Index:

$$\delta_w = \frac{V_{osp}}{V_{ot}} \quad (6)$$

, where V_{osp} is the volume of oil produced during spontaneous imbibition and V_{ot} is the total volume of oil produced. The Amott-Harvey index is a combination of the oil and water indices shown in equation (7)

$$I_{AH} = \delta_w - \delta_o \quad (7)$$

For a strongly water-wet system, the index will be close to 1, and for strongly oil-wet it will be close to -1. A disadvantage with the Amott-Harvey index is its ability to determine the wettability for samples that are near neutral wet, as the imbibed volumes will be small (Anderson, 1986a).

The USBM index is more suited for neutral and weakly wetted system. The USBM index compares the area of capillary curves obtained during forced displacement and relates the area of the work needed to displace the fluids. (Donaldson et al., 1969). The wettability can be quantified by contact angle measurements. Several methods have been used, including the sessile drop method, where the contact angle between a drop of oil and the mineral surface is measured (Anderson, 1986a).

3 SPONTANEOUS IMBIBITION IN IDEALIZED POROUS MEDIA

Capillary tubes and capillary tube bundles are simple but useful analogs to porous media and used to investigate the physic involved during spontaneous imbibition. Various geometries have been investigated, the simplest being one single cylindrical tube (Dong et al., 2005). The Hagen-Poiseille equation (8) describes the pressure drop during a laminar flow of a Newtonian fluid in a cylindrical pipe with a constant radius. The equation is valid when: The length of the pipe is substantially longer than the cross-section radius; this ensuring entrance effect negligible; the flow velocity and pipe radius are small enough to prevent turbulent flow, and the flow velocity of the fluid is constant, i.e., no acceleration (Kirby, 2010).

Washburn (1921) combined the Hagen-Poiseille equation (8) and the Young-Laplace's equation (9) to predict the inflow rate during co-current spontaneous imbibition into horizontal capillary tubes. The model was derived from a situation where a viscous fluid displaced a non-viscous fluid, i.e. all of the viscous resistance is in the imbibing wetting fluid. A consequence of this assumption is a linear relationship between the advance of the front and the square root of time.

Washburn equation can simply be derived from the Hagen-Poiseille equation (8) and the Young-Laplace's equation (9):

The Hagen-Poiseille equation (8) gives the pressure drop in the wetting phase ΔP_w in over a length x of a capillary tube with a radius r during flow of the fluid with viscosity μ_w at a rate q_w . The pressure drop ΔP_w in a capillary tube with a radius r during spontaneous imbibition is the capillary pressure P_c , given by the Young-Laplace's equation (9), where σ is the interfacial tension.

$$\Delta P_w = \frac{8\mu_w x q_w}{\pi r^4} \quad (8) \quad \text{Where} \quad \Delta P_w = P_c = \frac{2\sigma}{r} \quad (9)$$

Washburn equation (15) can simply be derived from the Hagen-Poiseille equation (8) by substituting ΔP_w from Young-Laplace's equation (9),

$$\frac{2\sigma}{r} = \frac{8\mu_w x q_w}{\pi r^4} \quad (10)$$

The flow rate q_w equals the advance of the saturation front $\frac{dx}{dt}$ multiplied by the cross-section area A

$$q_w = A \frac{dx}{dt} \quad (11) \quad \text{Where} \quad A = \pi r^2 \quad (12)$$

, for a circular capillary tube. Equation (11) and (12) substitutes for q into equation (10) and gives:

$$\frac{2\sigma}{r} = \frac{8\mu x * \pi r^2}{\pi r^4} \frac{dx}{dt} \quad (13)$$

Solving for the advanced distance x

$$x * dx = \frac{\sigma r}{4\mu} * dT \quad (14)$$

On integration, we get the Washburn equation (15), where the advanced distance of the fluid interface x is equal to the square root of the time:

$$x^2 = \frac{\sigma r}{2\mu} * t \quad (15)$$

The Washburn equation (15) can be expanded to be valid when both phases have a viscosity; if the wetting fluid with viscosity μ_w fills the tube to the front position x , and the non-wetting fluid with the viscosity μ_{nw} fills the tube from the front position x to the end of the tube x_{tube} , we get:

$$(\mu_{nw}(x_{tube} - x) + \mu_w x) dx = \frac{\sigma r}{4} * dT \quad (16)$$

Integrating from $t = 0, x = 0$ to t and x gives

$$\mu_{nw} x_{tube} x - \frac{1}{2} (\mu_{nw} - \mu_w) x^2 = \frac{\sigma r}{4} t \quad (17)$$

Normalizing the equation with respect to the time t_{end} , when the wetting fluid arrives at the end of the tube we get:

$$\frac{1}{2} (\mu_{nw} + \mu_w) x_{tube}^2 = \frac{\sigma r}{4} t_{end} \quad (18)$$

Dividing equation (17) by equation (18) gives.

$$\frac{t}{t_{end}} = \frac{1}{(\mu_{nw} + \mu_w)} \left(2\mu_{nw} \frac{x}{x_{tube}} - (\mu_{nw} - \mu_w) \frac{x^2}{x_{tube}^2} \right) \quad (19)$$

This equation can be used to predict the imbibition rate in experiments where the applications viscosity ratios between the non-wetting and wetting fluid vary. **Figure 4** shows the normalized production versus normalized time during spontaneous imbibition for different viscosity ratios; the spontaneous imbibition rates are the gradients of the curves. When the viscosity of the two fluids is equal, the imbibition rate will be constant, i.e. linearly increasing with time. When the viscosity of the non-wetting fluid is higher than the viscosity of the wetting fluid, the imbibition rate will increase as the front advances, displaying a convex behavior with time. For the opposite case, when the viscosity of the wetting fluid is higher than the viscosity of the non-wetting fluid, i.e. the imbibition rate will decrease as the front advances and has a concave behavior with time. The production rate is proportional to the square root of time if the non-wetting viscosity is zero.

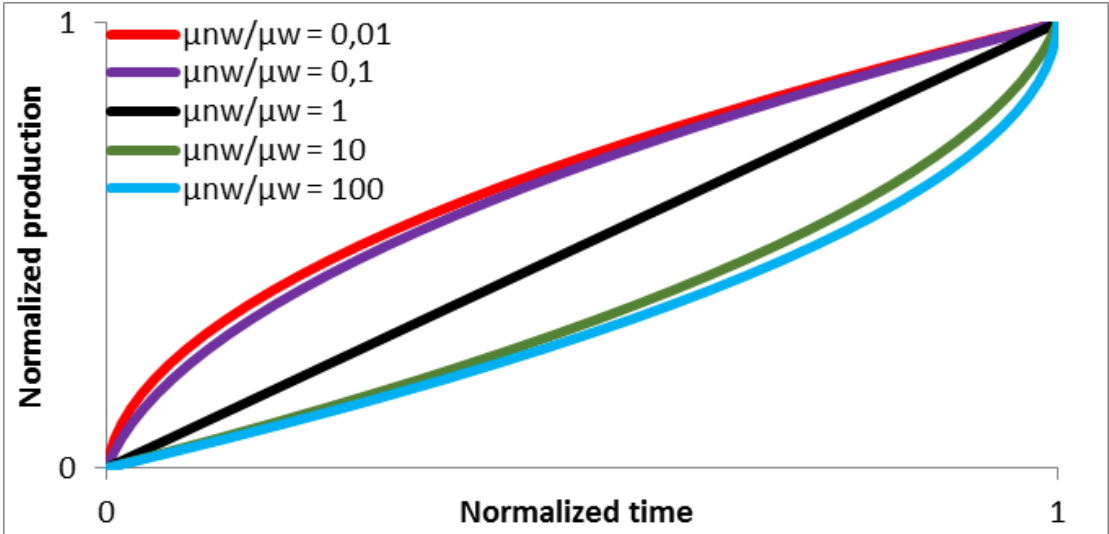


Figure 4: The normalized position of the saturation front plotted as a function of normalized time, calculated using equation (19). The progression of the front is dependent on the viscosity ratio between the two fluids. From Haugland (2016).

4 SPONTANEOUS IMBIBITION IN POROUS MATERIAL

Capillary tube models are able to represent several aspects of spontaneous imbibition (Unsal et al., 2007). However, spontaneous imbibition in porous media shows behaviors not recognized in capillary tubes due to its complexity, including the onset of spontaneous imbibition. It is, therefore, necessary to examine the behavior in porous mediums directly.

4.1 DIRECTION OF FLOW DURING SPONTANEOUS IMBIBITION

Two different flow regimes can exist during spontaneous imbibition, counter-current, and co-current. During counter-current imbibition, the flow direction of the two imbibing and produced fluid fluids is opposite, the non-wetting fluid is displaced out of the sample through the same surface as the wetting fluid imbibes through. During co-current imbibition the two phases are flowing in the same direction, and the non-wetting fluid is produced on a surface that is not exposed to the wetting fluid, i.e. there is no threshold capillary back pressure present at the surface to prevent the flow of the non-wetting fluid.

A common assumption is that the imbibition from fractures to the matrix is counter-current, based on the assumption that surfaces of matrix blocks in real reservoirs completely covered with water during water flooding (Mason and Morrow, 2013). Bourbiaux and Kalaydjian (1990) used different boundary condition to compare co-current and counter-current imbibition, and found that the recovery rate was faster for co-current compared with counter-current imbibition. In one experiment, half-recovery time was 22.2 hours during counter-current imbibition and 7.1 hours during co-current imbibition, using counter-current imbibition data may, therefore, lead to pessimistic recovery estimations if the imbibition is dominated by co-current imbibition. Gravity segregation of the water and oil phase in the fractures may cause the matrix blocks in the oil water contact zone to be exposed to water at the bottom, while the top is exposed to oil. This will lead to a difference in capillary backpressure between the two sides, and oil production towards the top of the matrix blocks, promoting co-current spontaneous imbibition (Pooladi-Darvish and Firoozabadi, 2000). This gravity-segregated situation will be similar to a free spontaneous boundary case, where the inlet side is exposed to brine, and the outlet side is exposed to oil (Haugen et al., 2015). A free spontaneous imbibition boundary occurs when one of the open surfaces of a sample is exposed to the non-wetting phase; the capillary back pressure at this surface will then be zero, promoting co-current spontaneous imbibition to the side in contact with the produced fluid. The pressure profiles during a free spontaneous imbibition boundary case are illustrated in **Figure 5**. Haugen et al. (2014) explains the change from counter-current production to co-current production during a two ends open free spontaneous imbibition boundary case to be associated with the viscous drag of the transport of the fluids and the capillary backpressure. The viscous drag associated with the transport of the wetting fluid from the wetted face to the front is proportional to the distance from the wetted face to the front, and will, therefore increase as the front advances. Simultaneously the viscous drag associated with the transport of the non-wetting fluid towards the face exposed to the non-wetting fluid will decrease. As a higher pressure is necessary to transport the wetting fluid, the pressure in the non-wetting phase will decrease, at one point it will be lower than the bubble pressure at the wetted face causing counter-current production to cease, and

the imbibition becomes purely co-counter. The amount co-current versus counter-current imbibition will be influenced by any difference in mobility between the two phases (Haugen et al., 2015).

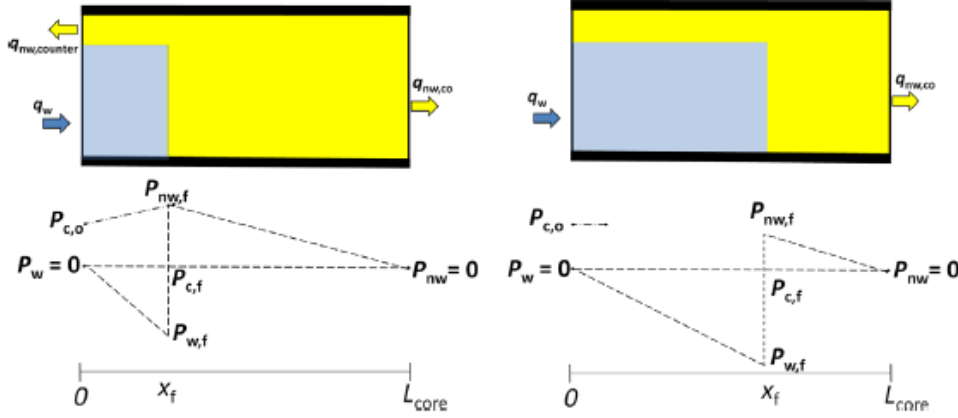


Figure 5: Pressure profiles during piston-like Two Ends Open Free Spontaneous Imbibition. Left: Combined counter-current and co-current imbibition. Right: Pure Co-current imbibition. (Haugen et al., 2014)

4.2 PISTON-LIKE FLOW IN POROUS MEDIA

Analytical models for counter-current spontaneous imbibition with a piston-like saturation front based on Darcy's law were derived by Mason et al. (2009b). The wetting and non-wetting phase relative permeability and capillary pressure function are necessary when describing fluid flow during spontaneous imbibition. The functions can be simplified into single values behind and ahead of the saturation front during a piston-like displacement, where the saturation change occurs in one step from a low water saturation $S_{w,l}$ to the saturation after spontaneous imbibition $S_{w,sp}$.

Mason et al. (2009b) and Mason et al. (2012) derived analytical models for counter-current spontaneous imbibition based on Darcy's law for flow of the wetting q_w and non-wetting phase q_{nw} :

$$q_w = -\frac{Kk_{r,w}A}{\mu_w} \frac{\partial P_w}{\partial x} \quad (20)$$

Where K is the absolute permeability, $k_{r,w}$ is the wetting phase relative permeability, μ_w is the wetting phase viscosity, $\frac{\partial P_w}{\partial x}$ is the wetting phase pressure gradient and A is the cross-sectional area.

And,

$$q_{nw} = -\frac{Kk_{r,nw}A}{\mu_{nw}} \frac{\partial P_o}{\partial x} \quad (21)$$

where $k_{r,nw}$ is the non-wetting phase relative permeability, μ_{nw} is the non-wetting phase viscosity and $\frac{\partial P_o}{\partial x}$ is the non-wetting phase pressure gradient. The capillary pressure is the pressure difference between the two phases given by equation (2). The conservation of volume during flow of incompressible fluids gives that the flow of the two fluids at both sides of the saturations front are equal

$$q_w = -q_{nw} \quad (22)$$

Combining equation (2), (20), (21) and (22) gives:

$$q_w = \frac{K k_{r,w} k_{r,nw} A}{\mu_w k_{r,nw} + \mu_{nw} k_{r,w}} \frac{\partial P_c}{\partial x} \quad (23)$$

A part of this equation can be simplified into the mobility factor M from the assumption of constant saturations and relative permeability behind the front:

$$M = \frac{K k_{r,w} k_{r,nw}}{\mu_w k_{r,nw} + \mu_{nw} k_{r,w}} \quad (24)$$

The Darcy velocity the wetting fluid behind the front can be simplified to

$$q_w = KMA \frac{\partial P_c}{\partial x} \quad (25)$$

The piston-like flow defined in equation (25) is valid for all sample shapes and boundary conditions. The rate of the advancing saturation front $\frac{dx}{dt}$ is given by volumetric imbibition rate q_w and surface area of saturation front. When deriving equations that predict the fractional production versus time, it is necessary to use expressions describing the relationship between the advance of the saturation front and the volumetric imbibition rate q_w . For a linear, radial and spherical imbibition it is straightforward to find suitable expressions describing this relationship.

4.3 LINEAR COUNTER- CURRENT IMBIBITION

The surface area of the saturations front A_f is constant and equal to the cross-sectional area during a linear displacement, and the rate of the advancing saturation front $\frac{dx}{dt}$ is therefore proportional to the volumetric imbibition rate q_w :

$$\frac{dx}{dt} = \frac{q_w}{A_f \varphi (S_{w,f} - S_{w,spi})} \quad (26)$$

, where φ is the porosity, $S_{w,l}$ is the low water saturation ahead of the saturation front and $S_{w,sp}$ is the water saturation behind the saturation front.

Equation (25) can be integrated from the open face to the front:

$$q_w(x - 0) = KMA(P_{c,f} - P_{c,o}) \quad (27)$$

Where $P_{c,f}$ is the capillary pressure at the front, and $P_{c,o}$ is the capillary backpressure at the open face. During linear imbibition the cross-sectional area A is constant.

Substituting for q_w in equation (27), using equation (26) and integrating gives:

$$x^2 = \frac{2KM(P_{c,f} - P_{c,o})}{\varphi(S_{w,sp} - S_{w,l})} t \quad (28)$$

Let the time $t = 0$ be when the front is at the open face. If f is the normalized production at the time t , then $f = x/L$, where L is the core length. This gives:

$$f^2 = \frac{2KM(P_{c,f} - P_{c,o})}{L^2 \varphi(S_{w,sp} - S_{w,l})} t \quad (29)$$

The difference in capillary back pressures and capillary pressure can be substituted with:

$$C_{spread} 2\sigma \sqrt{\frac{\varphi}{8K}} \quad (30)$$

The capillary pressure is assumed to be equal to the capillary pressure in a tube, where the mean radius is given by the relationship between the permeability and porosity proposed by Leverett (1941). C_{spread} , represent the pore size distribution.

Rearranging equation (29) and using the substitution in equation (30) gives the normalized production at a normalized time t_f :

$$t_f = \sqrt{\frac{\varphi}{2K} \frac{S_{w,sp} - S_{w,l}}{MC_{spread}\sigma}} L^2 f^2 \quad (31)$$

,where the normalized time t_f is given by the time t and the time when spontaneous imbibition ceases t_{end} :

$$t_f = \frac{t}{t_{end}} \quad (32)$$

This equation predicts the time for a fractional production f during one-dimensional spontaneous imbibition from a sample with the length L . The model predicts that the fractional production will be proportional to the square root of time. The scaling factor for a linear one-dimensional spontaneous imbibition is given by this equation when $f = 1$.

Similar derivations were performed for radial and spherical imbibition. The main difference in the derivations is that the area of the front A_f will be a function of the front position r . r replaces the front position x . For convenience, only the result of the derivation for the radial and spherical displacement is presented in this paper. The complete derivations can be found in Mason et al. (2009b) and Mason et al. (2012). The analytical Darcy models are used in the analysis of how different saturation front shapes observed during the onset spontaneous imbibition affects the rate of spontaneous imbibition.

4.4 RADIAL COUNTER-CURRENT IMBIBITION

The saturation front area for radial spontaneous imbibition A_r , is given by the length of the core L_{core} and position of the saturation front r :

$$A_r = 2\pi r * L_{core} \quad (33)$$

Substituting the saturation front area A in equation (25) with the radial saturation front area A_r gives the wetting phase flow rate $q_{w,r}$:

$$q_{w,r} = -KM2\pi r * L_{core} \frac{\partial P_c}{\partial r} \quad (34)$$

, where $\frac{\partial P_c}{\partial r}$ is the pressure gradient.

The rate of the advancing saturation front $\frac{dr}{dt}$ is given by the volumetric imbibition rate q_w :

$$\frac{dr}{dt} = \frac{q_{w,r}}{2\pi r L_{core} \phi (S_{w,sp} - S_{w,l})} \quad (35)$$

The two equations (34) and (34) can be applied in a similar derivation as for the linear case:

$$t_{f,Mason} = \frac{1}{2} \sqrt{\frac{\phi}{2k} \frac{S_{w,sp} - S_{w,l}}{MC_{spread}\sigma}} (R_{open}^2 + 2r^2 \ln \frac{r}{R_{open}} - r^2) \quad (36)$$

Equation (36) predicts when the wetting front arrives at the closed boundary during radial counter-current imbibition. The equation is valid during both inward and outward imbibition: For inward imbibition $R_{open} > R_{closed}$ and $R_{open} < R_{closed}$ for outward imbibition.

4.5 SPHERICAL COUNTER-CURRENT IMBIBITION

The saturation front area for radial spontaneous imbibition A_s , is given by position of the saturation front r

$$A_s = 4\pi r^2 \quad (37)$$

Substituting the saturation front area A in equation (25) with the spherical saturation front area A_s gives the wetting phase flow rate $q_{w,s}$:

$$q_{w,s} = KM4\pi r^2 \frac{\partial P_c}{\partial r} \quad (38)$$

, where $\frac{\partial P_c}{\partial r}$ is the pressure gradient.

The rate of the advancing saturation front $\frac{dr}{dt}$ is given by the volumetric imbibition rate $q_{w,s}$:

$$\frac{dr}{dt} = \frac{q_{w,s}}{4\pi r^2 \phi (S_{w,f} - S_{w,spi})} \quad (39)$$

The two equations (38) and (39) can be applied in a similar derivation done for the linear and radial case:

$$t_{f,Mason} = \frac{1}{3} \sqrt{\frac{\varphi}{2k}} \frac{S_{w,sp} - S_{w,l}}{MC_{spread}\sigma} (2 \frac{r^3}{R_{open}} - 3r^2 + R_{open}^2) \quad (40)$$

Equation (40) predicts when the wetting front arrives at the closed boundary during spherical counter-current imbibition. The equation is valid during both inward and outward imbibition: For inward imbibition $R_{open} > R_{closed}$ and $R_{open} < R_{closed}$ for imbibition outward .

During radial and spherical imbibition where the aspect ratio between R_{closed} and R_{open} is greater than 5, the imbibition rate will be close to linear with time. This is because most of the resistance to flow will be close to the open face (Mason et al., 2012).

4.6 FREE SPONTANEOUS CO-CURRENT IMBIBITION

A set of equations describing co-current displacement during spontaneous imbibition into a porous media applying Two Ends Open Free Spontaneous Imbibition boundary conditions (TEOFSI) was developed by Haugen et al. (2014). As for counter-current imbibition, Darcy's law can be used to describe the flow of the two fluids. The pressure drop for a free spontaneous co-current imbibition boundary case is described in equation (41) and (42) and differs from the pressure drop during linear counter-current spontaneous imbibition, the right-hand side of equation (23). **Figure 5** illustrates the pressure drop during TEOFSI. The following Darcy equations will be valid when the pressure drop in the non-wetting phase towards the inlet side exposed to the wetting fluid is zero, i.e. pure co-current imbibition.

$$q_w = - \frac{Kk_{rw}A}{\mu_w} \frac{(P_{w,f} - 0)}{(x - 0)} \quad (41)$$

$$q_{nw} = - \frac{Kk_{rnw}A}{\mu_{nw}} \frac{(0 - P_{nw,f})}{(L - x)} \quad (42)$$

, where x is the front position measured from the surface exposed to the wetting fluid. The saturation change occurs over the front only, resulting in the endpoint saturation and associated endpoint relative permeability k_{rw} and k_{rnw} .

Combining Darcy equation (41) and (42) with the rate of the advancing saturation front for a one-dimensional displacement equation (26), and the requirement of equal flow of the two phase equation (22) gives:

$$\frac{x^2}{L^2} + 2 \frac{\mu_{nw}/k_{nw}}{\left(\left(\mu_w/k_w\right) - \left(\mu_{nw}/k_{nw}\right)\right)} \frac{x_f}{L} = \frac{2KP_{c,f}}{\varphi L^2(S_{w,sp} - S_{w,l})} \frac{1}{\left(\left(\mu_w/k_w\right) - \left(\mu_{nw}/k_{nw}\right)\right)} t \quad (43)$$

The pressure drop ahead of the saturation front is given by equation (44), based on the pressure drop in **Figure 5**:

$$\frac{P_{nw,f}}{P_{c,f}} = \frac{1}{1 + (k_{nw}/\mu_w)(\mu_w/k_w) \left(1/(L/x) - 1\right)} \quad (44)$$

Define a variable D to represent the following expression

$$D = \left(\frac{1}{((k_{nw}/\mu_w)(\mu_w/k_w) - 1)} \right) \quad (45)$$

, the variable D simplifies equation (43)

$$\frac{x^2}{L} + 2D \frac{x}{L} + D^2 = D^2 + \frac{2KP_{c,f}}{\varphi L^2(S_{w,sp} - S_{w,l})} \frac{1}{\left(\left(\mu_w/k_w\right) - \left(\mu_{nw}/k_{nw}\right)\right)} t \quad (46)$$

Define a new variable E to represent the following expression

$$E = \frac{2KP_{c,f}}{\varphi L^2(S_{w,f} - S_{w,sp})} \frac{1}{\left(\left(\mu_w/k_w\right) - \left(\mu_{nw}/k_{nw}\right)\right)} \quad (47)$$

, the two variables D and E simplifies equation (46):

$$\left(\frac{x}{L} + D\right)^2 = D^2 + Et \quad (48)$$

D And E will be constants during a single displacement.

Equation (48) can be rewritten to:

$$\frac{x}{L} = \sqrt{D^2 + Et} - D \quad (49)$$

Equation (49) gives the expected front position x at a given time t . The calculated front positions can be plotted versus a set of experimental measured front positions. The value of D and E can be determined by fitting the values such that this plot will be linear with a gradient of unity, and the two variables D and E used to predict unknown parameters. The front capillary pressure $P_{c,f}$ can be estimated from the variable E , and the wetting phase relative permeability behind the saturating front can be estimated from variable D .

$P_{c,f}$ can be calculated using

$$P_{c,f} = E * \left(\frac{\mu_w}{k_w} - \frac{\mu_{nw}}{k_{nw}} \right) \frac{\phi L^2 (S_{wf} - S_{wi})}{2K} \quad (50)$$

k_w can be calculated using

$$k_w = \left(\frac{D \mu_w (k_{nw} / \mu_w)}{D + 1} \right) \quad (51)$$

5 BOUNDARY CONDITIONS

The boundary condition will determine the duration and shape of the production versus time curve (Mason et al., 2009b). Spontaneous imbibition experiments are usually performed on cylindrical core samples. The most common boundary condition is “All Faces Open” (AFO), where the core plug is unsealed and all faces exposed to the wetting fluid (Mason et al., 2009a). This boundary condition is simple to prepare, and the experiments are easy to perform and give reproducible results. However, it is complicated to model and describe the imbibition processes with differential equations due to a complex flow pattern, including both linear and radial co-current and counter-current imbibition (Mason et al., 2009a). A characteristic length for AFO is presented in **Table 1**.

Commonly used boundary conditions on cylindrical cores are Two Ends Closed (TEC), One End Open (OEO) and Two Ends Open (TEO), where some of the core faces are sealed, and others open to imbibition and production. Both OEO and TEO boundary conditions will promote linear piston-like imbibition that can be described with differential equations (Meng et al., 2015). Imbibition into core plug applying OEO boundary conditions will be purely counter-current. Imbibition into a core plug applying TEO boundary conditions was assumed to be similar to imbibition into two OEO cores acting independently. However: spontaneous imbibition experiments performed by Mason et al. (2010) showed a unpredicted behavior: the volume of water imbibed at each open side was equal and proportional to the square root of time, however; the volume of oil produced from the two sides was asymmetrical. A symmetrical development of the water saturation around the center of the core was confirmed from in situ imaging. In situ imaging is a valuable tool when investigating spontaneous imbibition as it is possible to determine the position and shape of the saturation front and observe the developing saturation profile. The saturation profile is the curve representing the water saturation over the length of the core sample at a time t .

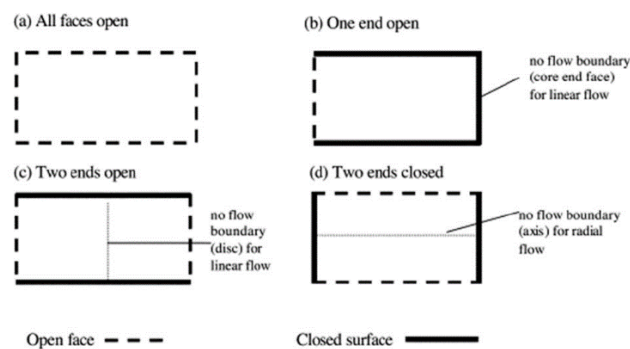


Figure 6: Illustrating different boundary conditions used for core samples (Morrow and Mason, 2001).

Two End Open Free Spontaneous Imbibition (TEOFSI) is a boundary case where one end of the core plug is exposed to the wetting phase while the other end is exposed to the non-wetting phase. At the side exposed to the non-wetting phase, the capillary back pressure will be zero, and this will promote co-current production. In experiments applying this boundary condition, oil production has been observed from both open faces. Initially, most of the production occur counter-currently, i.e. to the side exposed to brine. As the front progresses towards the side exposed to oil, the amount of co-current oil production increases while the amount of counter-current oil production decreases (Bourbiaux, 2009; Haugen et al., 2014).

6 SCALING OF SPONTANEOUS IMBIBITION

Using spontaneous imbibition laboratory data to predict reservoir production performance, and identifying conditions for when spontaneous imbibition data can be scaled as well as suitable correlation, is not straightforward and a topic investigated by several authors (Morrow and Mason, 2001). Early work by Mattax and Kyte (1962) incorporates fluid and rock properties into a scaling group for the dimensionless time. This scaling group and modifications are presented in this chapter.

6.1 DIMENSIONLESS TIME

The scaling group for dimensionless $t_{D,MK}$, proposed by Mattax and Kyte.

$$t_{D,MK} = Ct \sqrt{\frac{K \sigma}{\varphi \mu_w L_s^2}} \quad (52)$$

, where K is the permeability (mD), φ is the porosity, μ_w (cP) is the wetting phase viscosity, σ ($\frac{\text{dyn}}{\text{cm}}$) is the interfacial tension, t is the time in minutes, and L_s (cm) is the characteristic length. The constant C is 0.018849 when the proposed units in parenthesis are used.

$\sqrt{\frac{k}{\varphi}}$ is given by the Leverett microscopic radius (Leverett, 1941),

Mattax and Kyte's scaling group is useful when comparing experimental results from samples with different size. However, it can only be applied when the following conditions are met:

- 1) The shape and boundary conditions are equal between samples.
- 2) Oil -Water viscosity ratios are equal.
- 3) The effect of gravity is insignificant.
- 4) The initial saturation and distribution of the fluids are equal in all experiments.
- 5) The capillary pressure functions are proportional.
- 6) Similar relative permeability functions.

6.2 THE CHARACTERISTIC LENGTH

The characteristic length L_S is given by the shape factor F_S (Kazemi et al., 1992):

$$L_S = \frac{1}{\sqrt{F_S}} = \sqrt{\frac{V_b}{\sum_{i=1}^n \frac{A_i}{S_{A_i}}}} \quad (53)$$

Where n is the number of surfaces open to imbibition, A_i is the area of the open surface in direction i , S_{A_i} is the distance from surface A_i to the center of the sample and V_b is the bulk volume of the sample. The shape factor takes into account that the flow out of the sample is dependent on the ratio between the sample volume and total open surface area (Zhang et al., 1996). A modified characteristic length L_C was proposed by Ma et al. (1997), which accounts for the actual distance l_{A_i} the imbibition front travels from the open surface to the no-flow boundary. This made it possible to scale and compare samples with different shape and boundary condition. Using equation (54) the characteristic length is calculated from the front position at the time t_{end} , when the front arrives at the no-flow boundary. However, the front position is not dependent on the location of the no-flow boundary until it reaches it. The calculation of the characteristic length factor is based on the assumption that the saturation front follows a trajectory given by the position of the open faces and the no-flow boundaries. The intermediate saturation front position is therefore predetermined (Mason et al., 2009b).

The modified characteristic length L_C is defined as:

$$L_C = \sqrt{\frac{V_b}{\sum_{i=1}^n \frac{A_i}{l_{A_i}}}} \quad (54)$$

An overview of the characteristic length for different boundary cases, giving different flow regimes are presented in **Table 1**. The TEO, TEC, OEO and AFO characteristic length is derived Zhang et al. (1996). The characteristic length for the radial and spherical boundary case are derived by Mason et al. (2012). The four boundary cases are defined in **Figure 6**.

Table 1: Overview of different characteristic length L_c for different boundary cases and the flow regimes.

Boundary case	Flow regimes	Characteristic length, L_c
TEO	Linear	$L_c = L_s$
TEC (Radial inward)	Radial	$L_c = \frac{d}{2\sqrt{2}}$
OEO	Linear	$L_c = \sqrt{2}L_s$
AFO	Complex	$L_c = \frac{L_s d}{2\sqrt{d^2 + 2L_s^2}}$
Radial inward and outward	Radial	$L_c^2 = \frac{1}{2}(R_{open}^2 + 2R_{closed}^2 \ln \frac{R_{closed}}{R_{open}} - R_{closed}^2)$ For inward, $R_{open} < R_{closed}$
Spherical inward and outward	Spherical	$L_c^2 = \frac{1}{3}(2\frac{R_{closed}^3}{R_{open}} - 3R_{closed}^2 + R_{open}^2)$ For inward, $R_{open} < R_{closed}$

6.3 A NEW SCALING GROUP INCORPORATING THE EFFECT FROM VARYING VISCOSITY

Figure 4 shows the effect of viscosity ratios on productions curves during spontaneous imbibition into an idealized porous media. The production curves are calculated using the Washburn equation. It is clear that both the viscosity and the viscosity ratio between the fluids will greatly influence the scaling of the production data. The geometrical mean of the water and oil viscosities was applied to the scaling group by Ma et al. (1995). The modified scaling group was validated numerically and gave satisfactory results for fluid-fluid viscosity ratios, although, it was not suitable for gas-fluid viscosity ratios (Behbahani et al., 2006).

The geometrical mean viscosity μ_{gm} is defined as:

$$\mu_{gm} = \sqrt{\mu_{nw} * \mu_w} \quad (55)$$

Ma et al. (1997) combining the modified characteristic length L_c and the geometrical mean μ_{gm} to a new generalized scaling group for the dimensionless time: This scaling group eliminates condition 1 and 2 from the original scaling group: the requirements for duplicated core sample shape and boundary conditions and equal oil-water viscosity ratio.

The new scaling group for dimensionless time proposed by (Ma et al., 1997):

$$t_{D,MMZ} = Ct \sqrt{\frac{k}{\phi} \frac{\sigma}{\sqrt{\mu_{nw} * \mu_w}} \frac{1}{L_c^2}} \quad (56)$$

7 ONSET OF SPONTANEOUS IMBIBITION

The onset of spontaneous imbibition is the initial period of the displacement process. During this period several phenomena have been observed that contradict the assumed models and described the displacement process. For simplicity, the phenomena can be categorized into three categories.

1. Induction time before any spontaneous imbibition is measurable (Graue et al., 2002; Mason and Morrow, 2013).
2. Asymmetric production of the non-wetting phase from cores with two ends open (Mason et al., 2010; Meng et al., 2016).
3. Non-uniform initialization and the initial trajectory of the front (Baldwin and Spinler, 2002; Fernø et al., 2013; Wickramathilaka et al., 2010).

This paper will mainly focus on the initial front development (3) and inductions time (1).

Capillary pressure measurements during spontaneous imbibition into an OEO boundary core was performed by (Li et al., 2009). A period was necessary before the pressure reading stabilized; the suggested explanation for this period was the forming and development of a stable front. Fernø et al. (2013), Wickramathilaka et al. (2010) and Baldwin and Spinler (2002) used magnetic resonance imaging (MRI) to visualize the saturation front during respectively OEO, TEO and AFO spontaneous imbibition boundary conditions. Their experiments contradicted the general assumption of a uniform shaped saturation front, and a non-uniform initialization and initial trajectory of the saturation front was observed. The initial movement of the saturation front was described as *circle segment shaped*, where the saturation front increased radially outward from the closed side boundary towards the center of the core. *Limited area initialization* was also observed; spontaneous imbibition started in one or a few distinct and limited area of the wetted surface, and advanced as a hemisphere outward from this area. The advancing hemispherical front was unaffected by the closed side boundary until it was reached, after which a segment shaped front formed, and advanced through the rest of the core plug. This thesis also presents an analysis of spontaneous imbibition experiments performed using in-situ imaging by PET-CT, not previously published, but exhibiting similar behavior.

The derivations of piston-like flow presented in **Chapter 4.2** to determine the production versus time during spontaneous imbibition use the rate of the advancing saturation front and a predetermined surface area of the saturation front. The derivations assume a uniform shape of the saturation front strictly dependent on the boundary condition of the sample. The interfacial area of the saturation front will be constant during a one-dimensional displacement and a function of the front position R_f during a spherical or radial displacements. If the initialization of imbibition into a one-dimensional sample occurs with a segmented or limited area shape, the saturation front surface area will not be constant. Thus, the assumption of a predetermined area of the saturation front is not valid, and neither are the models derived on this basis in **Chapter 4.2** to be invalid during such a situation. These models are used to calculate the modified characteristic length for different shapes and boundary cases and is therefore relevant when scaling spontaneous imbibition data. How the onset period influences the scaling of spontaneous imbibition is unknown. Based on the observations of hemispherical and segment fronts, implementation of radial spontaneous imbibition models during the onset period, may

be necessary to accurately predicting the production versus time. Derivations of radial and spherical production versus time models are presented in **Chapter 4.4** and **4.5**, and an overview of different modified characteristic lengths can be found in **Table 1**.

Two different scenarios where spontaneous imbibition has been described as radial or spherical has been investigated, both resulting in a production rate linear with time. Spontaneous imbibition experiments through a limited small hemispherical depression were performed by Mason et al. (2012). The special boundary condition caused most of the resistance to the flow to be in the vicinity of the depression, causing the spontaneous imbibition rate to be proportional to time, **Figure 7**. This boundary condition forces the flow to be counter-current. The radial advance of the spherical front will be proportional to $t^{\frac{1}{3}}$ (Xiao et al., 2012). The experiments verified the analytical model for spherical outward spontaneous imbibition presented in **Chapter 4.5**. The model is used later in the thesis, to analysis deviating saturation fronts exhibiting a spherical outward behavior.

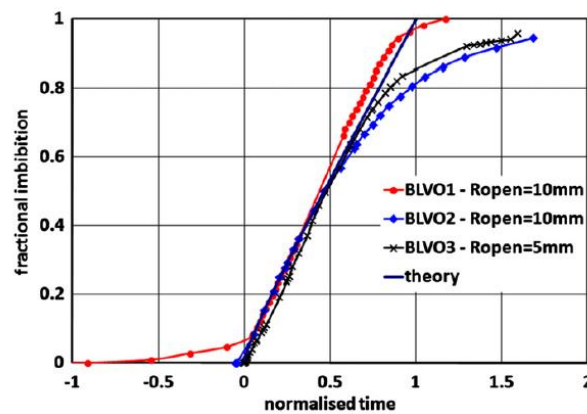


Figure 7: Hemispherical outward spontaneous imbibition, fractional imbibed volume versus normalized time. The results have been adjusted for induction time. The first half of the production curves have been fitted to a theoretic line, predicting an almost linear production curve. Form Mason et al. (2012).

Spontaneous imbibition from a slowly filled fracture was examined by Rangel-German and Kovscek (2002). The advance of the spontaneous imbibition saturation front during fracture filling occurred in two directions, both perpendicular outward from the fracture surface and parallel to the surface. *In-situ* (CT) images of the development of the saturation front is shown in **Figure 8**. The rate in both directions was proportional to the square root of time, resulting in a total imbibition rate proportional to time.

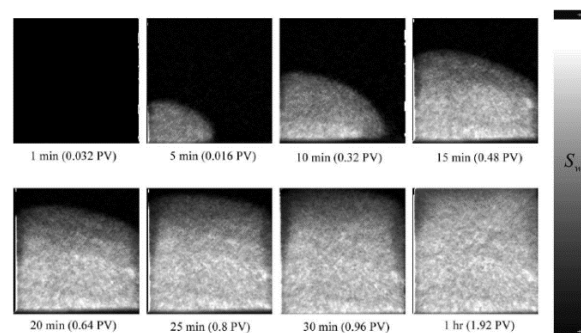


Figure 8: CT images for “filling fracture” at different times. Injection is from the lower left corner where the saturation front spreads radially. From Rangel-German and Kovscek (2002).

8 UNCONSOLIDATED SAND

Recent research presented spontaneous imbibition experiments as a quick and affordable method to estimate relative permeability and capillary pressure Fernø et al. (2015a) and Fernø et al. (2015b). The method is based on equations presented in **Chapter 4.6**. The calculation relies on the rate of the advancing saturation front and assumes a piston-like displacement. The front position can be determined by volumetric production data, visually, or with *in-situ* imaging. Through visualization of the saturation, piston-like displacement can be verified. Methods that includes a possible to inspect the spontaneous imbibition process visually is therefore preferred.

The method, developed for TEO free spontaneous boundary conditions was recently tested on imbibition tubes of glass, packed with unconsolidated material Vabø (2016) and Haugland (2016). The experimental method has several advantages compared with established laboratory procedures.

1. Direct visual inspection of flow in a uniform porous medium: verify piston-like displacement and determine the position of the saturation front.
2. Sand is an excellent unconsolidated material to use; it is cheap and available, the surface properties are known (i.e., quartz). And the porosity and the permeability of the pack can be designed by selecting mean grain size and the grain size distribution (Krumbein and Monk, 1942; Masch and Denny, 1966).
3. Imbibition tubes represent a quick and affordable method to investigate wettability, and the effect of wettability altering chemicals effect on capillary pressure, relative permeability and spontaneous imbibition (Haugland, 2016).
4. Capillary pressure estimates using centrifuges is challenging on unconsolidated material (Anderson, 1986b). Imbibition tubes represent an alternative and simple method to use on materials where the common centrifuge method is not feasible.

Meng et al. (2015) used similar glass tubes to study entrapment mechanisms of the non-wetting phase during spontaneous imbibition. They compared how the non-wetting viscosity influenced the entrapment in non-uniform and uniformly packed sand columns. In the uniform columns, the non-wetting viscosity did not influence the final saturation. However, in the non-uniform columns, the entrapment increased with the increase in non-wetting phase viscosity. Final saturation was measured and Meng et al. (2015) used the described method to estimate relative permeability of brine behind the front and capillary pressure at the front. Capillary filters were used at the imbibing surface to increase the capillary back pressure and promote co-current imbibition.

The Experiments performed by Vabø (2016), investigated imbibition rate and saturation front behavior in transparent sand packs. Unsymmetrical and non-uniform saturation front were observed during the displacements in several experiments and resulted in regions of trapped and bypassed oil behind the front. Most of the bypassed oil was located close to the inlet side of the tube, reducing the area available for water. The trapped oil had a significant effect on spontaneous imbibition development, and a close-to-constant imbibition rate was observed. This indicates the established water pathway at

the inlet side, sometimes narrow due to oil entrapment, dictated the resistance to flow during spontaneous imbibition. The mechanism for oil entrapment is counter-currently produced oil adhering to the surface of the capillary filter, reducing the area available for water imbibition, resulting in production of the non-wetting phase linear with time, shown in **Figure 9**.

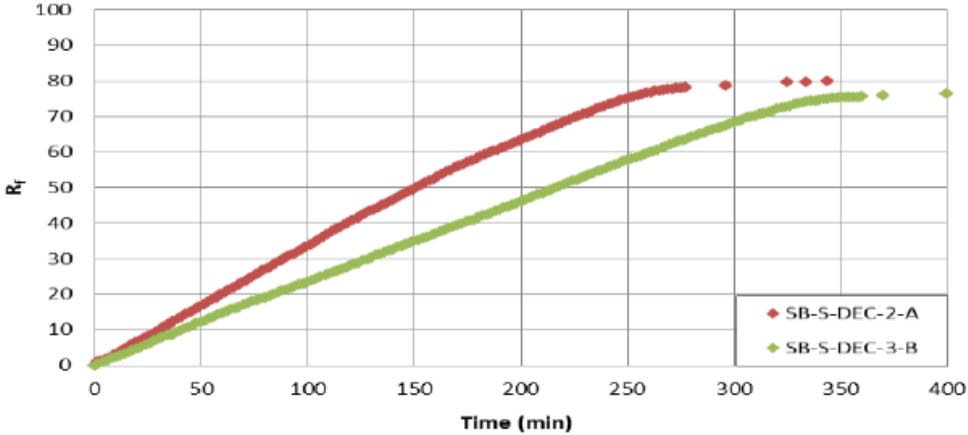


Figure 9: Show a linear relationship between the recovery factor of oil versus time during co-current spontaneous imbibition in sand packs using different capillary filters. From Vabø (2016).

The imbibition tub setup used by Vabø (2016) was modified developed and tested by Haugland (2016). The modifications reduced the entrapped regions and resulted in a stable piston-like displacement, which was reproducible and comparable to idealized production curves. Experiments were performed over a wide range of viscosity ratios, varying both the non-wetting and wetting phase viscosity. The wetting phase viscosity was altered using glycerol or polymers. The impact of Polymers on the wettability of the sand pack was investigated by comparing the front capillary pressure with capillary pressure measurements obtained using a glycerol-solution as the wetting phase. The front capillary pressure was estimated using the method and equations described in **Chapter 4.6**. Unfortunately, retention of the polymer molecule occurred on the inlet filter and reduced the rate of imbibition after some time.

9 CAPILLARY FLOW IN PAPER

Two-dimensional porous models with several different special boundary cases were created by covering paperboard with a clear two-component epoxy glue, giving access and the possibility to investigate the local flow patterns during the onset period of spontaneous imbibition. Paperboard is a porous material where the uptake of fluids is dominated by capillary forces (Salminen, 1988), and should, therefore, be considered to be a suitable analogue to a sedimentary material when investigating spontaneous imbibition. This was validated in this theses, by comparing experimental results to mathematical models based on capillary flow for an open end open and radial outward boundary case presented in **Table 1**.

9.1 CAPILLARY FLOW IN PAPER

Liquid flow and penetration into paper is a topic of great interest for the paper industry and is, therefore, a well-researched topic. There is a great variation for the motivations behind the research. Includes topics as how tissues absorb liquids (Beuther et al., 2010), defects in paperboard used to pack liquid when the edges of the paperboard are unsealed (Mark et al., 2012), and infiltration of inkjet droplets (Aslannejad et al., 2017; Oko, 2014).

Four mechanisms of water transport into paper has been proposed: Diffusion transport of vapor in the pores, capillary transport of liquids in the pores, surface diffusion in the pores and water transport through the fibers. A comprehensive research project investigating water transport in paper during short contact times was conducted by (Salminen, 1988). He concluded that capillary flow is the main mechanism for water transport in a hydrophilic unsized paper. Sizing of paper is the use of coating or additives in the paper to reduce the paper ability to absorb water (Gess, 1996). The capillary transport in paper is affected by several interactions between the water and the fiber matrix. This includes vapour adsorption ahead of the saturation front and swelling of the fiber matrix. Swelling of the matrix will influence the mean radius of the pores, and, consequently, the capillary pressure, affecting the validity of the Washburn equation. The swelling of the fiber matrix will also influence the pore volume, possibly making the imbibed volume disproportionate with the advance of the front.

PART II. METHODS AND EXPERIMENTAL SETUPS

This thesis built on work by Vabø (2016) and Haugland (2016) and used imbibition tubes and two-dimensional porous models to investigate the onset of spontaneous imbibition.

10 PREPARATION OF SAND AND FLUIDS

10.1 SAND PREPARATION AND PROPERTIES

Two different types of sand were used in the imbibition tube experiments. The types of sand had different mean grain size and grain size distribution. Type A sand consisted of grains with a very narrow distribution in grain size, from $212\ \mu\text{m}$ to $250\ \mu\text{m}$. Type B had a wider sand grain size distribution, ranging from $63\ \mu\text{m}$ to $500\ \mu\text{m}$. Details on the sand types are given in **Table 2**. Type A sand was extracted from a large batch of heterogeneous sand using geological sieves. The extraction was done in a sequential procedure. During each sieving step the sieve was placed on top of a bucket and approximately 100 grams of sand was sprinkle on to the sieve. Water was flushed over the sand bed, and the grains smaller than the mesh size was collected in the bucket beneath the sieve, the grains left on the sieve was collected in a separate container. All grains larger than 1000, 500 and $250\ \mu\text{m}$ were first separated out in three single steps, until the batch consisted of grains smaller than $250\ \mu\text{m}$. The smaller than $250\ \mu\text{m}$ batch of sand was sieved on a geological sieve with a mesh size of $212\ \mu\text{m}$, resulting in a batch of sand atop of the sieve with a grain size from $212\ \mu\text{m}$ to $250\ \mu\text{m}$.

Type B sand was delivered coarsely sieved. A set of small geological sieves was used to evaluate the grain size distribution in the Sand type B. The dry weight of each sieve was measured before they were stacked chronologically with the sieve with the coarsest mesh at the top. Approximately 30 grams of sand was sprinkled over the top sieve, and the sand bed was flushed with water. The grains collected on each sieve would be larger than the mesh size of the sieve itself and smaller than the mesh size of the sieve above in the stack. The stack of sieves was placed in a heating cabinet to dry, and the amount of sand on each sieve was calculated gravimetrically.

Both batches of sand contained some non-sand material, visible when the sand was stirred with water. The sand was cleaned by filling it into a large container and constantly flushing it with tap water for 48 hours. The clean sand was dried in a heating cabinet. Finally, the sand was heated to $500\ \text{C}^\circ$ for 8 hours in a furnace to oxidize and remove any remaining organic materials (Anderson, 1986b).

The wettability of the sand grains was tested qualitatively to be very strongly water wet using the flotation test method proposed by Nutting (1925). Sand grains were gently sprinkled over beaker filled with water and oil, forming two immiscible layers. The strongly water-wet grains settled at the bottom of the beaker. Any oil-wet grains would be suspended at the oil-water interface. The test is useable to determine a strong wetting condition.

Table 2: Grain size distribution as weight percent for the two types of sand used in the imbibition tube experiments.

Sand Type	Grain size distribution
Type A	100 wt.% 212 μm -250 μm
Type B	<1 wt.% 250 μm -500 μm
	84 wt.% 125 μm -250 μm
	15 wt.% 63 μm -125 μm
	<1 wt.% 212 μm -250 μm

10.2 FLUIDS PREPARATIONS AND PROPERTIES

10.2.1 Wetting fluids

The Sodium Chloride Brine was prepared by mixing distilled water with five wt% Sodium chloride (equivalent to 0.856M). 0.5ml of NaN₃ was added to every 10 liters of brine to inhibit bacterial growth. Dyed brine was prepared by mixing one weight percent of food coloring to the brine. The Sodium Chloride Brine was used in most imbibition tube experiments, except in experiment SP5, SP6 and SP7, where viscosified aqueous phases with matching viscosities were used. A brine-glycerol solution was used to increase the viscosity of the aqueous phase in experiment SP7, and a viscous, water-based polymer solution was used as the aqueous phase in experiment SP5 and SP6. Glycerol is well suited to examine the effect of a high wetting viscosity without affecting the chemical properties of the aqueous phase. Glycerol is soluble in water at all concentrations and insoluble in hydrocarbons, the viscosity of a water-glycerol solution varies non-linearly, from 1cP for pure water to 1650 cP for pure glycerol at 20 C° (Fischer and Morrow, 2006). The polymer solution was prepared by mixing Sodium Chloride Brine with Alcoflood 935 to a 5000ppm solution (0.5wt%). Alcoflood 935 is a hydrolysed polyacrylamide (HPAM). Polymers are shear-thinning, meaning that the viscosity decreases as the shear rate increases (Donaldson et al., 1989). All viscosities were measured with a rotational viscometer (Brookfield DV-II+ Pro). The shear-thinning nature of the polymer solution is recognizable in **Figure 10**, where the viscosity of the polymer solution are plotted versus the rotation speed of the spindle inside the viscometer, the rotation speed is proportional to the shear speed. Glycerol behaved as newtonian fluid, i.e. the measured viscosity was independent from the rotation speed. The density of the fluids was measured by filling a 500ml graded cylinder and recording the weight. The dye used in the wetting phase was a gel based food coloring containing glycerol and the dye E124.

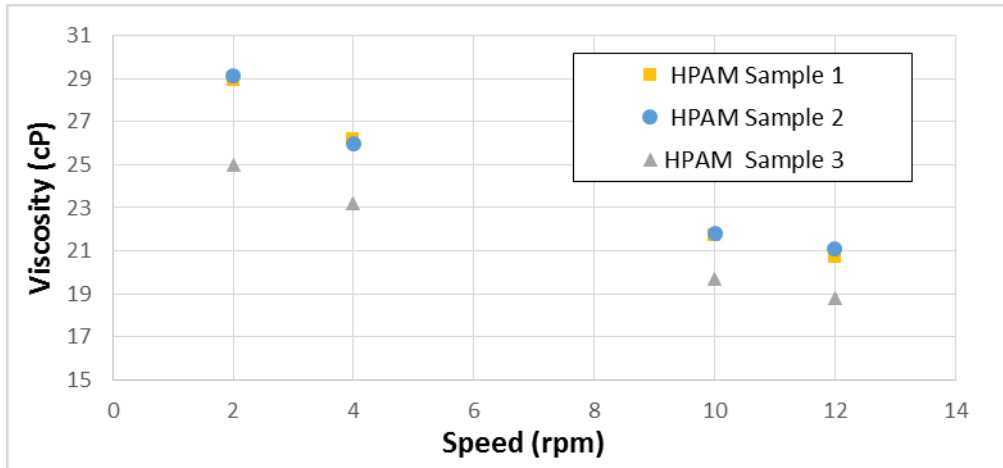


Figure 10: Measured viscosity of the polymer solution at different rotation speeds. HPAM Sample 1 was collected before experiment SP5, HPAM Sample 2 was collected before experiment SP6, and HPAM Sample 3 was collected after experiment SP6. Measurements performed in cooperation with Haugland (2016).

10.2.2 Non-wetting fluids

Three different mineral oils with varying viscosity were used in the imbibition tube experiments, Decane 95%, DTE FM 32 and Marcol 82, properties are given in **Table 3**. Surface active components were removed from the mineral oils by filtration through a column consisting of aluminum oxide and silica gel, using the technique described in Fernø et al. (2013). The aluminum oxide and silica gel were filled into a separatory funnel as two distinct beds, with glass wool at the bottom. The mineral oil was gently poured over the filtration bed, and the filtrated oil was collected from the outlet valve on the separatory funnel. The dye used in the non-wetting phase was Sundan blue.

Table 3: Properties of the fluids used in the imbibition tube experiments.

Fluid	Density, ρ ($\frac{g}{cm^3}$)	Viscosity, μ (cP)
Oleic Phase		
Decane 95 %	0.73 ± 0.01	0.96 ± 0.01
Marcol 82	0.84 ± 0.01	32.6 ± 0.2
DTE FM 32	0.85 ± 0.01	73.2 ± 0.7
Aqueous Phase		
5 wt% NaCl Brine	1.03 ± 0.01	1.15 ± 0.02
70 wt% glycerol	1.20 ± 0.01	28.3 ± 0.70
5000 ppm HPAM	NM	29.0 ± 1.00^s

^{NM} Not measured. ^s The fluid is shear-thinning

11 THE IMBIBITION TUBE SETUP

The experimental setup used for the imbibition tubes was modified based on experiences from previous experiments. Two different types of setups were used; the submerged imbibition tube setup and the continuously flushing inlet setup. The submerged imbibition tube setup consisted of a bath filled with the wetting fluid where the imbibition tube was submerged. The non-wetting fluid was produced through a fitting going through a hole in the side of the water bath. The two setups consisted of similar types of inlet- and outlet-parts, however, the design of the parts varied. The modifications in design for the continuously flushing inlet made it possible to inject fluids through the sand pack after spontaneous imbibition; measure the counter currently produced non-wetting phase, and adjust the head pressure at the inlet. The hydro static pressure in the submerged imbibition tube was dependent. For the continuously flushing inlet, the complete sand pack was visible through the glass tube, making it possible to observe the saturation front directly after spontaneous imbibition had started. The mounting, sand filling and saturation procedure for the two imbibition tube setups were similar. Therefore, only the experimental procedure for the continuously flushing inlet is presented stepwise. The initialization of the spontaneous imbibition experiment differs between the two setups. The submerged imbibition tube was simply connected to the outlet fitting and then submerge into the water bath. Drainage and permeability measurements were not possible with the water bath setup. The separate parts used in the continuously flushing inlet setup is illustrated in **Figure 11**.

11.1 PREPARATIONS OF SAND PACK SPONTANEOUS IMBIBITION EXPERIMENTS

1. Counter-current production collector with $\frac{1}{4}$ " venting tubes
2. $\frac{1}{4}$ " Male-male Swagelok tube fitting and $\frac{1}{4}$ " cap
3. Graded Imbibition tube
4. Continuously flushing inlet
5. Coarse metal mesh
6. Paper filter
7. Threaded inlet end piece
8. Screws
9. Glass imbibition tube
10. Fine metal mesh
11. Threaded outlet end piece and rubber plug with tubing
12. $\frac{1}{8}$ " Swagelok quarter turn valve
13. $\frac{1}{4}$ - $\frac{1}{8}$ " Reducing Swagelok fitting

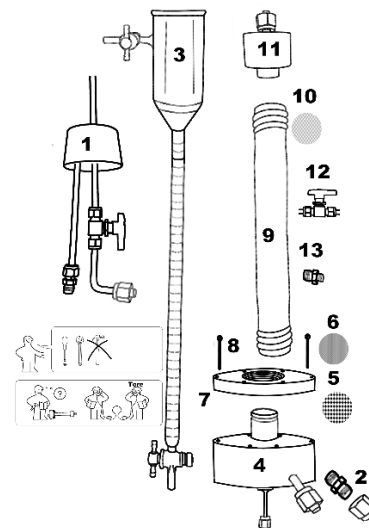


Figure 11: Illustrates all the separate parts used to build the continuously flushing inlet. The figures on the lower left side should be credited IKEA.

Mounting the continuously flushing inlet to the imbibition tube:

The threaded inlet end piece (7) was screwed onto one end of the imbibition tube (9). The coarse metal mesh (5) and the paper filter (6) was attached to the continuously flushing inlet (4), before it was pushed into the imbibition tube and secured to the threaded end piece

Filling the imbibition tube with sand:

To assure a uniform sand pack the imbibition tube was held vertically, filled sequentially with sand, and shaken for 30 seconds between every sequence. Each sequence of sand was approximately two centimeters long. The imbibition tube was filled until the level of the sand was 3 centimeters from the end of the tube. The weight of the imbibition tube was measured before and after filling.

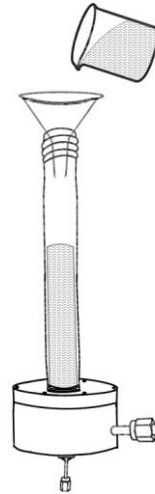


Figure 12: Illustrates the sand filling process.

Mounting the outlet on the imbibition tube:

The fine metal mesh (10) was put on the top of the sand pack before the outlet rubber plug with tubing (11) was pushed down into the imbibition tube (9) and secured with the threaded outlet end piece (11).

Saturating the imbibition tube:

Air was evacuated out of the imbibition tube using a vacuum pump connected to the inlet side of the imbibition tube. The saturation fluid was degassed in a container connected to the vacuum pump. The degassed fluid was poured into a funnel connected to the top of the imbibition tube

The valve between the funnel and imbibition tube was opened when a sufficiently low pressure in the imbibition tube was reached. The degassed fluid quickly flowed into the sand pack and completely saturated it. Finally, both valves were closed and the tubes disconnected. The weight of the imbibition tube was measured before and after it was saturated, and the weight difference was used to calculate the porosity and pore volume.

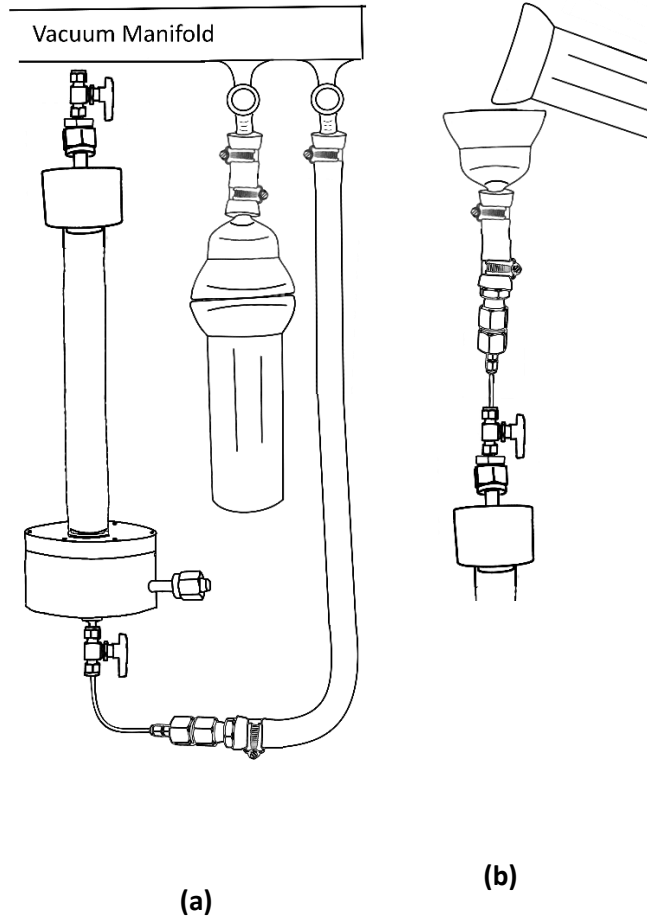


Figure 13: Left: The imbibition tube and the container used to degas the fluids connected to the vacuum pump. Right: The degassed fluid is saturating the imbibition tube .

The dead volume of the continuously flushing inlet was estimated by filling it up with water and measuring the increase in mass. The dead volume of the continuously flushing inlet with $\frac{1}{4}$ inch tubing was 3.7 ml, and 3.5 ml for the continuously flushing inlet with $\frac{1}{8}$ inch tubing.

Connecting the imbibition tube to the flushing equipment:

To enable circulation of fluids in the endpiece the inlet tube on the continuously flushing inlet was connected a Pharmacia pump. The venting tube on the continuously flushing inlet was connected to the vertically held counter-current production collector. A graduated Imbibition tube was placed under the outlet tubing to collect the co-current production.

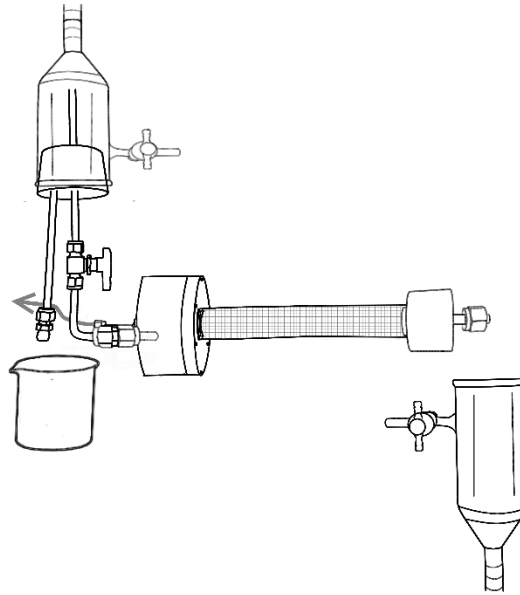


Figure 14: Illustrates the complete imbibition tube for the continuously flushing inlet setup.

11.2 PERMEABILITY MEASUREMENTS AND DRAINAGE

The setup was equipped with a high precision pump capable of delivering a constant flow rate in the range from 1 to 499 ml/h . A pressure transducer manufactured was connected to the inlet side of the imbibition tube, used to measuring the differential pressure from the inlet to the atmospheric pressure at the outlet of the imbibition tube. Minor oscillations in the pressure due to the step volume in the pump was observe in the pressure measurements. The standard derivation of the oscillating pressure was used as the uncertainty in permeability calculations, as this contribution was significantly larger than any other contribution to the uncertainty.

Absolute permeability was measured by injecting the same fluid as the imbibition tube was initially saturated with, i.e. before drainage. The fluid was injected with several constant injection rates. The differential pressure over the imbibition tube was measured with the ESI pressure transducer. Drainage is the process where the non-wetting fluid is forcibly displacing the wetting fluid out of the porous medium. The imbibition tube initially saturated with the wetting fluid was drained to a low water saturation $S_{w,f}$, by injecting mineral oil. High viscous oil, Marcol or DTM FM 68, were used to increase the volume of brine produced during the drainage process. The high viscous oil was injected from an accumulator connected to the pump by bypass tubing. After reaching a low water saturation, the high viscous oil was miscible displaced by injecting the mineral oil intended for the experiment. The injection was stopped when the pressure measurements flattened out, indicating an insignificant amount of high viscous oil left in the sand pack. Some of the imbibition tubes were used in several spontaneous imbibition experiments and was therefore re-drained to a new initial saturation between the spontaneous imbibition experiments. The low water saturation after drainage is hereby denoted as the initial water saturation $S_{w,i}$.

The effective permeability for the non-wetting phase at the initial water saturation was measured at the end of the drainage process. The effective permeability for the wetting phase at the residual oil saturation was measured after the end of spontaneous imbibition. Measuring the wetting phase effective permeability by injecting the wetting fluid was a forced imbibition process, resulting in a further production of the non-wetting phase and increased water saturation. The effective permeability is dependent on the saturation (Anderson, 1987), and the measured effective permeability of the wetting phase is therefore not necessarily the same as the effective permeability of the wetting phase behind the saturation front during spontaneous imbibition.

11.3 PRESSURE IN THE CONTINUOUSLY FLUSHING INLET.

The pressure in the wetting phase at the inlet side of the imbibition tube, designated P_{Inlet} , is of great concern when performing spontaneous imbibition experiments. It is ambitious and problematic to completely eliminate the presence of any inlet pressure in any type of spontaneous imbibition experimental setup. However, in a well-designed setup the inlet pressure should be considered insignificant. Ignoring the capillary back pressure, the differential pressure from the inlet surface to the saturation front will be the sum of the inlet pressure P_{Inlet} and the front capillary pressure $P_{c,f}$. A imbibition process should not be described as a spontaneous if P_{Inlet} is of a significant magnitude compared with $P_{c,f}$, otherwise it will be a forced imbibition process (Morrow and Mason, 2001). It is not straightforward to determine when the inlet pressure is of significance, but it should be compared with the measured capillary front pressure.

There are two contributions to the inlet pressure P_{Inlet} in the continuously flushing inlet: The height difference ΔH between the continuously flushing inlet and the outlet tube on the counter-current production collector, denoted ΔP_H . The second pressure contribution is a result of the viscous resistance associated with the flow through the complete continuously flushing inlet setup, denoted ΔP_R . An approximate estimate of the pressure ΔP_{Inlet} in the continuously flushing inlet can be calculated using the Darcy-Weisback equation (57) for the pressure drop in a pipe during laminar flow (McCabe et al., 2005). Which incorporates the flow rate q (m^3/s), the dynamic viscosity of the fluid μ ($Pa \cdot s$) and the shape and size properties of the pipe. The shape and size properties for the continuously flushing inlet was simplified to a pipe length L (m) and pipe diameter D (m).

$$\Delta P = L * \frac{128}{\pi} * \mu * \frac{q}{D^4} \quad (57)$$

The pressure contribution due to the viscous resistance in the continuously flushing inlet setup should be considered to be insignificant for flushing at low rates ($20 \frac{ml}{h}$). The estimated pressure ΔP_R , associated with the viscous resistance for two different pipe diameters D , is shown in **Table 4**.

Table 4: Calculated pressure contribution due to viscous resistance through the complete continuously flushing inlet setup with varying pipe diameter. The pressure is calculated by equation (57).

D (Inch)	q [$\frac{ml}{H}$]	L [m]	μ [cP]	ΔP [Pa]	ΔP [mmH ² O]
$\frac{1}{8}$	20	1	1	2.36	0.24
$\frac{1}{4}$	20	1	1	0.14	0.01

Presenting the pressure in the unit mmH^2O is convenient when comparing the two pressure contributions resulting in the total inlet pressure ΔP_{Inlet} . Both pipe diameters results in a pressure ΔP_R lower than the pressure contribution from a height difference $\Delta H = 1mm$ giving a $\Delta P_H = 1 mmH^2O = 9.81 Pa$. The limiting factor for the inlet pressure is the ability to set and control the height difference ΔH , having an uncertainty of $1 mm$. Both $\frac{1}{8}$ Inch and $\frac{1}{4}$ Inch tubing was used as the outlet tubing from the continuously flushing inlet and the Counter-current production collector. The size of the tubing had no observable effect on the spontaneous imbibition experiments. However, the physical strength of the $\frac{1}{4}$ Inch tubing made it easier to control the height difference ΔH . The pressure estimates in **Table 4**, does not include effects from bends in the pipe, valves and outlet and inlet effects.

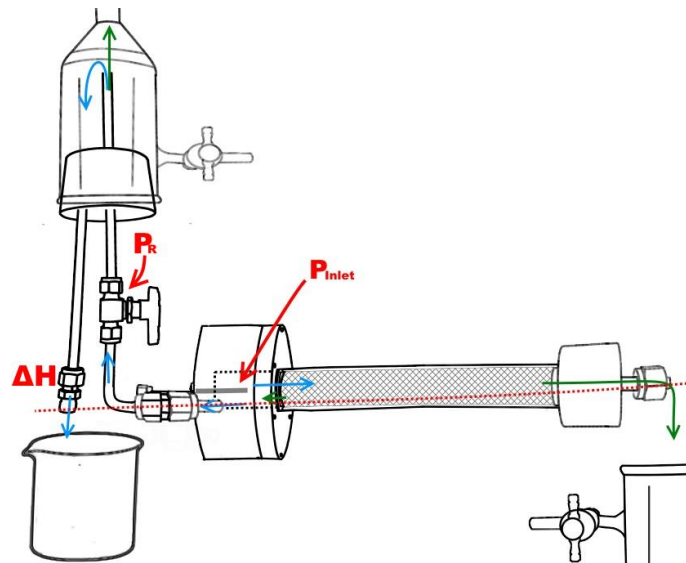


Figure 15: Illustrates the flow direction of the wetting fluid through the continuously flushing inlet and the counter current production collector (blue arrows), where some of the wetting fluid spontaneously imbibes into the imbibition tube resulting in co- and counter currently produced non-wetting phase (green arrows). The height difference ΔH between the inlet and the outlet tube is marked as a red dotted line, the uncertainty in ΔH is $1 mm$.

11.4 INITIATING AND MEASURING THE SPONTANEOUS IMBIBITION EXPERIMENTS.

The spontaneous imbibition experiments were initiated by pumping wetting fluid through the continuously flushing inlet, venting it through the counter-current production collector and exposing the sand pack to brine. The counter-currently produced oil flowed into the counter-current production collector and was trapped in the graduated measuring tube due to the density difference between the two phases. The co-current produced oil was collected in the co-current production collector. The production into both production collectors and the advancing front were monitored using three separate cameras. The saturation after, and the recovery factor from, spontaneous imbibition was calculated based on the measured produced volumes.

Dye was added to the wetting or non-wetting fluids in some of the experiments, to increase the visible intensity of the saturation front. The dye in the wetting phase was added directly to the brine flowing through the continuously flushing inlet. The dyed non-wetting mineral oil was injected it through the imbibition tube before the spontaneous imbibition experiment was initiated.

12 TRANSPARENT TWO-DIMENSIONAL POROUS MODELS.

Two-dimensional porous models with several different special boundary cases were created by covering paperboard with a clear two-component epoxy glue to investigate the onset of spontaneous imbibition. Four different boundary cases were tested: two special boundary cases with one or multiple limited open areas, the open areas were 5mm wide, and two boundary cases conventional, One End Open and Radial Outward boundary cases.

12.1 PREPARATION OF THE TWO-DIMENSIONAL PAPER MODELS.

The two-dimensional models were prepared by sketching the desired shape of the sample directly onto a paperboard. The upper and lower surface of the paperboard were sequentially covered with epoxy glue. Then, each single sample was cut out of the paperboard following the previously drawn sketches. The samples were glued onto a metal plate with glue also covering the open cut-surfaces. The open end surfaces on the radial and one end open samples was preserved unexposed to the glue. The smaller limited open surfaces on the Onset samples were made by slicing of small extended pieces of paperboard. The extended pieces had a width equal to the desired limited open areas and were located at the planned location of the limited open areas.

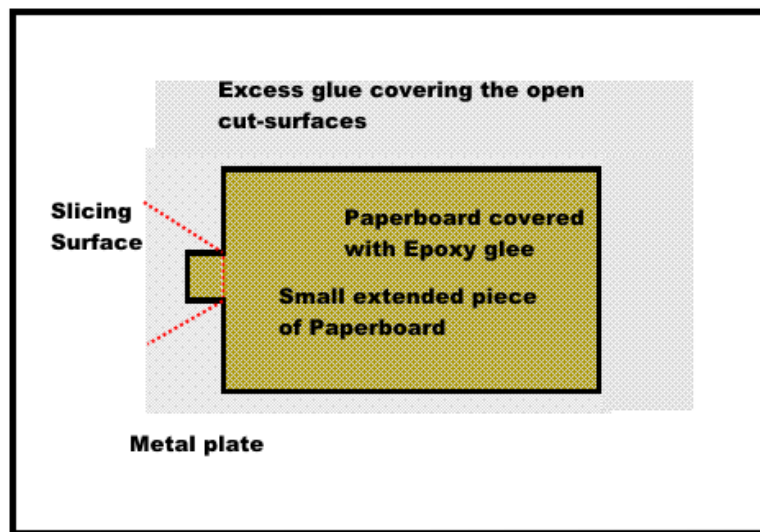


Figure 16: Illustrates a paperboard sample glued to a metal surface, with all surfaces, including the cut-surfaces covered with epoxy glue. The red-dotted line illustrates where the extended pieces will be removed, opening up the limited open area.

All closed surfaces of the samples were coated with a two-component transparent epoxy glue named Strong Epoxy Rapid, produced by Casco. The epoxy glue was prepared by mixing equal amounts of hardener and resin to a total desired amount of epoxy glue. The cure time was approximately 40 minutes at ambient temperature to reach a durable strength and reaching full strength after 4 hours. The cut-surface is the cross section of the paperboard. The paperboard was 1.5mm thick.

12.2 INITIATING AND MEASURING SPONTANEOUS IMBIBITION INTO TWO-DIMENSIONAL PAPER MODELS

The spontaneous imbibition into the two-dimensional models was visually measured by monitoring the advancing saturation front with a camera, taking pictures at fixed intervals and simultaneously using a weight to measure the mass of the sample continuously. Measuring the mass and taking pictures simultaneously was doable by using a below balance weight placed above a transparent water bath, and placing the camera underneath the water bath, illustrated in **Figure 17**.

The paperboard samples glued to the metal plate was hanged under the below balance weight and submerge into the water bath. The hanging equipment consisted of five magnets and nylon cords, four of the magnets were used to attach the metal plate, the last magnet was used to separate the nylon cord into a lower and upper part. The knots used to tie the hanging equipment made it possible to adjust the height and levelling of the metal plate.

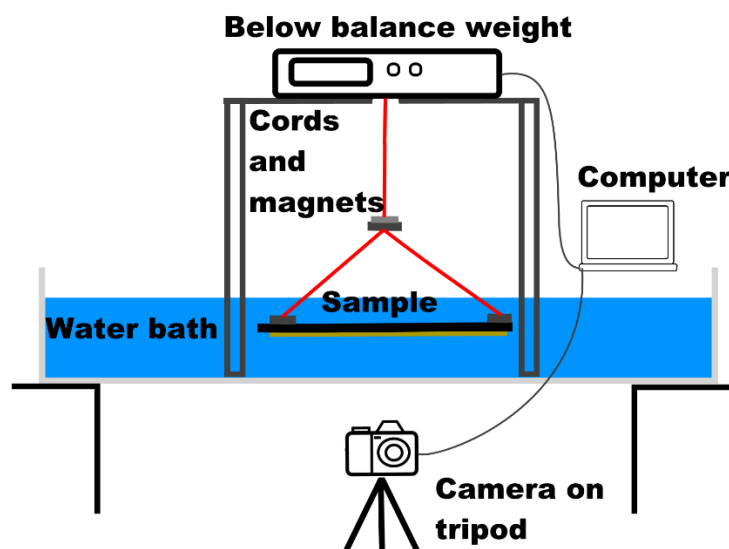


Figure 17: Illustrating the complete setup used for the two dimensional paper models.

The spontaneous imbibition rate into the two dimensional models was estimated from pictures taken by the camera at fixed time steps. The area of imbibition was estimated for each time step by counting the number of square pixels in the imbibed and air saturated area. A distinct saturation front separated the imbibed and non-imbibed area of the paperboard samples. Several tools in the communally available graphic editor paint.net were used to discriminate the area behind and ahead of the saturation front, and to count the number of square pixels. First, the non-paperboard part of the picture was outlined and painted red. Secondly, the saturation front was outlined using the pencil tool, drawing a one square pixel wide line. The Fill tool was used to paint the outlined and enclosed imbibed area black, and the non-imbibed area white. Finally, the size of each area was estimated by counting the number of pixels square having the distinct colors. When selecting an area in paint.net, the number of pixels square inside the selected area will be shown in the lower left corner. The Magic Wand tool was used to select an area with one distinct color.

The uncertainty of the position of the saturation front and the effect on the uncertainty of the imbibed area was estimated by drawing a yellow line over the saturation front. The thickness of the line was adjusted so that it cover both sides of the saturation front with a solid margin. The number of square pixels of the yellow line was used to calculate the uncertainty of the increasing imbibed area, as illustrated in **Figure 18**.

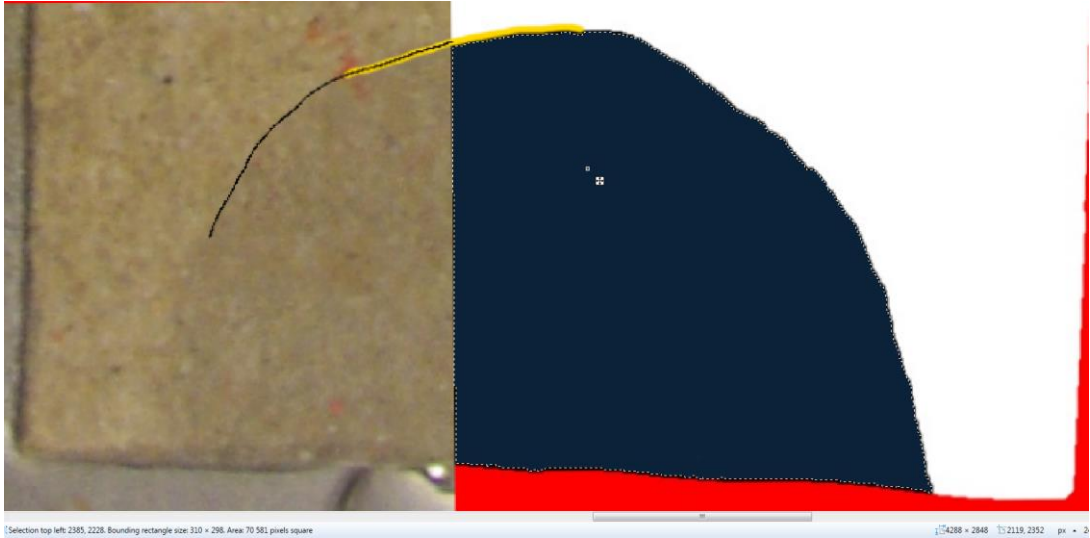


Figure 18: Illustrating the procedure to estimate the area behind the imbibition front. The area behind and ahead of the front was estimated by discriminating the different area with distinct colors. The area around the paperboard was painted red, the non-imbibed area of the paperboard was painted white, and the imbibed area was painted black. The yellow brush line represents the uncertainty in the location of the saturation front.

PART III. RESULTS AND DISCUSSION

13 OVERVIEW OF THE EXPERIMENTS

The overview is separated into two parts, a **Table 5** containing the imbibition tube experiments and a **Table 6** containing the two-dimensional model experiments. The overview contains only key properties; details are included in **Appendix III**.

Table 5: An overview of the imbibition tube experiments with key properties and results. The Group A experiments were performed in cooperation with (Haugland, 2016).

Experiment	Sand pack properties L [cm] PV [ml] ϕ [frac.PV]	Sand pack Permeability's [Darcy]	Fluids and viscosity ratio	Saturations and recovery [frac.PV]	Recovery [frac.OOIP] and ratio produced counter- currently
Group A	Setup: Submerged imbibition tube. Porous Material: Sand 212-250 μm				
SP2	$L = 48.4 \pm 0.1$ $PV = 62.3 \pm 0.6$ $\phi = 0.39 \pm 0.01$	K^B $k_{f,w}^B$ $k_{f,nw}^B$	WP: Brine NWP: Decane $\mu_{nw} / \mu_w = 0.8$	$S_{w,l} = 0$ $S_{w,sp} = 0.88 \pm 0.01$	$R_f = 0.88 \pm 0.01$ $\frac{Q_{cc}}{Q} = 0.12$
SP3	$L = 48.3 \pm 0.1$ $PV = 59.5 \pm 0.6$ $\phi = 0.377$	K^B $k_{f,w}^B$ $k_{f,nw}^B$	WP: Brine NWP: Marcol 82 $\mu_{nw} / \mu_w = 28.3$	$S_{w,l} = 0$ $S_{w,sp} = 0.84 \pm 0.01$	$R_f = 0.84 \pm 0.01$ $\frac{Q_{cc}}{Q} = 0$
SP4	$L = 48.3 \pm 0.1$ $PV = 62.9$ $\phi = 0.399$	K^B $k_{f,w}^B$ $k_{f,nw}^B$	WP: Brine NWP: DTE FM 32 $\mu_{nw} / \mu_w = 63.7$	$S_{w,l} = 0$ $S_{w,sp} = 0.77 \pm 0.01$	$R_f = 0.77 \pm 0.01$ $\frac{Q_{cc}}{Q} = 0.4$
SP5	$L = 48.2 \pm 0.1$ $PV = 63.9 \pm 0.6$ $\phi = 0.406$	K^B $k_{f,w}^B$ $k_{f,nw}^B$	WP: HPAM NWP: Decane $\mu_{nw} / \mu_w = 0.033$	$S_{w,l} = 0$ $S_{w,sp} = 0.57 \pm 0.01$	$R_f = 0.57 \pm 0.01$ $\frac{Q_{cc}}{Q} = 0$
SP6	$L = 48.2 \pm 0.1$ $PV = 62.0 \pm 0.6$ $\phi = 0.393$	K^B $k_{f,w}^B$ $k_{f,nw}^B$	WP: HPAM NWP: Decane $\mu_{nw} / \mu_w = 0.033$	$S_{w,l} = 0$ $S_{w,sp} = 0.77 \pm 0.01$	$R_f = 0.77 \pm 0.01$ $\frac{Q_{cc}}{Q} = 0$
SP7	$L = 48.2 \pm 0.1$ $PV = 60.7 \pm 0.6$ $\phi = 0.385$	K^B $k_{f,w}^B$ $k_{f,nw}^B$	WP: Glycerol NWP: Decane $\mu_{nw} / \mu_w = 0.034$	$S_{w,l} = 0$ $S_{w,sp} = 0.82 \pm 0.01$	$R_f = 0.82 \pm 0.01$ $\frac{Q_{cc}}{Q} = 0$
SP8 ^F	$L = 48.45 \pm 0.1$ $PV = 59.7 \pm 0.6$ $\phi = 0.38$	$K = 15.7 \pm 0.2$ $k_{f,w} = 9.2 \pm 0.8$ $k_{f,nw} = 12.4 \pm 0.2$	WP: Brine NWP: Decane $\mu_{nw} / \mu_w = 0.8$	$S_{w,l}$ $S_{w,sp}$	R_f $\frac{Q_{cc}}{Q}$
Group B	Setup: Flushing inlet 1. Porous Material: Sand new μm				
SP9	$L = 45.5 \pm 0.1$ $PV = 65.2 \pm 0.7$ $\phi = 0.44 \pm 0.1$	$K = \text{NM}$ $k_{f,w} = \text{NM}$ $k_{f,nw} = \text{NM}$	WP: Brine NWP: Decane $\mu_{nw} / \mu_w = 0.8$	$S_{w,l} = 0$ $S_{w,sp} = 0.84 \pm 0.01$	$R_f = 0.84 \pm 0.01$ $\frac{Q_{cc}}{Q} = 0.06^E$
SP10_E1	$L = 45.7 \pm 0.1$ $PV = 64.6 \pm 0.7$ $\phi = 0.43 \pm 0.1$	$K = 13.8 \pm 0.2$ $k_{f,w} = 7.0 \pm 0.4$ $k_{f,nw} = 11.4 \pm 0.4$	WP: Brine ^D NWP: Decane $\mu_{nw} / \mu_w = 0.8$	$S_{w,l} = 0.30 \pm 0.01$ $S_{w,sp} = 0.97 \pm 0.01$	$R_f = 0.95 \pm 0.01$ $\frac{Q_{cc}}{Q} = 0.07^E$
SP10_E2	$L = 45.7 \pm 0.1$ $PV = 64.6 \pm 0.7$ $\phi = 0.43 \pm 0.1$	$K = 13.8 \pm 0.2$ $k_{f,w} = 7.0 \pm 0.4$ $k_{f,nw} = 11.4 \pm 0.4$	WP: Brine ^D NWP: Decane $\mu_{nw} / \mu_w = 0.8$	$S_{w,l} = 0.25 \pm 0.01$ $S_{w,sp} = 0.83 \pm 0.02$	$R_f = 0.78 \pm 0.02$ $\frac{Q_{cc}}{Q} = 0.09^E$
SP11	$L = 46.1 \pm 0.1$ $PV = 68.4 \pm 0.7$ $\phi = 0.47 \pm 0.1$	$K = 16.7 \pm 0.4$ $k_{f,w} = 6.5 \pm 0.2$ $k_{f,nw} = 9.7 \pm 0.3$	WP: Brine ^D NWP: Decane $\mu_{nw} / \mu_w = 0.8$	$S_{w,l} = 0.26 \pm 0.01$ $S_{w,sp} = 0.71 \pm 0.01$	$R_f = 0.60 \pm 0.01$ $\frac{Q_{cc}}{Q} = 0.10^E$
SP12 ^A					
SP13_E1 ^C	$L = 45.8 \pm 0.1$ $PV = 60.6 \pm 0.7$ $\phi = 0.42 \pm 0.1$	$K = 26.7 \pm 5.3$ $k_{f,w} = 18.0 \pm 4.0$ $k_{f,nw} = 18.8 \pm 4.8$	WP: Brine ^D NWP: Decane ^D $\mu_{nw} / \mu_w = 0.8$	$S_{w,l} = 0.13 \pm 0.01$ $S_{w,sp} = 0.86 \pm 0.01$	$R_f = 0.84 \pm 0.01$ $\frac{Q_{cc}}{Q} = 0.43$

SP13_E2 ^C	$L = 45.8 \pm 0.1$ $PV = 60.6 \pm 0.7$ $\phi = 0.42 \pm 0.1$	$K = 26.7 \pm 5.3$ $k_{f,w} = 18.0 \pm 4.0$ $k_{f,nw} = 18.8 \pm 4.8$	WP: Brine ^D NWP: Decane ^D $\mu_{nw} / \mu_w = 0.8$	$S_{w,l} = 0.12 \pm 0.01$ $S_{w,sp} = 0.87 \pm 0.02$	$R_f = 0.86 \pm 0.02$ $\frac{Q_{cc}}{Q} = 0.40$
SP14 ^C	$L = 45.5 \pm 0.1$ $PV = 62.5 \pm 0.7$ $\phi = 0.43 \pm 0.1$	$K = 16 \pm 0.1$ $k_{f,w} = \text{NM}$ $k_{f,nw} = 6.3 \pm 0.5$	WP: Brine ^D NWP: Decane $\mu_{nw} / \mu_w = 0.8$	$S_{w,l} = 0.16 \pm 0.01$ $S_{w,sp} = 0.58 \pm 0.01$	$R_f = 0.50 \pm 0.01$ $\frac{Q_{cc}}{Q} = 0.66$
SP15 ^A	$L = 45.5 \pm 0.1$ $PV = 62.6 \pm 0.7$ $\phi = 0.43 \pm 0.1$	$K = \text{NM}$ $k_{f,w} = \text{NM}$ $k_{f,nw} = \text{NM}$	WP: Brine ^D NWP: Decane ^D $\mu_{nw} / \mu_w = 0.8$	$S_{w,l} = 0$ $S_{w,sp} = 0$	$R_f = 0$ $\frac{Q_{cc}}{Q} = 0$
Group C	Setup: Flushing inlet 2. Porous Material: Sand new μm				
SP16_E1	$L = 15.7 \pm 0.1$ $PV = 23.8 \pm 0.3$ $\phi = 0.46 \pm 0.1$	$K = 14.5 \pm 0.5$ $k_{f,w} = 4.5 \pm 0.2$ $k_{f,nw} = \text{NM}$	WP: Brine [*] NWP: Decane $\mu_{nw} / \mu_w = 0.8$	$S_{w,l} = 0$ $S_{w,sp} = 0.92$	$R_f = 0.92 \pm 0.01$ $\frac{Q_{cc}}{Q} = 0.14$ ^E
SP16_E2	$L = 15.7 \pm 0.1$ $PV = 23.8 \pm 0.3$ $\phi = 0.46 \pm 0.1$	$K = 14.5 \pm 0.5$ $k_{f,w} = 4.5 \pm 0.2$ $k_{f,nw} = \text{NM}$	WP: Brine ^D NWP: Decane ^D $\mu_{nw} / \mu_w = 0.8$	$S_{w,l} = 0.22 \pm 0.01$ $S_{w,sp} = 0.81 \pm 0.02$	$R_f = 0.76 \pm 0.02$ $\frac{Q_{cc}}{Q} = 0.20$ ^E
SP17_E1	$L = 15.8 \pm 0.1$ $PV = 25.2 \pm 0.3$ $\phi = 0.45 \pm 0.1$	$K = 14.8 \pm 0.4$ $k_{f,w} = 4.3 \pm 0.4$ $k_{f,nw} = \text{NM}$	WP: Brine ^D NWP: Decane $\mu_{nw} / \mu_w = 0.8$	$S_{w,l} = 0$ $S_{w,sp} = 0.89$	$R_f = 0.89$ $\frac{Q_{cc}}{Q} = 0.12$ ^E
SP17_E2 ^A	$L = 15.8 \pm 0.1$ $PV = 25.2 \pm 0.3$ $\phi = 0.45 \pm 0.1$	$K = 14.8 \pm 0.4$ $k_{f,w} = 4.3 \pm 0.4$ $k_{f,nw} = \text{NM}$	WP: Brine NWP: Decane ^D $\mu_{nw} / \mu_w = 0.8$	$S_{w,l} = 0.14 \pm 0.01$ $S_{w,sp} = 0.28 \pm 0.02$	$R_f = 0.17 \pm 0.02$ $\frac{Q_{cc}}{Q} = 0.33$ ^E

^A Wettability alteration. ^B Assumed equal values as measured in SP8. ^C Collapsed sand pack. ^D Dyed fluid. ^E The Counter-currently produced volume is equal to the dead volume in the continuously flushing inlet (3.5ml), and the counter-current production is therefore zero. ^F Failed. ^L Leakage. ^{NM} Not measured. SPx_E1 the sand pack x has been redrained and used in a new spontaneous imbibition experiment SPx_E2.

Recovery factor (R_f) calculated as percenter original oil in place (*frac. OOIP*):

$$R_f = \frac{S_{w,sp} - S_{w,l}}{1 - S_{w,l}} \quad (58)$$

Table 6: An overview of the spontaneous imbibition experiments applying two-dimensional paperboard models with key properties, as size, boundary condition and the total time before the models where completely imbibed

Experiment	Size parameters [cm] ± 0.1	Number of open areas Width of open area [cm] ± 0.1	Completed time (Hour: Minute)	Delamination time (Hour: Minute)
Group D	Boundary condition: Limited Open Area			
Onset 1	$L = 9.1$ $W = 3.9$	1 $W_L = 0.5$	07: 37	03: 42
Onset 2	$L = 8.9$ $W = 3.9$	1 $W_L = 0.5$	05: 43	
Onset 3	$L = 17.4$ $W = 4.2$	1 $W_L = 0.5$	28: 55	01: 36
Onset 4 ^L	$L = 20$ $W = 16$	1 $W_L = 0.5$	37: 00	
Onset 5 ^L	$L = 4.5$ $L = 4.5$	1 $W_L = 0.5$	01: 30	
Onset 6 ^L	$L = 9.0$ $W = 4.5$	1 $W_L = 0.5$	16: 20	

Onset 7 ^L	$L = 13.5$ $W = 4.5$	1 $W_L = 0.5$	15:00	
Onset 8 ^F	$L =$ $W =$	1 $W_L = 0.5$		
Onset 9 ^F	$L =$ $W =$	1 $W_L = 0.5$		
Onset 10 ^F	$L =$ $W =$	1 $W_L = 0.5$		
Onset 11	$L = 8.5$ $W = 8.5$	1 $W_L = 0.5$	12:40	02:44
Onset 12	$L = 8.5$ $W = 17.0$	1 $W_L = 0.5$	49:13	
Onset 13 ^F	$L =$ $W =$	1 $W_L = 0.5$		
Onset 14 ^F	$W =$ $L =$	1 $W_L = 0.5$		
Onset 15	$L = 6.5$ $W = 6.5$	1 $W_L = 0.5$	14:80	08:20
Onset 16 ^F	$L =$ $W =$	1 $W_L = 0.5$		
Onset 17	$L = 8.5$ $W = 25.5$	1 $W_L = 0.5$	73:30	13:30
Onset 18	$L = 6.5$ $W = 13.0$	1 $W_L = 0.5$	15:14	03:07
Onset 19	$L = 6.5$ $W = 19.5$	1 $W_L = 0.5$	37:44	20:24
Onset 20	$L = 20$ $W = 16$	2 $W_L = 0.5$	35:50	14:17
Onset 21	$L = 20$ $W = 16$	4 $W_L = 0.5$	26:30	04:30
Onset 22	$L = 20$ $W = 16$	8 $W_L = 0.5$	27:00	07:47
Group E	Boundary condition: Radial Outward			
Radial 1	$R_{open} = 0.25$ $R_{closed} = 5.25$		03:52	02:12
Radial 2	$R_{open} = 0.50$ $R_{closed} = 5.25$		02:22	01:32
Radial 3	$R_{open} = 1.00$ $R_{closed} = 5.25$		02:32	
Group F	Boundary condition: One End Open			
Linear 1 ^W	$L = 30$ $W = 6$		25:52	
Linear 2 ^L	$L = 20$ $W = 16$		16:15	01:22
Linear 3 ^L	$L = 20$ $W = 6$		18:53	03:53
Linear 4	$L = 6.5$ $W = 13$		24:07	
Linear 5	$L = 4.5$ $W = 9$		08:09	

^W Includes measurements of change in mass during the spontaneous process. Several of the two-dimensional paperboard experiments are categorized as fail, due to three different reasons: ^L Leakage due to an improper sealing using the epoxy glue. ^F Air trapped at the limited open area resulting in no capillary contact between the water paperboard and the ^F. Challenges observing the saturation front due to camera settings and light conditions also denoted ^F. The time for delamination is included, the cause and effect from delamination are discussed in Chapter 14.2.

14 THE POROUS MEDIA USED IN THE EXPERIMENTS

Observations obtained during the experimental work of this thesis indicate the quality of the setups and the materials used when investigating spontaneous imbibition. Spontaneous imbibition is capillary driven, often giving low pressures and easily affected by alterations in wettability and fluid composition, and is therefore considered sensitive to experimental artifacts. As discussed later experimental artifacts is a possible explanation for the onset phenomena.

14.1 THE SAND PACKED IMBIBITION TUBES

The stability of sand packs regarding of great concern during the experiments applying imbibition tubes. A non-uniform and improperly packed sand pack could possible collapse, causing a change in the properties of the porous medium. The pressure readings obtained during absolute and relative permeability measurements were equal during increasing, and decreasing injection rates for the majority of the sand packs in this thesis, and the sand packs are therefore considered stable, not influenced by an applied differential pressure over the imbibition tube.

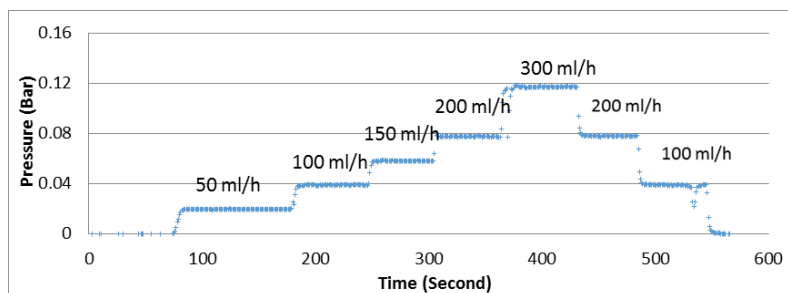


Figure 19: Pressure reading obtained during absolute permeability measurement on imbibition tube SP11. Increasing and decreasing injection rates were used, respectively 50, 100, 150, 200, 300, 200 and finally 100 ml/h.

The sand packs SP12 and SP13 used in imbibition tube experiment SP12_E1, SP12_E2 and SP13 were damaged due to a collapse. The collapse in both sand packs occurred during permeability measurements, due to improperly mounted filters at the inlet side, causing sand to fall into the dead volume of the continuously flushing inlet. The collapsed area in both sand packs can be described as a tunnel of void space. The tunnels started at the inlet side and decreased in size towards the center of the imbibition tubes. The collapses were not caused by the quality of the sand packs. The open tunnels had a significant influence on the spontaneous imbibition processes: water imbibed into the non-collapsed area of the sand pack and displaced a significant fraction of the oil into the open tunnel, resulting in a high ratio of oil produced counter-currently, as shown in **Figure 63** in **Appendix III**. The open tunnel stayed saturated with oil after the imbibition ceased, clearly visible in **Figure 20**. The observations from the three experiments strongly indicate a capillary driven displacement, i.e. spontaneous imbibition: as the water spontaneously imbibe into the unaffected area of the sand pack having a high capillary pressure: a viscous displacement i.e. forced imbibition, would preferably occur through the open tunnel having a lower viscous resistance. Both counter-current and co-current production were observed, indicating that the observations are not caused by an applied pressure. The pressure reading during the permeability measurements in the collapsed sand packs was affected by the injected rate, and a significantly higher permeability was measured.



Figure 20: Picture of imbibition tube SP13 after spontaneous imbibition has finished, the inlet side is to the left. The tunnel created during the absolute permeability measurements is completely saturated with dyed mineral oil (Decane).

14.2 PAPER AS AN ANALOGUE TO ROCK MATERIAL WHEN INVESTIGATING SPONTANEOUS IMBIBITION

The quality of paperboard as analogues to a sedimentary material when investigating spontaneous imbibition was validated by comparing the experimental results with mathematical models based on capillary imbibition. Experiments with one-end open boundary cases and radial-outward boundary cases were tested. In **Figure 21 (a)**, the radial-outward experiments are compared with an idealized model based on the analyses by Mason presented, in **Chapter 4.4**. The radial outward experiments are in agreement with the Mason model. Delamination occurred in experiment Radial 1 and Radial 2. The imbibed area data was therefore normalized with respect to the time for when the delamination occurred, simply removing this experimental artifact from the dataset. Removing the experimental results for the later time is unproblematic for a piston-like saturation front, as the frontal advance is not affected by the outer boundary until it reaches it (Mason et al., 2009b). In **Figure 21 (b)** the one-end open experiments is plotted versus the square root of time, and from the linear relationship between the area imbibed and the square root of time we can conclude that imbibition follows the tendency proposed by Washburn (1921).

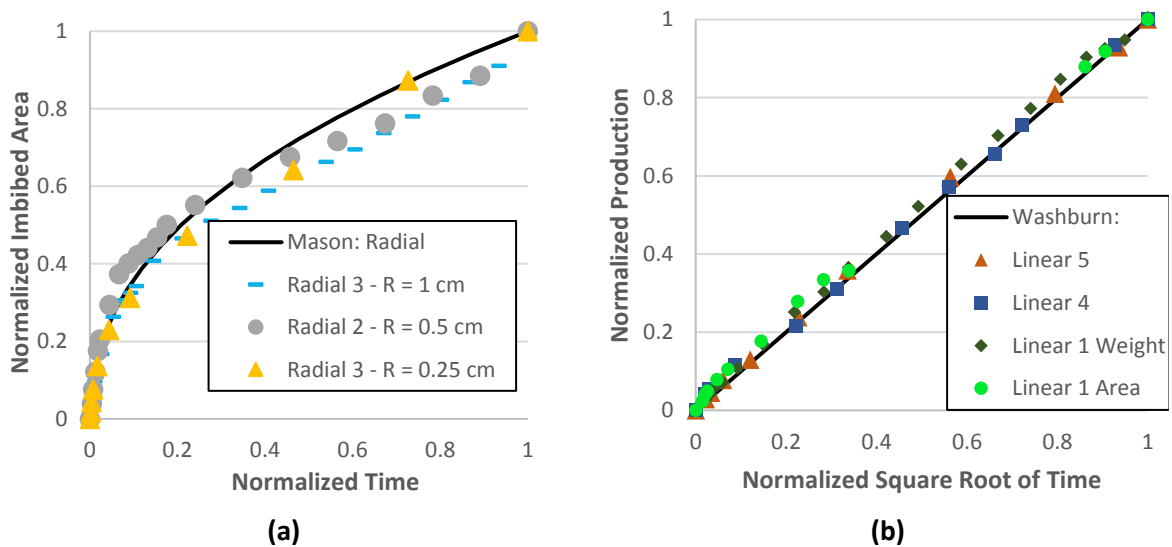


Figure 21: (a) Radial outward spontaneous imbibition into two-dimensional models with varying open diameter, respectively 5, 10 and 20 mm. The black line represents a theoretical curve, calculated using equation (36), an analytical model derived by Mason et al. (2009b). The three two-dimensional models had an equal outer closed radius of 5.25cm. (b) Linear spontaneous imbibition into two-dimensional models with a One End Open boundary condition. Imbibed areas versus square root of time were linear during all three spontaneous imbibition processes. The change in mass was measured during the spontaneous imbibition process into sample Linear 1 (Weight). The black line is a diagonal reference line.

Measurements of the change in mass during the spontaneous imbibition process was obtained for experiment Linear 1 and is compared with the imbibed area in **Figure 21 (b)**. The normalized imbibed area is equal to the normalized change in mass, i.e. the imbibed volume is proportional to the imbibed area.

Delamination was observed in several of the paperboard experiments. The imbibed water behind the saturation front weakened the paperboard, and combined, with the pressure in the wetting phase caused the paperboard to delaminate into two distinct layers. The delamination was observable as a bubble shaped pocket behind the saturation front. The time for delamination was clearly recognizable as an accelerated spontaneous imbibition rate and is shown for four different experiment in **Figure 22**, where the imbibed area is plotted versus time. The acceleration in spontaneous imbibition rate is likely a result of the bubble shaped pocket, reducing the resistance of flow behind the saturation front. In general, the delamination occurred towards the end of the spontaneous imbibition process, and the initial period of spontaneous imbibition is therefore not affected. The period of spontaneous imbibition results until the acceleration occurred is therefore valuable for the discussion of the onset of spontaneous imbibition, as the spontaneous imbibition is not affected by the location of non-flow boundary until the saturation front reaches it (Mason et al., 2009b).

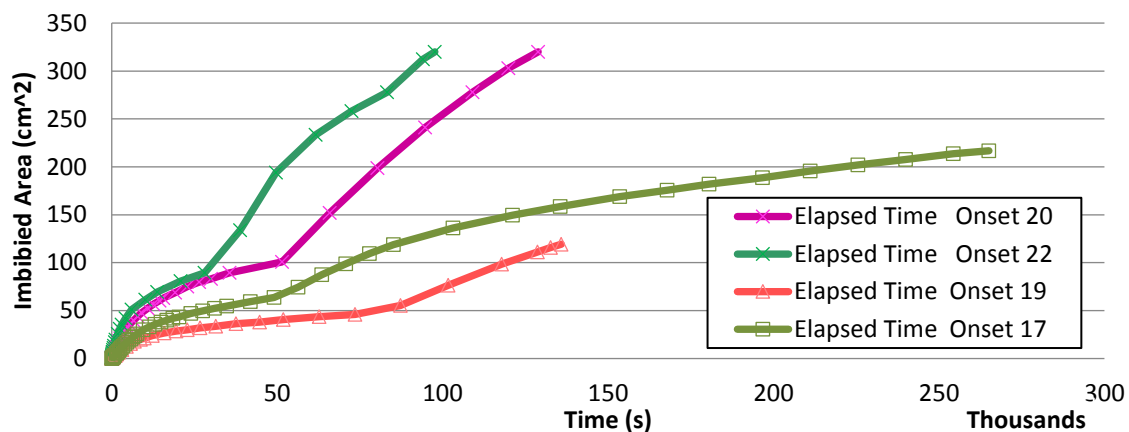


Figure 22: Shows the accelerated spontaneous imbibition due to delamination, as a sudden increased in the imbibed area versus time curve.

Paper and paperboard are a soft fibrous material, produced by pressing together a mixture of fibers and cellulose pulp and drying it into sheets. The mechanical strength of paperboard differs greatly from the mechanical strength of sedimentary rock and is further weakened when soaked in water

15 THE SATURATION PROFILE AND THE SATURATION FRONT SHAPE

It is important to clarify the difference between the shape of the saturation front and the shape of the saturation profile before discussing the two in the context of spontaneous imbibition. The saturation profile is the curve representing the water saturation over the length of the core sample at a time t . A piston-like displacement front is a saturation profile that appears as a step from the water saturation ahead of the front to the water saturation behind the front. The piston-like front can easily be misunderstood as the shape of the saturation front during a linear spontaneous imbibition, however; a uniform saturation front during a linear displacement should be described as planar shaped. The shape of the saturation front is the shape of a surface representing locations in the porous media with an equal saturation, analogous to isobars representing the barometric pressure used in weather forecasts. In **Figure 28** the shape of the saturation front for two-dimensional model experiment Onset 11, Onset 12, and Onset 12 are outlined for different time steps, the front is changing from a radial front, towards a planar front with an intermediate shape as a segment shaped front. The contrast between the imbibed and the non-imbibed area was not affected by the location and the shape of the saturation front, and the saturation profile in the two-dimensional models is therefore considered to be piston-like and independent from the saturation front shape. The same behavior were observed in imbibition tubes, where a piston-like saturation change occurred independent from the saturation front shape for limited period before stabilizing in some experiments, as shown in **Figure 23 (a)**.

The imbibition tube experiments with a low initial water saturation had a distinctly different saturation profiles during the spontaneous imbibition process compared with the imbibition tube experiments without an initial water saturation. The experiments using imbibition tubes packed with a strongly water-wet sand and zero initial water exhibited a true piston-like change in the saturation, as shown in **Figure 23 (a)**. The production of oil started immediately after the experiments were initiated and ceased when the front reached the outlet of the sand pack, confirming a piston-like displacement (Li et al., 2003). A stable uniform saturation front shape was also observed in the imbibition tube experiments with zero initial water and Decane as the non-wetting phase, experiment SP2, SP9, SPI16_E1 and SPI17_E1. The rapid development of the piston-like front and the uniform displacement shows that the experiments are unaffected by any onset period and in agreement with the assumptions for the analytical model for a free spontaneous imbibition boundary case. An overview of the recovery factor, R_f , and ratio produced co-currently and counter-currently, $\frac{Q_{cc}}{Q}$, can be found in **Table 5**. The shape of the saturation front was non-uniform and unstable when the imbibing fluid had an increased non-wetting phase viscosity for, experiment SP3 and SP4. The non-uniform shape resulted in regions of bypassed and entrapped oil. Still, the shape of saturation profile is considered to be piston-like, as the saturation change at the non-uniform shaped front visual appeared as a step change. No spontaneous imbibition was observed for experiment SP15, likely caused by a changed wettability. The influence from altered wettability on the onset period will be discussed later in this thesis.

In experiments with an initial water saturation present, the saturation front was observed as either a step change in saturation or as a global change in saturation. A self-similar front is a mode of saturation

change where the saturation profile is constant and falls between a piston-like displacement mode and a global mode of saturation change. During a global saturation change the saturation is equal over the whole length of the sample and change as a function of time, i.e. the saturation profiles will be a range of horizontal parallel line for each time t (Wardlaw and Yu, 1988). The photos in **Figure 23 (b)** shows a gradual change in color intensity i.e. a non-piston-like saturation profile, as the dyed wetting saturation is increasing and the front is advancing, the saturating profile has resemblances with a self-similar front. The gradually change in color intensity from the imbibing dye is only a qualitative description of the saturation profile, but is reliable to disprove a piston-like or global saturation profile.

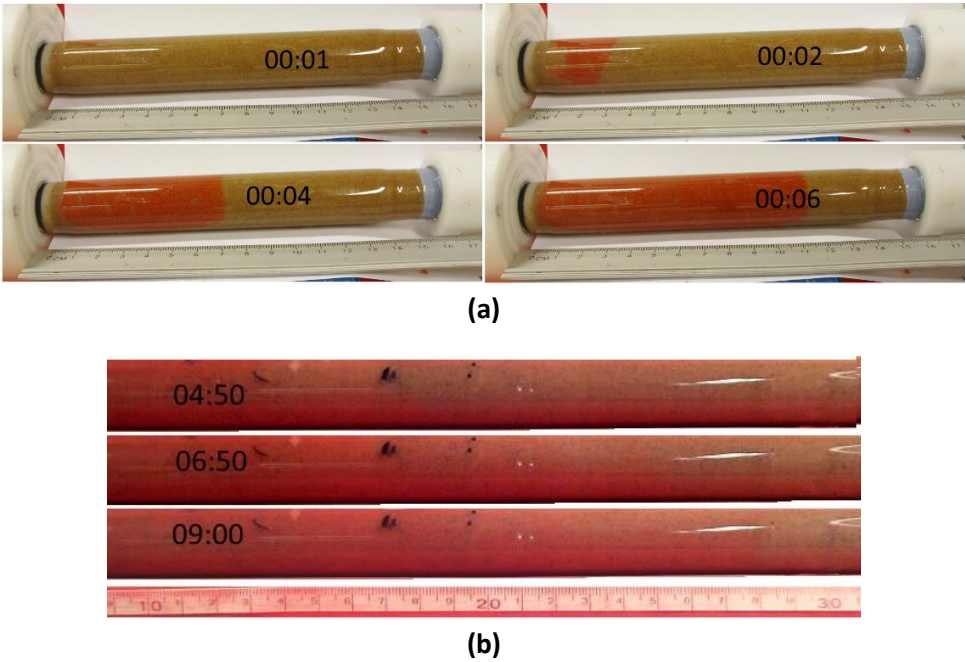


Figure 23: (a) A distinct piston-like saturation profile at different time steps during the spontaneous imbibition process in imbibition tube SP13_E1. The red area is the dyed wetting phase. The front emerging 1.5 cm into the imbibition tube indicate a limited area initialization. (b) A non-piston-like saturation profile during the spontaneous imbibition process in imbibition tube SP10_E2, the location and increase in saturation is very difficult to observe from the photos, it is easier to observe the advancing saturation by combing the pictures into a movie.

An analytical solution for a self-similar mode of saturation change during linear counter-current spontaneous imbibition was derived by Li et al. (2003). The model can be used to estimate the position x for a distinct saturation $S_{w,x}$ at a certain time t , as this saturation is advancing through the sample of a length L . The model shows that all distinct saturations is advancing through the sample at a rate proportional to the square root of time. It is, therefore possible, to construct a map of the self-similar front shape versus time, where the outlined saturation will represent a distinct saturation at different time steps, as done for the piston-like displacement in the two-dimensional models presented in **Figure 28**. The mapping method can be applied on *in-situ* imaging data to confirm a self-similar front, as the distance between the outlined distinct saturation will be linear with the square root of time.

15.1 THE EFFECT OF AN INITIAL WATER SATURATION ON SPONTANEOUS IMBIBITION

The observations from the imbibition tube experiments indicate that some distinct initial water saturations could be influenced by an onset period with slow spontaneous imbibition, which possibly affects the development of the saturation profile. Work by Baldwin and Spinler (2002) showed that the saturation profile was dependent on the initial water saturation. They performed spontaneous imbibition experiments on four strongly water-wet chalk core samples with varying initial water saturation present, respectively 0%, 15%, 22% and 33%, applying magnetic resonance imaging (MRI) to monitor the saturation front and measure the distribution of water. The samples with 33% initial water present had no saturation profile gradient, i.e. a global rise in saturation across the sample. The sample with 22% initial water present had self-similar saturation profile with a low gradient. A piston-like displacement was observed in the samples with 0 and 15% initial water present. The capillary pressure and the relative permeability of both phases are dependent on the saturation. An increased initial water saturation in a water-wet porous media will increase the wetting phase relative permeability, but at the same time reduces the capillary pressure necessary for spontaneous imbibition (Viksund et al., 1998). The net effect of the initial water saturation on the imbibition rate is therefore complicated and will be influenced by the saturation profile as it determines the relationship between the capillary pressure and relative permeability in every location. The presence of an onset could be noticeable at some distinct initial water saturations if the onset affects the balance between the relative permeability and capillary pressure.

The increasing water saturation during spontaneous imbibition in sand packs with initial water present is shown in **Figure 24**. A slow and irregular increase in the wetting phase saturation was observed for two of the sand packs, SP10_E2 and SP11, with similar initial water saturation. SP10_E1 and SP16_E2, with higher and lower initial water saturation respectively, did not exhibit this behavior. The initial production period observed in experiment SP10_E2 and SP11 can, therefore, be addressed as an onset phenomenon.

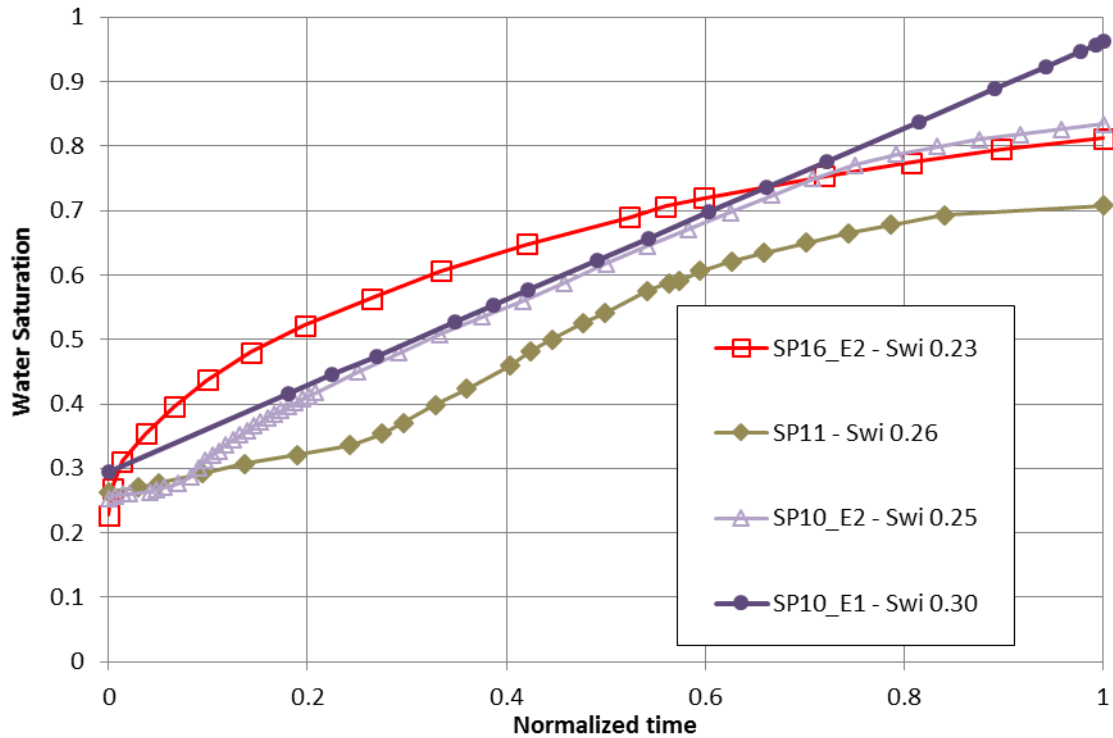


Figure 24. Increasing water saturation during spontaneous imbibition plotted versus normalized time. The initial water saturation is shown on the label.

Experiment SP10_E1 had higher initial water saturation than SP10_E2 and SP11 and was not affected by any onset period. This indicates that experiment SP10_E2 had a sufficient relative permeability and capillary pressure when the spontaneous imbibition process was initiated. SP16_E2 had a lower initial water saturation and was not affected by any onset period either, indicating a mode of saturation change similar to the imbibition tube experiments with zero initial water, where a piston-like saturating profile was visually confirmed.

16 CAPILLARY PRESSURE AND WETTABILITY.

16.1 CAPILLARY PRESSURE ESTIMATED FROM FREE SPONTANEOUS IMBIBITION

The front capillary pressure was estimated for the imbibition tube experiments using the fitting curve method presented in **Chapter 17**. The method is valid for sharp piston-like fronts and was therefore only applied on the imbibition tube experiments with zero initial water present. The results are presented in **Table 7**. Two different types of sand were used in the imbibition tube experiments, with different grain size and grain size distribution. The smaller grains and wider grain size distribution of sand type B used in imbibition tube SP9, SP16_E1 and SP17_E1 resulted in a higher front capillary pressure compared with experiment SP2. The same wetting and non-wetting fluids were used for all type B sand packs and SP2 (type A). The difference in capillary pressure is therefore likely caused by the different characteristics of the sand. The variation in capillary pressure between the imbibition tubes using sand type A is likely caused by the different wetting and non-wetting fluids used. The capillary pressure results obtained during experiment SP3 and SP4 are more uncertain, due to an unstable shape of the saturation front. However, the results match well with the other type A calculated front capillary pressure for experiments using Type A Sand. The Type A Sand experiments were performed in cooperation with and are also previously published by Haugland (2016).

Table 7: An overview of front capillary pressure measured during free spontaneous imbibition in different porous mediums and with different fluids. Type A Sand experiments were performed in cooperation with Haugland (2016). Bentheim Sandstone and Portland Chalk are published results performed by Haugen et al. (2014).

Experiment	Front capillary pressure [<i>kPa</i>]	Wetting Fluid	Non-Wetting Fluid
Type A Sand			
SP2	0.026	Brine	Decane
SP3	0.238	Brine	Marcol 82
SP4	0.396	Brine	DTE FM 32
SP6	0.138	HPAM	Decane
SP7	0.304	Glycerol	Decane
Type B Sand			
SP9	0.072	Brine	Decane
SP16_E1	0.338	Brine	Decane
SP17_E1	0.447	Brine	Decane
Bentheim Sandstone			
SS3 ¹	0.38	Brine	Filtered Lamp oil
SS4 ¹	0.31	Brine	Filtered Lamp oil
Portland Chalk			
CHP 2	166.1	Brine	Filtered Lamp oil
CHP 3	182.1	Brine	Filtered Lamp oil
CHP 4	117.1	Brine	Filtered Lamp oil
CHP 5	109.1	Brine	Filtered Lamp oil
CHP 7	77.7	Brine	Filtered Lamp oil

¹Induction time observed.

A correlation between the front capillary pressure and the onset has not been found for the imbibition tube experiments and literature experiments in this thesis, or elsewhere in the literature. Spontaneous imbibition into the two different types of sand, with zero initial water present, was similar and not

affected by the difference in capillary pressure. Haugen et al. (2014) investigated spontaneous imbibition into cylindrical Bentheim sandstone and Portland chalk cores and estimated the front capillary pressure. The results are shown in **Table 7**. The estimated front capillary pressure was considered unreliable for the sandstone core plug, due to a 20-minute long induction time and rapid spontaneous imbibition when it first started, giving few data points. No onset period was observed in the Portland chalk samples.

16.2 THE EFFECT OF WETTABILITY ON THE ONSET

Investigating how the wettability influenced the onset period was not the main objective of this thesis. However, unexpected behavior was observed in some sand packs, likely due to wettability alteration from the dye added to the non-wetting phase. The results gave insights, and are compared with literature results in the following. The observations indicate that a heterogeneous wettability distributions significantly influence the onset of spontaneous imbibition.

Wettability alteration from strongly water-wet towards strongly oil-wet was observed in experiment SP15. A short aging time, less than 20 minutes, was sufficient to age the sand pack in imbibition tube SP15 to a wettability condition where spontaneous imbibition did not occur. Imbibition tube SP15 was exposed to the imbibition fluid for 36 hours. After 24 hours the outlet tube in the counter-current production collector was adjusted upwards with 2 cm, resulting in an applied hydrostatic pressure of 0.2kPa at the sand pack inlet. The applied pressure of 0.2kPa was not sufficient to overcome the threshold pressure related to the capillary resistance in the sand pack. The applied pressure was comparable to the front capillary pressures estimated for the strongly water-wet sand packs, given in **Table 7**. Imbibition tube SP15, therefore, exhibits strongly oil-wet behavior. Imbibition tube SP15 had zero initial water present when it was exposed to the dyed non-wetting phase, opposed to the other imbibition tubes where initial water was present when the dyed non-wetting phase was injected.

Visual observations of the saturation front during imbibition tube experiments SPI17_E2 indicates a mixed-wet wettability condition. A limited forced imbibition was started due to no observable spontaneous imbibition for the first two hours of the experiment. The non-wetting dyed Decane was displaced out of 1 centimeter long section, causing a distinct piston-like saturation front starting from 1 cm length. Internal redistribution of the fluids due to spontaneous flow was visually observed in the first 15 hours after the forced imbibition process was ended, **Figure 25**. The redistribution of the non-wetting phase occurred due to spontaneous non-wetting phase flow, and could only occur if an area of the sand pack is to some degree oil-wet. When the redistribution occurred wetting phase was also produced co-currently, which can only occur if an area of the sand pack is water-wet. The wettability in sand pack SPI17_E2 should, therefore, be described as mixed, a type of wettability where the wettability is dependent on the pore size (Salathiel, 1973). The counter-current flow is denoted as internal due to no observed counter-current production. During the first 24 hour, 1 ml of dyed Decane was produced co-current at the outlet. During the next 48 hours additional 1,4 ml of dyed Decane where produced, a total of 7 ml of dyed Decane was produced after one week. The production rate was extremely slow and irregular.

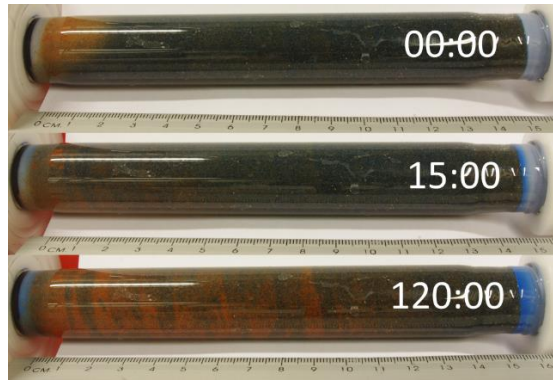


Figure 25: Shows the saturation distribution during spontaneous imbibition process in SP17_E2 at different time steps (hh:mm). The picture at zero hour shows the piston-like front formed during forced imbibition. The 15-hour picture shows the redistribution of the non-wetting phase (blue). The last picture shows scatter wetting phase saturation.

The wettability conditions caused a distinct pattern of oil through the sand pack. Dark areas, in the shape of rings, indicated a high saturation of the dyed Decane. The dark areas became more dominant towards the outlet, exhibiting an alternating pattern with dark and light areas, which gradually disappeared, indicating a non-imbibed area. The method used for packing of the sand could have resulted in a heterogeneous distribution of the sand grains size through the sand pack, resulting in layers of larger and smaller grains. A heterogeneous distribution of the sand grains would affect the distribution of the fluids in a mixed-wet sand pack, where the wettability depends on the pore size.

The slow and irregular co-current production of the non-wetting phase, shown in **Figure 26**, can be a result of the alternating layers of wettability conditions. The wettability condition and the high oil saturation in darker areas represent high resistance to spontaneous imbibition, resulting in periods of slow production. These periods can be compared to several literature spontaneous imbibition experiments, exhibiting induction times with very slow or zero spontaneous imbibition.

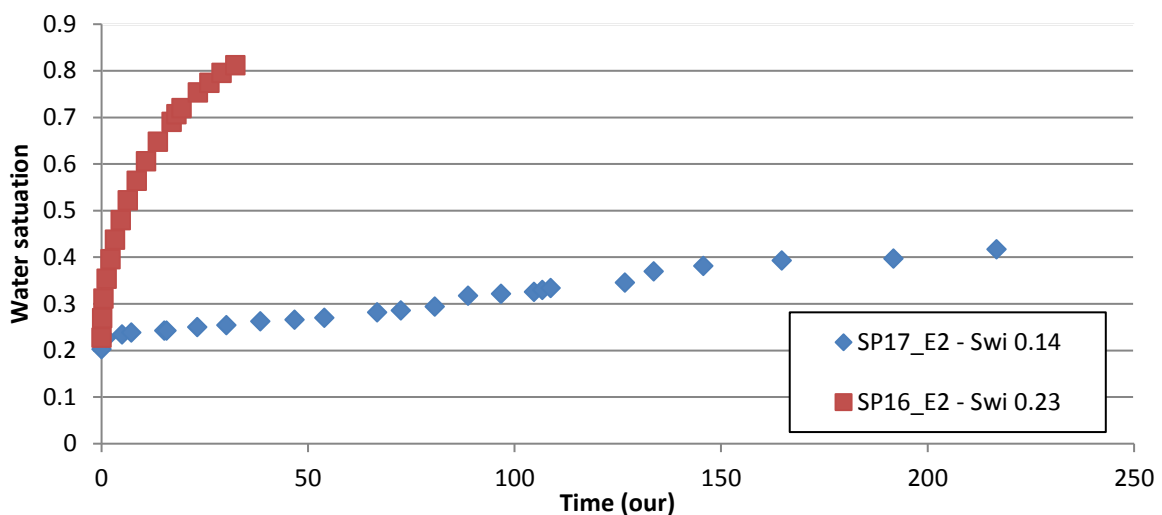


Figure 26: Increasing water saturation during spontaneous imbibition for experiment SP16_E2 and SP17_E2. Mixed-wet sand pack compared to strongly water-wet sand pack.

Wettability alterations with two different aging techniques resulted in significantly different induction times during spontaneous imbibition, observed by Fernø et al. (2010). The spontaneous imbibition results are shown in

Figure 27. A dynamic wettability alteration method was applied on two cores, resulting in no observable induction time. The dynamic method was suggested to give a more uniform alteration in wettability across the sample, compared with the conventional static aging method used on the two other cores. The non-uniform wettability alteration in the static aged cores can explain the difference in induction time: where the outer part of the cores exhibited a higher degree of wettability alteration than the inner part of the cores, giving an outer and inner layer of wettability, similar to the observations in experiment SPI17_E2. The outer layer represents a resistance towards spontaneous imbibition, being less water-wetted, until a sufficient wetting phase conductivity has been established. A high capillary pressure in the inner part of the core accelerated the spontaneous imbibition process is less affected by the wettability alteration, due to a higher capillary pressure. Fernø et al. (2010) used the spontaneous imbibition experiments to estimate the wettability alteration on four core plugs, using the Amott Harvey index to quantify wettability. The two wettability alteration methods resulted in equal Amott Harvey index (I_{AH}), but widely different spontaneous imbibition behavior. The rate of spontaneous imbibition is also an important factor describing wettability (Morrow et al., 1994), but does not impact the Amott-Harvey method, described in **Chapter 4.6**.

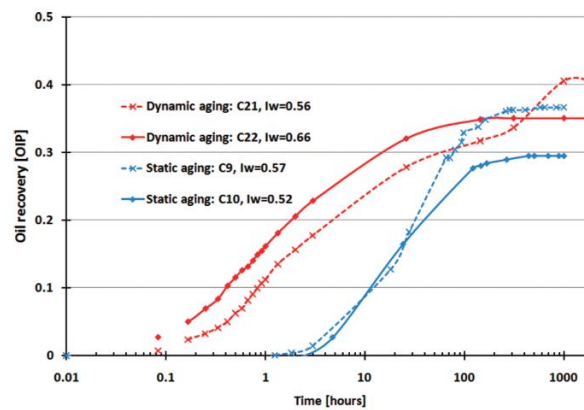


Figure 27: Comparison of induction time and production rates between four cores with a similar I_{AH} . C21 and C22 are aged dynamically and C9 and C10 statically. The statically aged cores had significant long induction time. From Fernø et al. (2010).

The wettability distribution through a core plug was shown by Graue et al. (2002) to be dependent on the wettability alteration method, and the induction times during spontaneous imbibition were related to the degrees of wettability alteration. Nuclear-tracer imaging was applied to measure the wettability heterogeneity as the distribution of the Amott-Harvey water indices on chalk core plugs after wettability alteration. Two different dynamic wettability alteration methods were tested: a unidirectional method where crude oil was injected into chalk cores from one direction, and a multidirectional method, injecting crude oil from both directions, the latter is the same applied by Fernø et al. (2010). The unidirectional method resulted in a significant heterogenic distribution of the Amott-Harvey water indices when applied on five core plugs stacked together. The Amott-Harvey water indices δ_w varied from 0.37 at the inlet side to 1 at the outlet side, over a total length of 22.8 cm. The observed induction times during spontaneous imbibition of the five core plugs were corresponding to the degrees of wettability alteration. The observation supports the proposed explanation of a heterogenic wettability alteration causing the induction times observed in the experiments performed by Fernø et al. (2010), and is a possible explanation for limited area initialization fronts observed in spontaneous imbibition experiments applying PET *in-situ* imaging, discussed in **Chapter 19**.

17 DEVELOPING SATURATION FRONT SHAPE

The trajectory and shape of the saturation front during spontaneous imbibition is assumed to be uniform and symmetrical, advancing perpendicular outward from the wetted surface of the sample. However, *in-situ* imaging has revealed that saturation front shape and trajectory contradicts the assumption of a uniform front shape in several spontaneous imbibition experiments. Two different categories of deviated saturation front shapes have been suggested; the limited area shaped front and the segment shaped front (**Chapter 7**). The deviated front shape and trajectory is problematic when applying the Darcy model to derive scaling equations, as the flow rate will be dependent on the interfacial area of the saturation front, and this area will be unpredictable and varying.

In this thesis, two-dimensional spontaneous imbibition models were designed to visualize and provide a detailed description of local flow patterns during the onset period, by applying a special boundary condition to forcibly cause a limited area saturation front. The models resemble a longitudinal section of a three-dimensional core, equivalent to the *Region of Interest* applied on *In-situ* visualizations of spontaneous imbibition in **Chapter 19**. The limited area models were used to study how the developing saturation front shape behaved before and after reaching the closed side boundaries, and how the viscous resistance location affected the spontaneous imbibition rate, further discussed in **Chapter 18**.

The special boundary case used in the limited area models produced deviating saturation fronts in both categories. The saturation front was radial and unaffected by the side no-flow boundary until it reached it, then a segment-shaped front formed, and advanced through the rest of the model becoming increasingly planar shaped. A reduced distance from the limited open area to the side no-flow boundary affected the time for when the transition from a radial front to a segment-shaped front occurred. The transition from a radial-shaped front occurred when the saturation front progressed to the corners of the paper sample, and is therefore simple to determine. It is more challenging to determine the time for transition from a segment to a planar-shaped saturation front, as the front shape is gradually evolving. Analytical models propose that the ratio between the length of the segment-shaped front and the width of the sample will converge towards one when the saturation front has advanced a distance equal to the width of the sample. This transformation behavior was confirmed in the two-dimensional models applying one single limited open area, shown in **Figure 28** and **Figure 30**. This shows that the spontaneous imbibition process was unaffected by the position of the closed side boundaries until the saturation front reached it.

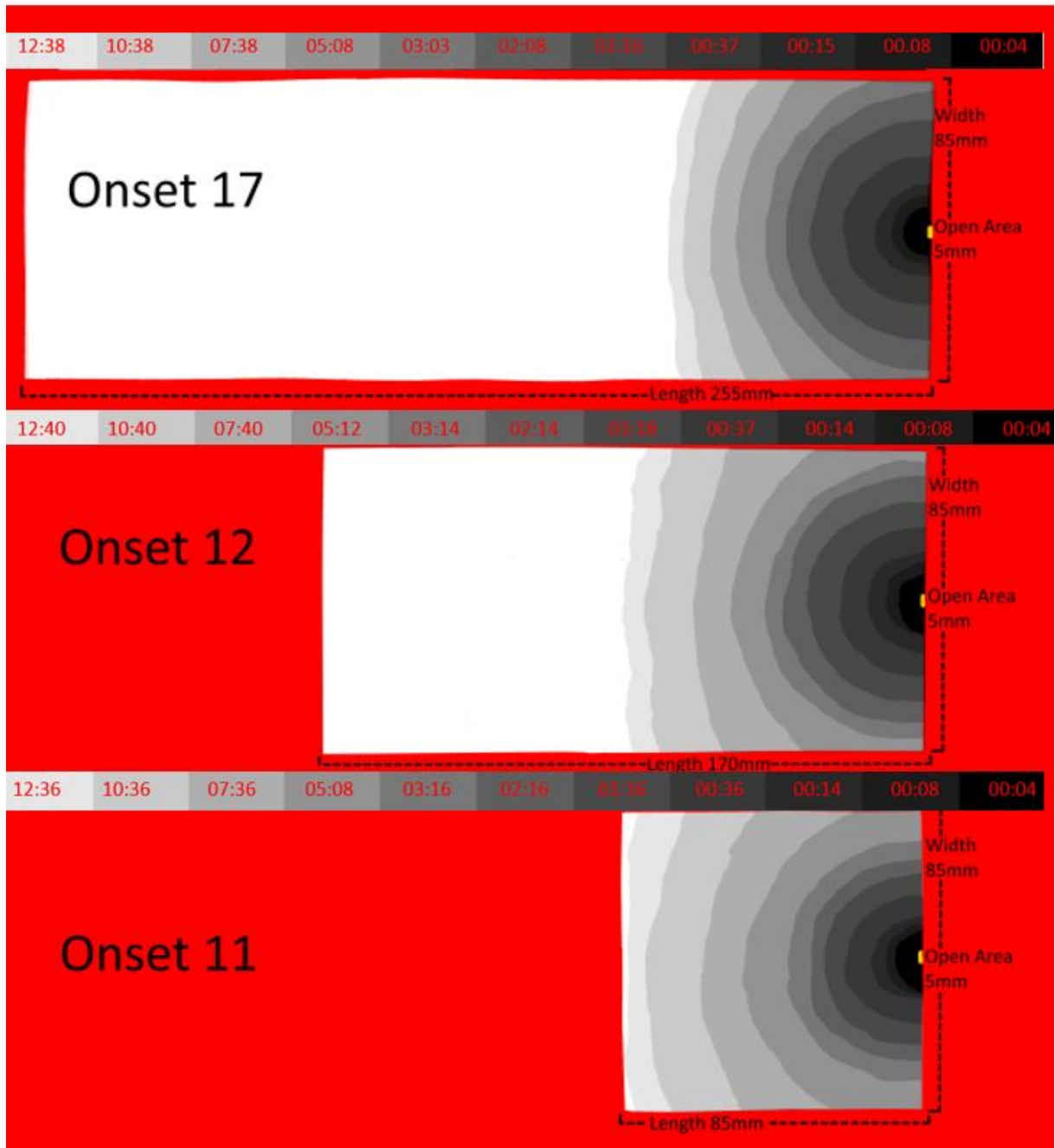


Figure 28: Limited open area spontaneous imbibition experiment Onset 11, Onset 12 and Onset 17 The figure shows the shape and area behind the saturation front at different times (hh:mm) as a decreasing intensity of gray. The different time steps and intensity of gray are shown in the bar above each experiment. The three experiments had an equal width and open area, but varying rectangular aspect ratio ($\frac{Length}{width}$), respectively 1, 2 and 3.

17.1 THE INITIAL RADIAL PERIOD OF SPONTANEOUS IMBIBITION

The saturation front during the initial period of spontaneous imbibition into the two-dimensional models with one single open area was radial in all the samples and behaved unaffected by the closed no-flow boundary until it reached it. The saturation front started out from the limited area and advanced outward as a half circle. The influence of the width of the samples i.e. the distance between the limited open area and the closed side boundary, on the time for saturation front transformation,

from a radial to segment shape is illustrated in **Figure 29**, comparing two limited open area experiments. A dotted blue line marks the size of the smaller Onset 3 experiment above Onset 16. If this marked line was the outer boundary of Onset 16 the front would be transforming to a plane shaped front at the time step marked with the yellow arrow, (17 minutes). The marked time step is comparable to the time for when the saturation front in experiment Onset 3 is transforming from a radial to a plane shaped saturation front.

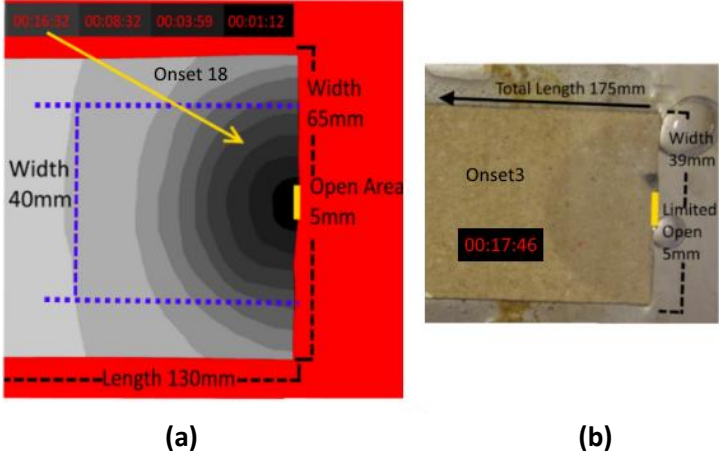


Figure 29: Limited open area spontaneous imbibition experiment Onset 3 and Onset 18. (a) Picture of experiment Onset 3 at the time 00:17:46, when the saturation front is transforming from a radial to a segment shape. (b) Experiment Onset 18 with the width of Onset 3 marked as a blue dotted line. The saturation front position is outlined for different times as a decreasing intensity of gray. The radial saturation front at the time 00:16:32 is marked with a yellow arrow. Onset 18 would be transforming to a dragging shape front if it had a width equal to the width of sample Onset 3.

Six of the experiments with one single limited open area are illustrated in **Figure 28** and **Figure 30**. The position of the saturation fronts is outlined as different intensity of gray for different time steps. The transition from a radial front to a segment shaped front occurred after approximately 3 hours, for the three experiments shown **Figure 28**. The transition from a radial front to a segment shaped front occurred after approximately 1.5 hours in the narrower models presented in **Figure 30**. The development of the saturation fronts illustrated in **Figure 28** and **Figure 30** shows the tendency in all models with one single limited open area. The transition from a radial to a segment shaped saturation front was controlled by the distance from the open area to the closed side boundary.

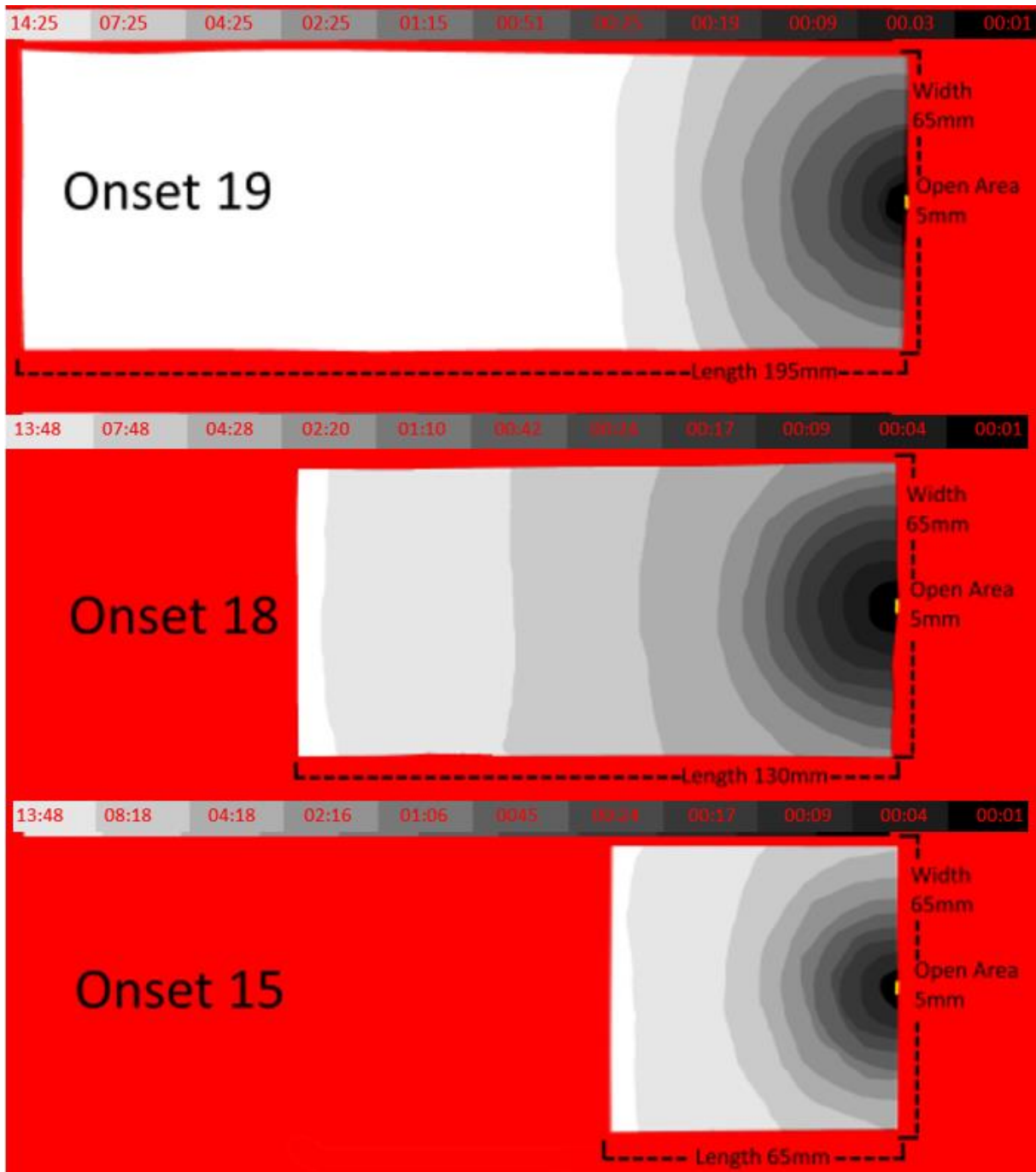


Figure 30: Limited open area spontaneous imbibition experiment Onset 15, Onset 18 and Onset 19. The figure shows the shape and area behind the saturation front at different times (hh:mm) as a decreasing intensity of gray. The different time steps and related intensity of gray are shown in the bar above each experiment. The three experiments had an equal width and open area, but varying rectangular aspect ratio ($\frac{Length}{Width}$), respectively 1, 2 and 3.

17.2 TRANSITION FROM A RADIAL TO A DRAGGING SHAPED SATURATION FRONT

The spontaneous imbibition process is not affected by a closed boundary until it reaches it, this is evident in the two-dimensional paperboard models where the shape of the saturation front is transforming when the saturation front reaches the closed side boundary. The shape of the saturation front during the spontaneous imbibition process in the limited open area models are determined by the geometrical shaped of the samples. A mathematical model for the transformation from a segment

shaped front to a planer shaped front during a limited area initialization has been derived. The radially outward expanding saturation front from the initialization area should be described as a plane shaped front when the length of the smoothed saturation front S is close to the width W of the sample. The length of a smoothed saturation front can be estimated by assuming a perfect radial growth after the front has reached the closed side boundary, resulting in a circle segmented shaped saturation front. The length of the smoothed segment shaped saturation front S can be calculated as the arc length of a circle with the radius r , where r is the distance from the limited open area to the smoothed saturation front and α is the angle inscribed between the limited open area and the ends of the segment-shaped front in radians. **Figure 31** shows an overview of the different geometrical variables. A smoothed saturation front is the best fit of a segment shaped line representing the true saturation front.

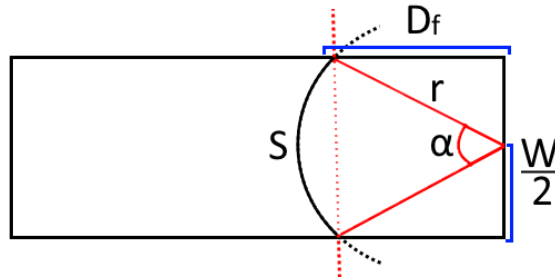


Figure 31: An idealized saturation front with the length S in a sample with the width W . r is the distance from the limited open area to the saturation front, D_f is the distance the saturation front has advanced along the closed side boundary. α is the angle inscribed between the limited open area and the ends of the line segment.

The segment length is given by:

$$S = r * \alpha \quad (59)$$

, substituting with

$$r = \sqrt{D_f^2 + \left(\frac{W}{2}\right)^2} \quad (60) \quad , \text{ and} \quad \theta = \pi - 2\arctan\left(\frac{D_f}{W}\right) \quad (61)$$

gives:

$$S = \left(\pi - 2\arctan\left(\frac{D_f}{W}\right)\right) * \sqrt{D_f^2 + \left(\frac{W}{2}\right)^2} \quad (62)$$

Equation (62) shows that the length S of the smoothed segment shaped saturation front is only dependent on the width W of the sample and the length D_f , where D_f is the distance the saturation front has advanced along the closed side boundary. The ratio of the saturation front length S to the width W is plotted versus the ratio of advanced distance D_f to width W in **Figure 33**. Giving a general

model for when the length of the segment-shaped saturation front S is equal to the length of a planar shaped front, with the length W . The theoretical difference in length between a plane-shaped front and segmented shaped front is less than 4 percent when the advanced distance D_f is equal to the W width of the sample. The experiments in **Figure 28** and **Figure 30** have rectangular aspect ratios ($\frac{Length}{Width}$) of 1, 2 and 3, and it is, therefore, simple to recognize that the saturation fronts become close to a planar -shaped front when the advanced distance is equal to the width of the sample. The general models assume that the saturation front is growing with a perfect radial shape with an initial radius of zero.

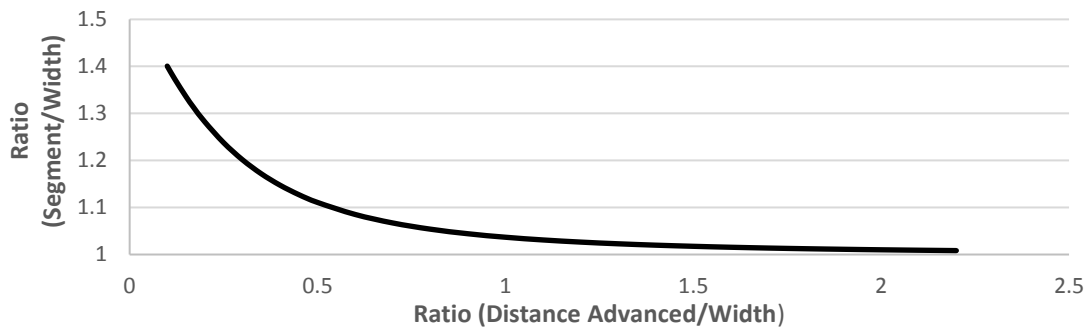


Figure 32: The transition from a segment to a plane shaped saturation front. The ratio of the saturation front length S to the width W is plotted versus ratio of the advanced distance D_f to width W .

This model describes how a radially growing expanding saturation front transformer after it reaches the closed side boundary when only affected by the geometrical shape of the sample. The radially growing saturation front should transform towards a planar shaped saturation front when the distance between the limited initialization area the and the saturation front is equal to the width of the sample, or the diameter of a cylindrical core. However, *in-situ* imaging of the saturation front during spontaneous imbibition by Fernø et al. (2013) and Wickramathilaka et al. (2010) shows that the transformations are not necessarily occurring, indicating that the spontaneous imbibition process is affected by the closed side boundary before the saturation front reaches it. Heterogeneous wettability is a proposed explanation and is future discussed in **Chapter 16.2** and **19**. A transforming saturation front was observed by Akin et al. (2000), behaving as anticipated by the proposed model, shown in **Figure 33**.

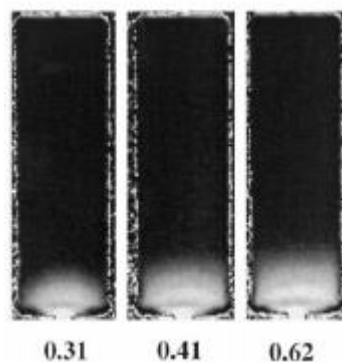


Figure 33: A transforming saturation front observed by CT images. Black indicates no water, white indicates fully water saturated. From Akin et al. (2000).

17.3 MULTIPLE OPEN AREAS

When the two-dimensional models exhibited multiple open areas, the saturation fronts during the initial period of spontaneous imbibition into consisted of several individual radial saturations fronts. The number of radial saturation fronts was equal to the number of open areas. The development of a planar front was influenced by the number of multiple areas, due to the reduced distance between open areas and the closed boundary and the subsequent merging of the multiple imbibed areas. The two-dimensional models with multiple numbers of limited open areas were equal, except the number of open areas, Onset 20 had two open areas, Onset 21 had four, and Onset 22 had eight open. The position of the saturation fronts in the three experiments are outlined as different intensities of gray for different time steps in **Figure 35. Table 11** in **Appendix III** is an overview of the size of the models and the time for when the areas merged.

The individual areas were observed expanding at a varying rate. The exact reason behind this behavior is unknown. A possible explanation is an uneven distribution of production of air and imbibing water between the open areas. Meaning that some of the areas imbibe more wetting phase than it produces the non-wetting phase, and the excess volume of the non-wetting phase is flowing out through another open area. This was observed in experiment Onset 20, shown in **Figure 34**. The imbibed area marked as *A* expanded quicker than the imbibed area marked as *B* where the produced air formed a bubble at the inlet. No produced air was observed at the area *A* inlet. Other possible explanations are the uncertainty inherent the width of the small open areas being 0.5 mm. Or small damages in the paperboard during the preparation procedure, causing limited areas of delamination and rifts close to the open area, reducing the viscous resistance. This explanation can explain differences in the rate of spontaneous imbibition observed in the two-dimensional models with one single limited open area, **Figure 50 - 58** in **Appendix III**.



Figure 34: Spontaneous imbibition into a two-dimensional model with two open areas, Onset 20. The arrow points at a bubble of produced air at the A side inlet. The A imbibed area is smaller than the B imbibed area. The picture is taken 1 hour and 7 minutes after the experiment was initiated.

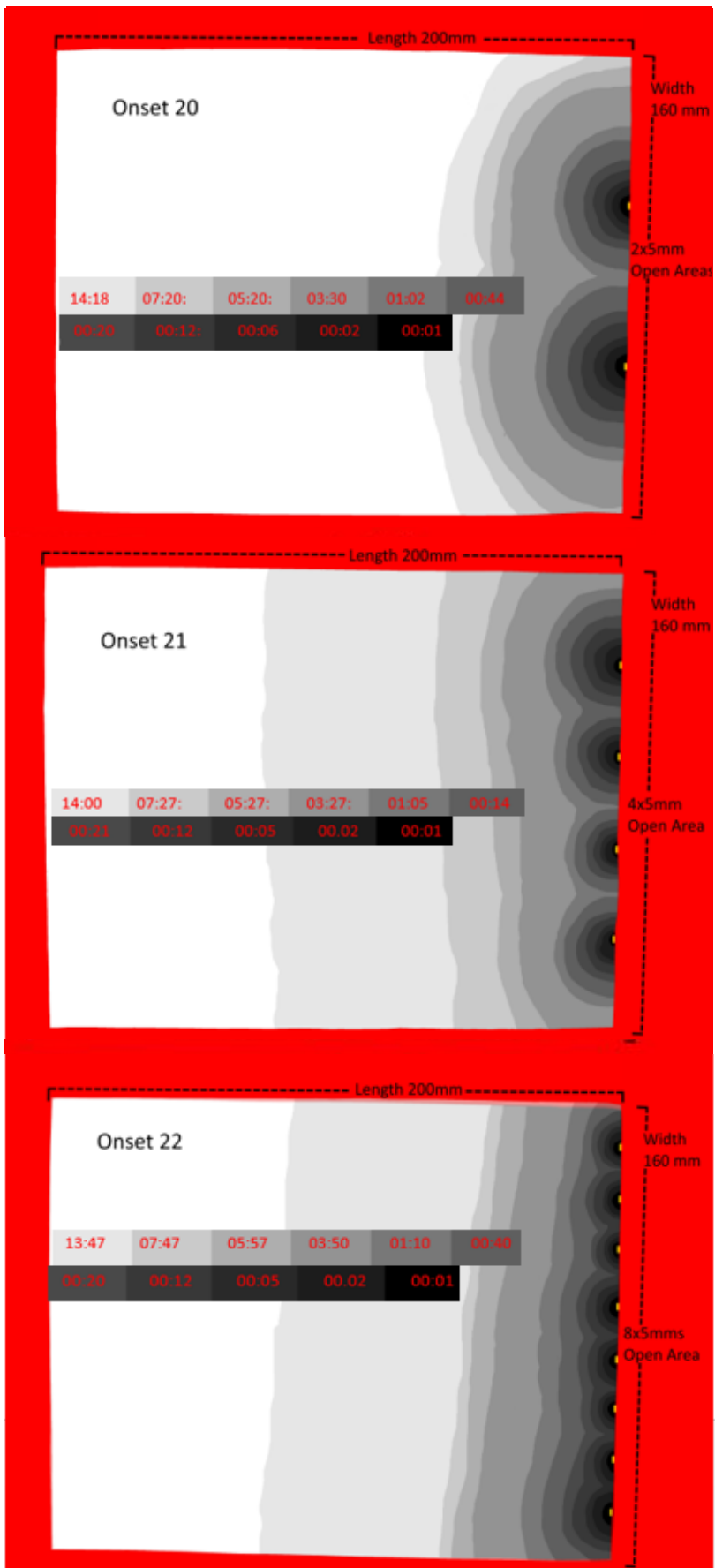


Figure 35: Limited open area spontaneous imbibition experiment Onset 20, Onset 21 and Onset 2. The Figure shows the shape and area behind the saturation front at different times (hh:mm) as a decreasing intensity of gray. The different time steps and related intensity of gray are shown in the bar above each experiment. The three experiments had equal width an length, but a varying number of limited open areas, respectively 2, 4 and 8.

18 THE VISCOUS RESISTANCE LOCATION

A total of 12 onset experiments were successfully implemented, the shape of the spontaneous imbibed area versus time curve was conclusive, with a high degree of reproducibility between experiments. The method used to estimate the imbibed area resulted in low uncertainties, except during the initial period when few pixels were imbibed. The method used to estimate the imbibed area and the related uncertainty is clarified in **Chapter 12.2**, and was time-consuming during analysis. A matlab or python script to do this task would be convenient, but was considered to be challenging to develop due to the variety of colors in a dry paperboard, making it difficult for a simple script to discriminate the non-imbibed area and the imbibed area.

A selection of experimentally obtained result is presented in this part of the thesis illustrating the general behavior. The remaining results and uncertainty estimates are included in **Appendix III**. The uncertainty estimate for the imbibed area in experiment Onset 22 is shown in **Figure 36**. The uncertainty is assumed to be related to the length of the saturation front, and the relative uncertainty is therefore high during early times of the experiments. The relative uncertainty was less than 3 percent for all experiments after one hour. Experiment Onset 22 had a particularly large circumference at the initial period of the experiment, due to the multiple numbers of open areas. The relative uncertainty estimate of experiment Onset 22 is, therefore, higher than in other experiments.

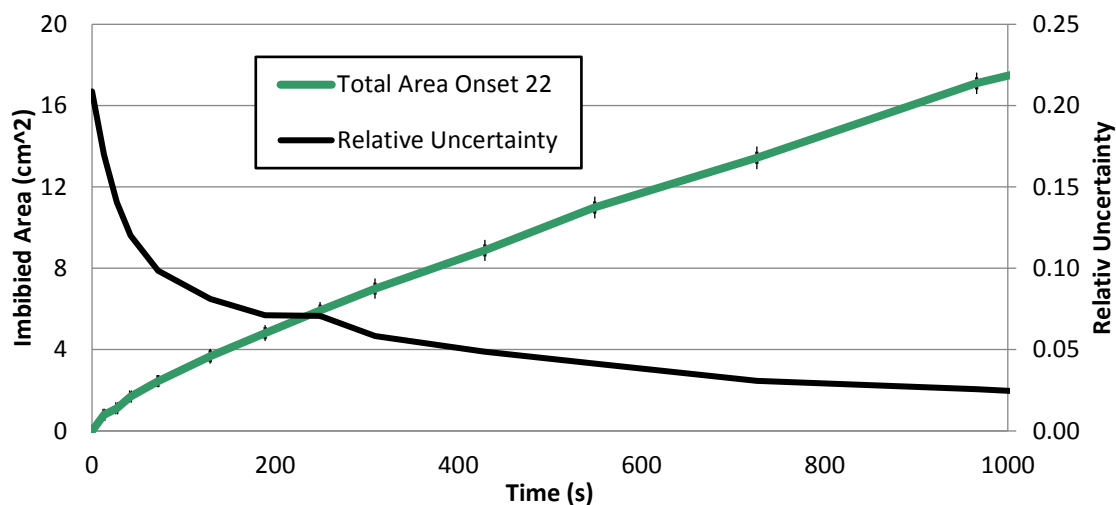


Figure 36: Limited open area spontaneous imbibition experiment Onset 22, with eight open areas. The figure shows imbibed area (cm^2) versus time (seconds) and the estimated absolute uncertainty. The relative uncertainty is plotted versus a secondary y-axis. The plot is limited to the first 1000 seconds of the experiment.

The general trend of the spontaneous imbibition process with one single limited open area is conclusive. The viscous resistance location is associated with the flow through the limited open area, affecting the relationship between time and the imbibed area for the initial three hours of the experiments, the spontaneous imbibition process exhibits a close to a linear relationship between time and imbibed area for the first hour. The initial period where the total viscous resistance is dominated by the flow through the limited open area caused a distinguished slack in the square root of time plots compared with diagonal reference lines for the complete experiments. The slack in the square root of time plot is notable in **Figure 37**, containing the experimental results from the three limited open area

models least affected by delamination. The slack in the square root of time curve, due to the forced onset phenomenon is of special interest when investigating the onset period of spontaneous imbibition; as the shape of the curve indicates that the location of the significant contribution to the total viscous resistance, and how the viscous resistance is developing, denoted as the viscous resistance location. A methodology investigating the affect from the onset by comparing the spontaneous imbibition curves with analytical curves is discussed in **Chapter 20**.

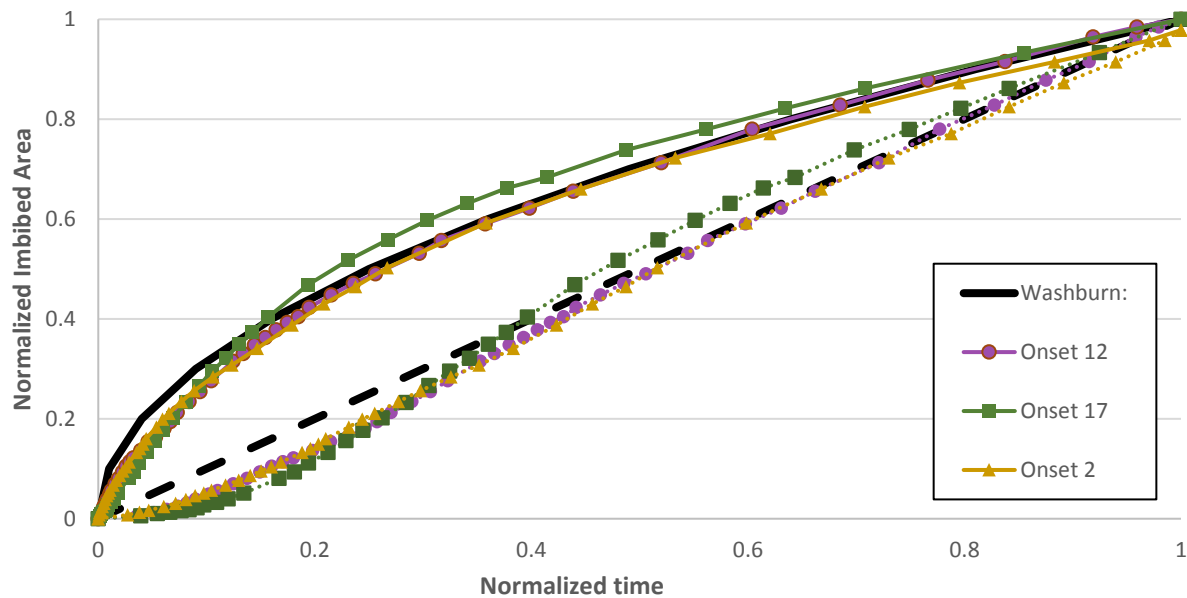


Figure 37: Limited open area spontaneous imbibition experiment Onset 2, Onset 12 and Onset 17. The figure shows normalized imbibed area versus normalized time as solid lines, and versus normalized square root of time as dotted lines. The normalization is with respect to the time for when the sample was completely imbibed for Onset 12 and Onset 2, and for when the delamination occurred for Onset 17. The experiments are compared with an idealized model for linear spontaneous imbibition.

As the front progress away from the inlet a larger part of the viscous resistance become associated with the distance between the open area and the saturation front position, and the spontaneous imbibition rate transformed gradually towards the square root of time relationship proposed by Washburn. The initial period of linear with time spontaneous imbibition ended after approximately 1 hour. **Figure 38** shows the normalized imbibed area versus the normalized time with respect to the first hour of the spontaneous imbibition process. The results are in agreement with the spherical Darcy model for spontaneous imbibition derived by Mason et al. (2012), verifying that most of the viscous resistance is associated with the small inlet area. The results can be compared with **Figure 21 (a)**, where radial two-dimensional models are matched with the radial Darcy model for spontaneous imbibition derived by Mason et al. (2009b), where the inlet area is larger and therefore behaves less linear with time.

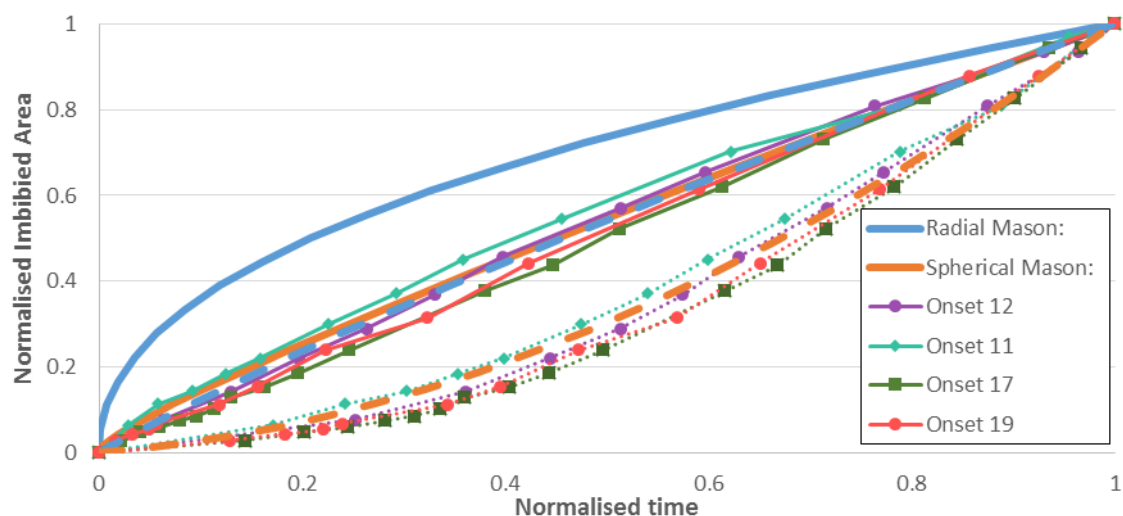


Figure 38: Limited open area spontaneous imbibition experiment Onset 11, Onset 12, Onset 17 and Onset 19. The figure shows normalized imbibed area versus normalized time as solid lines, and versus normalized square root of time as dotted lines. The normalization is with respect to the first hour of the experiments. The experiments are compared with idealized models for radial and spherical spontaneous imbibition.

Entrapment and bypassed non-wetting phase due to a non-uniform and unstable saturation front was observed in the imbibition tube experiments SP3 and SP5, with increased wetting phase viscosity. The regions of entrapped oil were located close to the inlet as globules. The production of the wetting phase was close to linear with time during the whole experiment, indicating that the significant contribution to the viscous resistance was related to the pathway for the wetting phase limited by the regions of entrapped oil. Identical behavior was observed in experiments performed by Vabø (2016), with Decane as the non-wetting phase and the same imbibition tubes, shown in Figure 9.

The magnitude of the gradually increasing viscous resistance associated with the distance from the limited open area to the saturation front was the significant contribution to the total viscous resistance after 3 hours after imbibition initiation. This resulted in a linear relationship between the imbibed area and the square root of time. **Figure 39** gives an overview of the total imbibed area at different time intervals during the spontaneous imbibition process in experiment Onset 12, highlighting how the development of the viscous resistance affects the spontaneous imbibition behavior over time. The upper left plot **(a)** is the first hour with a linear relationship between time and imbibed area. The upper right plot **(b)** is the transformation period, where a linear square root of time relationship with the imbibed area is developing. The lower left plot **(c)** is the square root of time period of the spontaneous imbibition process, starting after the transformation period. The lower right plot **(d)** is the complete spontaneous imbibition process, where the effect from the initial period with constant spontaneous imbibition rate has a notable effect, causing a slack in the square root of time line compared with the diagonal reference line.

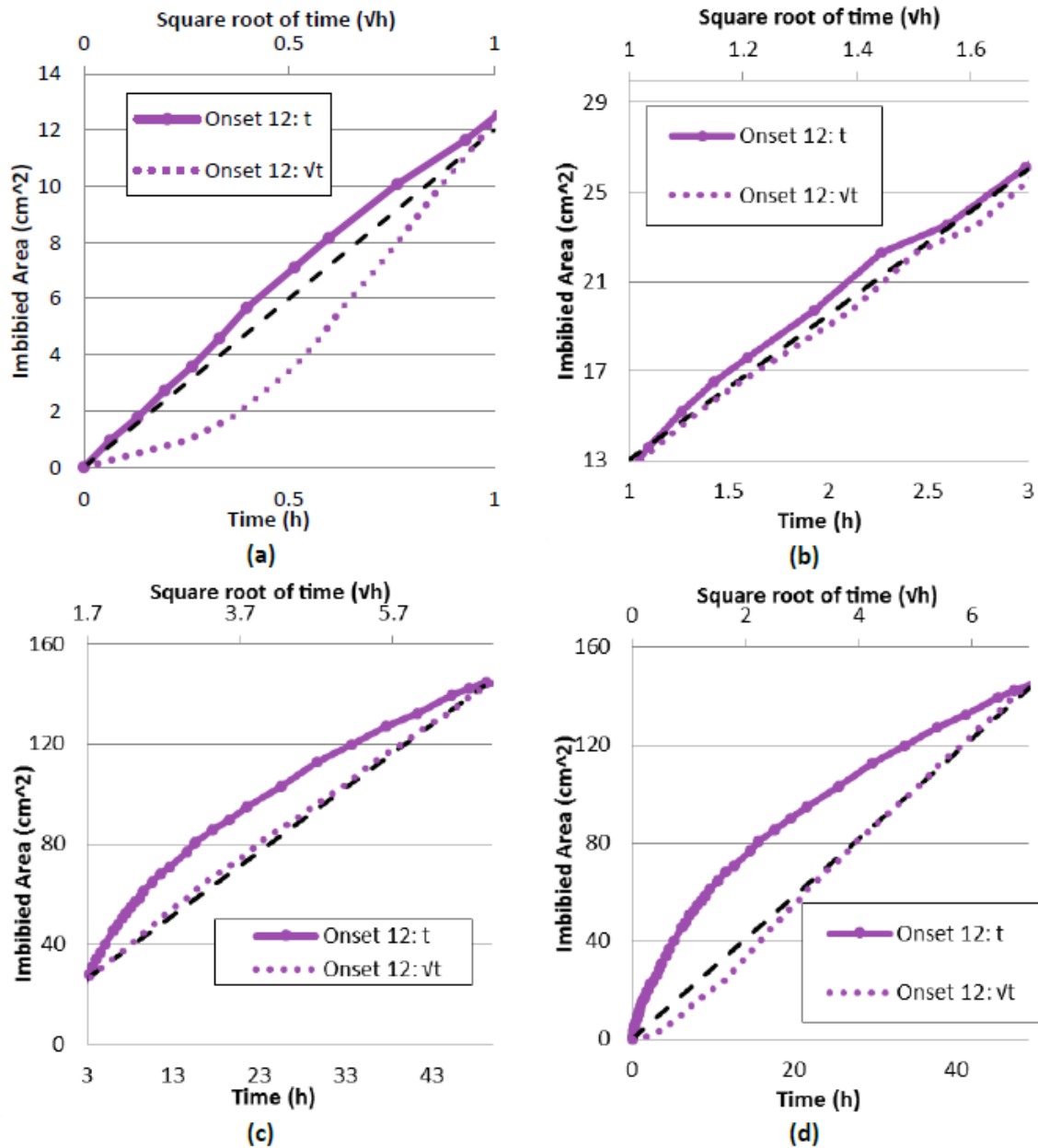


Figure 39: Limited open area spontaneous imbibition experiment Onset 12. The four figures show the total imbibed area at different time intervals to highlighting the different periods: The solid line is the plotted versus time (primary x-axis) and the dotted line is plotted versus the square root of time (secondary x-axis). The black dashed line is a diagonal reference line. (a) The first hour of the experiment, the imbibition is linear with time. (b) The period from 1 to 3 hours of the experiment, a transformation period. (c) The period from 3 to 49 hours i.e. the end of the experiment, the imbibition is linear with the square root of time. (d) The complete experiment.

18.1 MULTIPLE NUMBERS OF LIMITED OPEN AREAS

The number of open areas affected the imbibed area versus time during the initial period of spontaneous imbibition into the two-dimensional models. The relationship between time and imbibed area was similar in models with only one and multiple limited open areas. In Onset 20, two open imbibed areas existed, and each of the two areas expanded outward with an increase in area proportional to the time until they merged after 3100 seconds, **Figure 40**. The merged area continued to grow with an increase in area proportional to the time for the first hour of the spontaneous imbibition process. This period resulted in the distinguished slack in the square root of time plot for the complete spontaneous imbibition process, **Figure 41**. The two imbibed areas in experiment Onset 20 expanded with a dissimilar rate where Area A expanded faster than Area B. Possible explanations for this difference is briefly discussed in **Chapter 17.2**

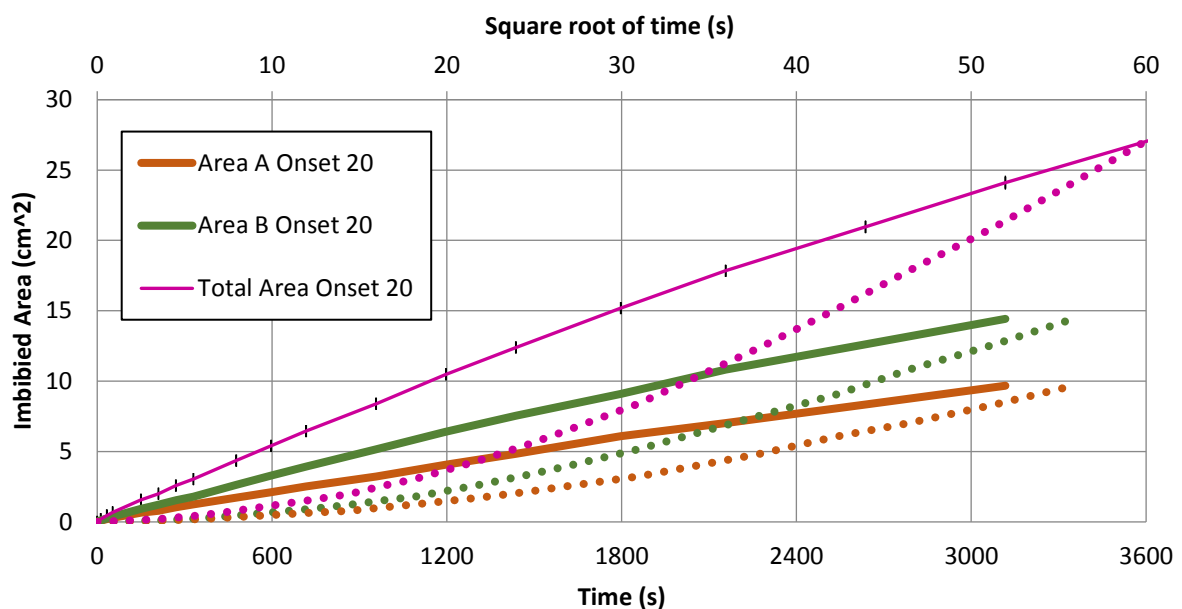


Figure 40: Limited open area spontaneous imbibition experiment Onset 20, with two open areas. The figure shows the combined and separate size of the two imbibed areas formed at the two limited open areas, versus time and the square root of time. The versus time curves are solid lines, and the versus square root of time curves are dotted lines. The absolute uncertainty of the total imbibed area is included. The vertical gridlines do not connect the two horizontal axes.

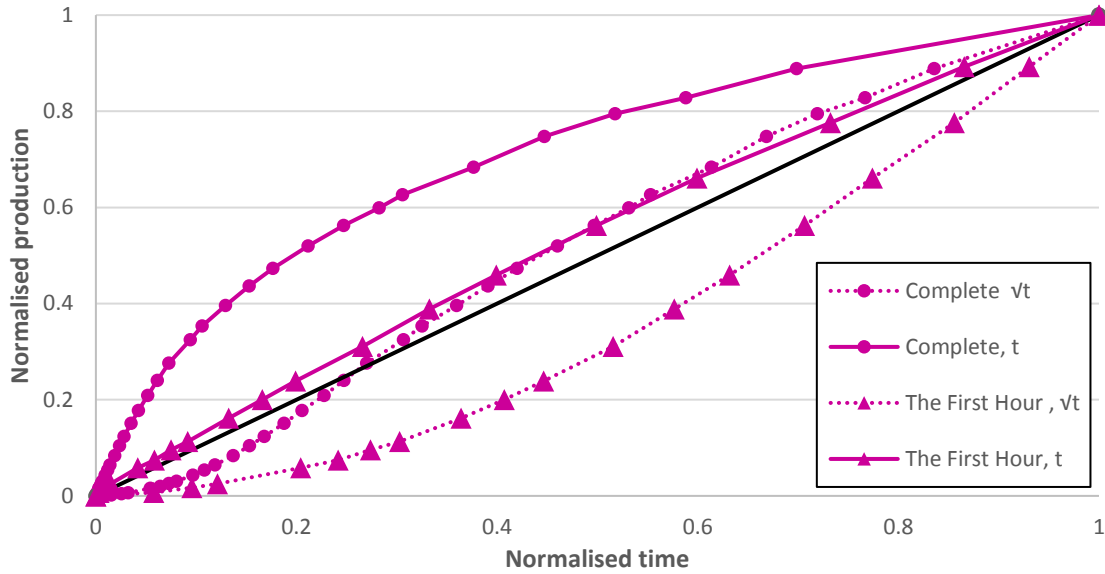


Figure 41: Limited open area spontaneous imbibition experiment Onset 20, with two open areas. The figure shows normalized imbibed area versus normalized time as solid lines, and versus normalized square root of time as dotted lines. The normalization is with respect to the time for delamination (round markers) and the first hour of the experiment (triangular markers).

Additional limited open areas influenced the imbibition process when more than two open areas were present, as in experiment Onset 21 and Onset 22 with respectively four and eight open areas. The increase of the imbibed area of Onset 21 was fitted to be proportional with time $t^{0.8}$ during the first hour, **Figure 60** in **Appendix III**. The increase of the imbibed area of Onset 22 was fitted to be proportional with time $t^{0.6}$ during the first hour, **Figure 63** in **Appendix III**. This shows a clear dependency between the number of limited open areas and the spontaneous imbibition rate during the initial period. The three experiments Onset 20, Onset 21 and Onset 22 experienced delamination at an intermediate time of the spontaneous imbibition process and the normalization of the imbibed areas versus normalized time is, therefore, performed with respect on the time for delamination. The time for delamination is included in **Table 6**.

18.2 CORRELATIONS BETWEEN THE TRANSFORMING SATURATION FRONT SHAPE AND THE IMBIBED AREA VERSUS TIME CURVE

No correlations between the transforming saturation front shape and the shape of imbibed area versus time curve are recognized in the work of this thesis. The time for when the saturation front is transforming from a radial to a segmented shape can be calculated if the transformation occurs when the imbibition rate is constant, i.e. for the first hour of the limited open area models. **Table 11** in **Append III** shows an overview of the observed time for transformation in the different two-dimensional paper models with one limited open area.

19 IN-SITU OBSERVATIONS OF LIMITED OPEN AREA INITIALIZATION

Spontaneous imbibition experiments applying *Positron Emission Tomography* (PET) for *in-situ* visualization of the advancing saturation front were performed on two Bentheim sandstone core plugs by professor Martin Fernø in the summer of 2012, **Table 8** includes the properties relevant for the experiments. This thesis presents a reanalysis of the spontaneous imbibition process with the emphasis on the onset period, as a highly deviating saturation front shape and imbibed volume versus time were observed in both samples. The images visualizing the change in water saturation during spontaneous imbibition process were reprocessed applying shorter time steps between the images during the initial period. The registered activity from the radioactively labeled brine measured by the PET detector, hereby denoted as the PET-signal, was quantified in two separate *Regions Of Interest* (ROI) in both samples. The ROI were two longitudinal surfaces placed perpendicular to each other, shown in **Figure 42**. The PET-signal in the two ROI were proportional to the water saturation calculated from the cumulative oil production; the measured PET-signals were therefore multiplied with a factor to represent the water saturation directly. The factors were calculated by dividing the final water saturation from the cumulative oil production by the PET-signal obtained when the spontaneous processes were completed. The water saturation from the PET signals and the water saturation calculated from the cumulative oil production during the spontaneous imbibition process are shown in **Figure 43 (a)**.

Table 8: Properties of the two sandstone samples used during spontaneous imbibition experiments visualized by PET.

Experiment	Length Diameter [cm]	Porosity Permeability [D]	Non wetting fluid Viscosity [cP]	Wetting fluid Viscosity [cP]	Pressure taps Location	Boundary condition
Sandstone 1	13.0	0.229	Decane	Brine	3	One End Open
	5.0	4.15	0.9	1.07	1 at dead end 2 at curved surface	
Sandstone 2	8.3	0.226	Marcol	Brine	1	Two Ends Open Free
	5.0	2.51	83.3	1.07	At curved surface	

The visualized saturation front during the spontaneous imbibition process in sample Sandstone 1 and Sandstone 2 should be categorized as a limited area initialization. Induction times were observed in both samples, respectively 150 minutes in sample Sandstone 1 and 50 minutes in sample Sandstone 2. The shape and behavior of the saturation fronts were similar between the two samples. A distinct pathway of the wetting fluid, approximately 1.5 cm deep, was established at the center of the wetted surface and the saturation front continue to advance as an elongated sphere from this pathway. The saturation front shape in sample Sandstone 1 at different time steps is shown in **Figure 42**; the red area indicates a high water saturation. . It appears that a piston-front is formed at the first 0.5 cm of the sample, close to the void space in the continuously flushing inlet. However, the same signal is detected from the POM-inlet, and is therefore likely an experimental artifact caused by higher resolution in the CT signal compared to the PET-signal: because of this, a PET-signal can appear in impermeable parts of the setup (like the POM-spacer) without radioactive fluid actually being present there.

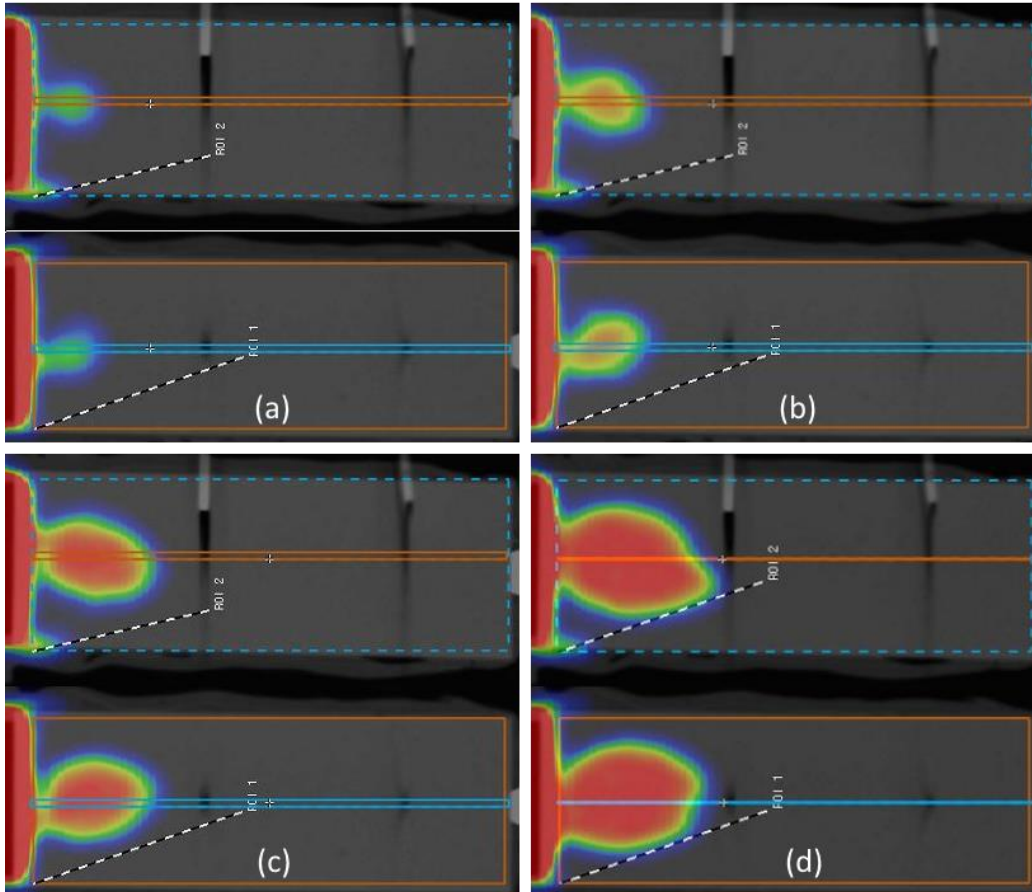


Figure 42: The saturation front at different times during spontaneous imbibition into sample Sandstone 1 visualized using a PET. The two regions of interest ROI 1 and ROI 2 are longitudinal and placed perpendicular to each other, outlined in orange and blue. The red area to the left on each image is the inlet. The two pressure taps are visible on the gray scaled CT background image. Image (a) is 180 minutes after the experiments was initiated, (b) 210 minutes, (c) 250 minutes and (d) 280 minutes.

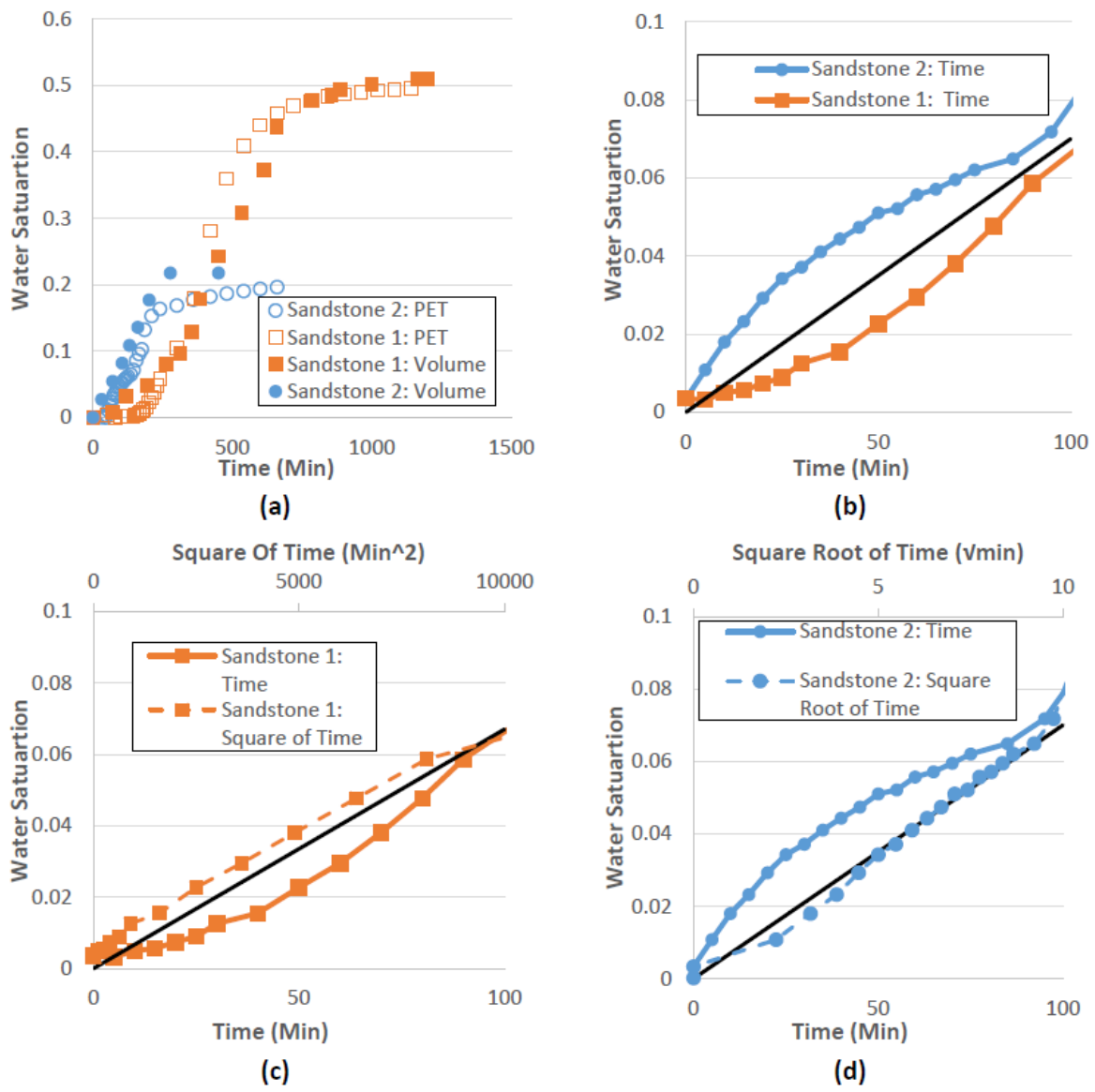


Figure 43: Increasing average water saturation versus time during spontaneous imbibition in sample Sandstone 1 and Sandstone 2. (a) The increase in average water saturation during the complete spontaneous imbibition process. Calculated from the cumulative oil production (Volume), and from PET signals (PET), the induction period is included. (b) The increase in average water saturation during the onset period after the induction period. (c) The increase in average water saturation during the onset period in sample Sandstone 1, compared with a diagonal reference line, the dotted line and the secondary x-axis represents the square of time. (d) The increase in average water saturation during the onset period in sample Sandstone 2, compared with a diagonal reference line, the dotted line and the secondary x-axis represents the square root of time.

The increase in saturation was proportional to the square of time during the onset period in sample Sandstone 1. The high-quality visualization obtained by the PET scanner gives indications of a possible explanation for the saturation front shape and the square of time increase in saturation: the flow is limited through a preferred pathway, clearly visible on the image (a) and (b) in Figure 42. This pathway is restricting the flow and is the significant contribution to viscous resistance, similar to the limited open area in the two-dimensional models previously presented. However, the size of this pathway is not fixed, it is clearly growing radially outward, image (c) and (d), and the viscous resistance decreases causing an increasing imbibition rate. The flow rate through a cylindrically shaped pathway at a constant pressure drop will be proportional to the cross sectional area; the cross-sectional area is

proportional to the radius squared; the imbibition rate will, therefore, increase cubically to the expanding radius of the pathway.

No direct observations of why limited pathways are established at the inlet side of the samples are obtained. However, the observation of an induction time has similarities with and could have the same proposed explanation, as the induction time and irregular spontaneous imbibition observed in experiments presented in **Chapter 16.2**. Where heterogeneous wettability was proposed to explain induction times during spontaneous imbibition experiments performed by Fernø et al. (2010), and the irregular production of oil from imbibition tube SP17_E2. The indication of heterogenic wettability can be supported by the PET images taken at the end of the spontaneous imbibition experiment, **Figure 44**. The distribution of brine after spontaneous imbibition is significantly affected by the closed side boundary and the pressure taps; the area near the closed side boundary is completely oil saturated at the end of the experiment, indicating a wettability condition where spontaneous imbibition will not occur, i.e. neutral or oil wet. A similar saturation distribution is recognizable around the pressure taps, sealed with epoxy resin. The saturation front can to some extent be described as segment shape. However it is not converging towards a planar shape, as predicted by equation (62). The equation is based on a radial expansion of the saturation front unaffected by the location of the closed boundaries until it reaches it, confirmed in from the observations in the two-dimensional models, discussed in **Chapter 17.2**. The imbibition towards the closed side boundary and the pressure taps is likely reduced due to the wettability condition in those areas, and the spontaneous imbibition is therefore affected by the closed before it reaches it.

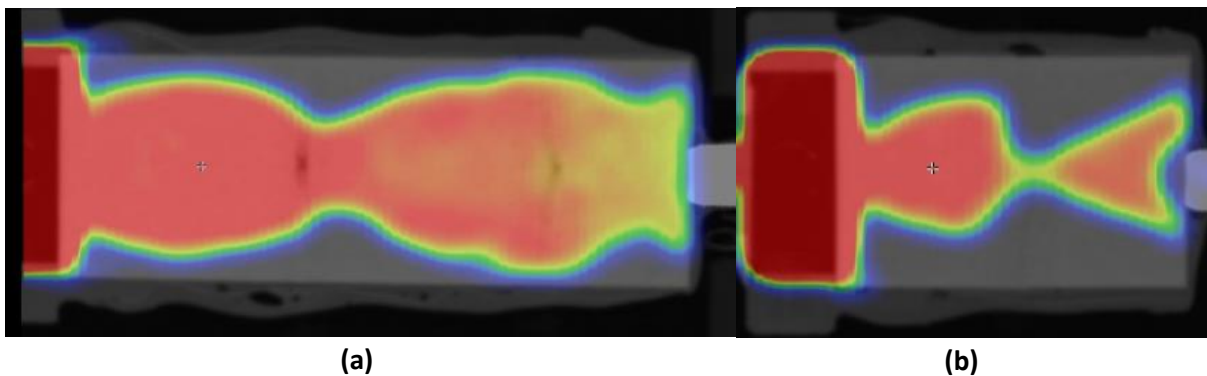


Figure 44: The final saturation distribution in sample Sandstone 1 (a) and Sandstone 2 (b).

The use of epoxy resin to seal the closed no-flow boundaries during spontaneous imbibition experiments has been shown to affect wettability (Morrow and Xie, 2001), and is a likely explanation for possible alteration in the wettability in the two sandstone cores. The observation of a possible heterogeneous wettability distribution across the samples has a severe effect on the behavior of the spontaneous imbibition: including the duration of the experiments, the induction time and the recovery of oil by spontaneous imbibition. The recovery of oil by spontaneous imbibition is a key parameter in the Amott-Harvey index, making wettability measurements from aged cores where an induction time has been observed questionable. The use of *in-situ* imaging as PET is, therefore, a very valuable tool when investigating spontaneous imbibition, as the experimental artifact of heterogeneous wettability is easily observed and identifiable. However, *in-situ* imaging is expensive and unavailable. Packed transparent glass imbibition tube represent a quick and affordable method to investigate: wettability and the effect of wettability altering chemicals on capillary pressure, relative

permeability, and spontaneous imbibition, where any such experimental artifacts are easily observed and identify, as in the imbibition tube experiment with a heterogeneous wettability, SP17_ E2. The next chapter presents a method to identify the cause and effect from an onset period when no visualization of the spontaneous imbibition process is obtained, by comparing the imbibition versus time curve with a set of analytical models based on the Darcy model.

The increase in saturation was proportional to the square root of time during the onset period in sample Sandstone 2, indicating that the viscous resistance is associated with the flow of the oil, having an increased viscosity compared with the oil used in Sandstone 1

20 IDENTIFYING DIFFERENT CAUSES FOR THE ONSET

The onset period effect on the production curve during spontaneous imbibition into natural porous material is notable in several literature spontaneous imbibition experiments. The onset period gives a variety of deviations from the assumed square root of time behavior during the initial period of the experiments. The imbibition versus time curve for the initial period of spontaneous imbibition experiments, i.e. spontaneous imbibition rate, could be compared and possibly matched with different analytical curves based on the Darcy model. The Darcy curves are based on a set of assumptions, which can give indications of the nature behind the onset phenomena. Especially if the assumptions have physically likely explanations, and are supported by visual observations through transparent models, or *in-situ* imaging. It can, therefore, be rewarding to compare the collected data sets for the initial period of spontaneous imbibition experiments, to analytical models. It is possible to obtain a variety of Darcy model curves by weighting assumptions, e.g. boundary condition, viscous resistance and the shape of the saturation front. The shape of the saturation front can be imitated by adding radial, spherical or expanding pathway model on to linear sample for a period of the spontaneous imbibition where deviating behavior is observed.

An overview of how different displacement trajectories of imbibing flow will affect the rate of spontaneous imbibition, based on the Darcy model, is presented in **Table 9**, and idealized normalized production versus time curves are visualized in **Figure 44**. If the imbibition is limited through a small opening, for instance during radial and spherical outward boundary case, the spontaneous imbibition rate will be linear with the square root of time during the initial period. In this case, the resistance of flow will be associated with the distance from the inlet to the front, and this distance is increasing. The imbibition rate will become linear with time when the saturation front has advanced sufficiently far away from the inlet. At this point, most of the viscous resistance will be located in the vicinity of the inlet (Mason et al., 2012; Xiao et al., 2012). As shown in **Figure 44**, the spherical case converges much fast towards a linear trend compared with the radial case. A special situation, where the saturation front is growing spherically outward from a pathway expanding linearly with time, the spontaneous imbibition rate will be proportional to the square of time. In this case, the viscous resistance is associated with the cross-sectional area of the pathway, as observed and discussed in **Chapter 19** for the spontaneous imbibition experiment applying PET visualization. The spontaneous imbibition rate will be proportional to the square root of time if the viscous resistance at some point becomes dominated by the distance between the inlet face and saturation front.

Table 9: Development of spontaneous imbibition rate for different displacement trajectories

Displacement trajectory	The rate of spontaneous imbibition is proportional with:
Linear	Initial period: $t^{0.5}$ Late period: t
Radial outward	Initial period: $t^{0.5}$ Late period t
Spherical outward	Initial period: t Late period: $t^{0.5}$
Expanding Pathway	Initial period: t^2 Late period: $t^{0.5}$

Two different cases of onset situations were investigated using the matching with analytical curves method in this thesis; both onsets were affected by a limited area available for the wetting fluid to flow through during the initial period of spontaneous imbibition. The nature of the limited open areas was drastically different between the two cases. The size of the limited open areas in the two dimensional models was fixed, causing a linear with time imbibition for the initial period of the spontaneous experiment, which had a noticeable effect on the imbibed volume versus square root of time curve visible as a slack below the diagonal reference line. The limited area in the sandstone experiments applying PET to visualize the saturation front can be described as an expanding pathway; the expanding pathway caused the imbibed volume to be proportional to the square of time. The PET experiments and the two-dimensional model experiments produced more data during the initial period compared to the litterateur, thus making it possible to clearly observe and analyze behavior deviating from conventional results. The onset period is most notable when the imbibed volume is presented versus time and versus square root of time. Most literature results are presented versus logarithmically time and the logarithmically dimensionless time and are therefore challenging to analyze. This include a variety of litterateur applications of spontaneous imbibition measurements where induction times has been observed.

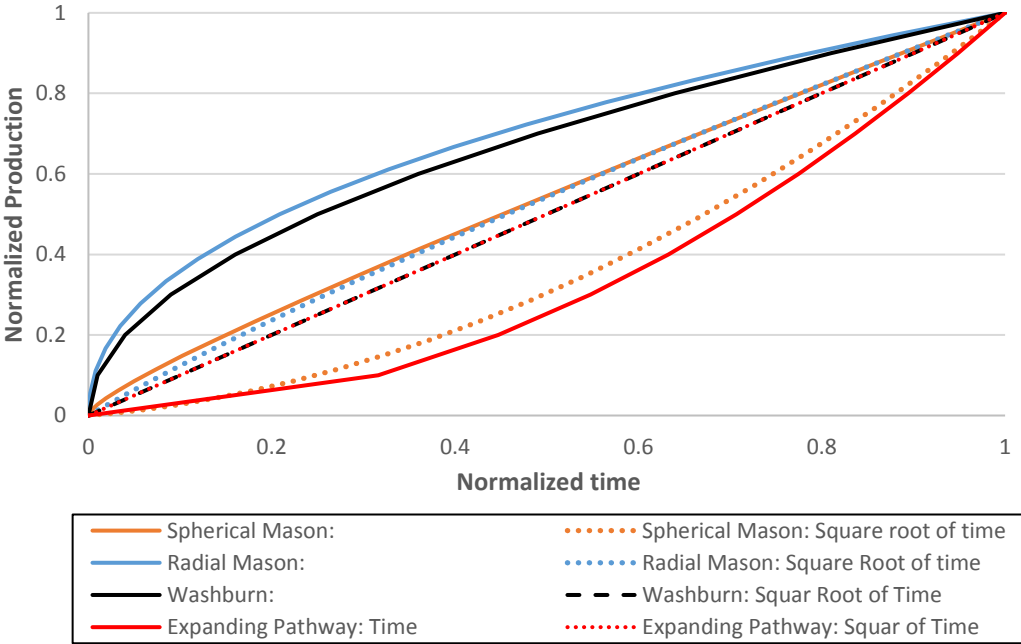


Figure 45: Shows the normalized production during an idealized linear, spherical outward, radial outward and the suggested expanding pathway spontaneous imbibition. The spherical and radial curves are calculated using the Darcy model derived by Mason et al. (2009b). The ratio $\frac{R_{closed}}{R_{open}} = 5$, for both curves. The Washburn equation is used to calculate the idealized linear curves. The expanding Pathway is based on the analysis in Chapter 19.

21 THE ONSET INFLUENCING SCALING OF SPONTANEOUS IMBIBITION

From the variation in rate and duration of spontaneous imbibition experiments presented in **Figure 24** with equal properties other than initial water saturation, it is clear that an ideal scaling group should incorporate the effect of the initial water saturation. Initial water saturation and distribution of the fluids is a required condition for the scaling groups by Ma et al. (1997), presented in **Chapter 6**, based on the well-known scaling group proposed by Mattax and KYTE (1962). This requirement of initial water saturation was only true between experiment SP10_E2 and SP11. In **Figure 24** it is easy to observe the similarity between the two experiments, and how greatly they differ from experiment SP10_E1 with lower initial water saturation and SP10_E1 with a higher initial water saturation. It is not necessary to scale the four experiments, due to equal sample and fluid properties used in the calculations of the scaling groups.

A universal scaling group capturing all key parameters of spontaneous imbibition was derived by Schmid and Geiger (2012). The scaling group is derived from an exact solution to the Darcy model, in comparisons with the derivations presented in **Chapter 4** by Mason et al. (2009b) and Mason et al. (2012), where a piston-like displacement is assumed. The universal scaling group relies on capillary and relative permeability curves, denoted as capillary-hydraulic properties. The universal scaling group gave remarkably good results when applied on 42 different core experiments. However, for early times the scaled results scattered around the curve given by the analytical solution. This scattering was proposed to be a result of the capillary-hydraulic properties used or the dataset itself. If the scattering is a result of the dataset itself and is predominantly occurring for the early time it should be addressed as a result of the onset period. Implying that the new universal scaling group incorporating capillary-hydraulic properties do not capture the onset period.

A scaling group for co-current linear spontaneous imbibition with a two ends open free spontaneous imbibition boundary case was proposed by Mirzaei-Paiaman et al. (2017). The co-current spontaneous imbibition scaling group was based on the universal scaling group proposed by Schmid and Geiger (2012) and is valid for both non-piston-like and piston-like displacements. A simplified scaling group for water-wet conditions with duplicated initial water saturation was presented, equation (63). This simplified scaling group was used to calculate spontaneous imbibition versus dimensionless time for the imbibition tube experiments with no initial water saturation. The scaled results are presented as change in water saturation versus dimensionless time and are compared with pre-scaled results in **Figure 46**. The scaling group gave a satisfactory match between the experiments. However, a separation into two separate groups of well-matched experiments is evident. The left group contains the experiments with short imbibition tubes (16 cm) and the experiments with an increased non-wetting phase viscosity. The other group contains the experiments with long imbibition tubes and decane as the non-wetting phase. No measurements of the interfacial tension were performed in the experimental work in this thesis, the value $\sigma = 52 \text{ dyn/cm}$ were used for all fluids in the calculations of the dimensionless time, based on a literature water-decane interfacial tension measured by Zeppieri et al. (2001).

$$t_{d,simplified} = \sqrt{\frac{\left(2\sigma * \sqrt{\frac{K}{\phi}}\right)}{\left(\mu_{nw} + \sqrt{\mu_w \mu_{nw}}\right)L^2}} t^{\frac{1}{2}} \quad (63)$$

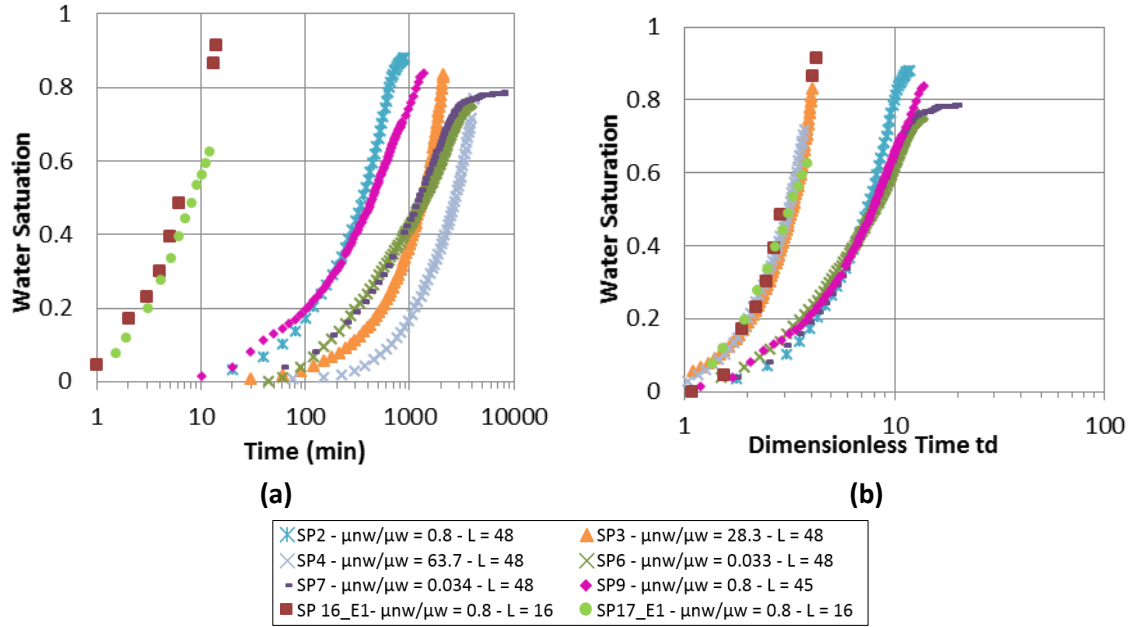


Figure 46: Co-current spontaneous imbibition from zero initial water, the samples had varying length and viscosity, marked on the label. (a) Change in water saturation versus time (logarithmic x-axis). (b) Change in water saturation versus dimensionless time, calculated using the co-current scaling group proposed by Mirzaei-Paiaman et al. (2017).

21.1 THE EFFECT FROM THE ONSET PERIOD IN THE TWO DIMENSIONAL MODELS

The imbibed areas versus time during spontaneous imbibition experiments applying two-dimensional paperboard models were scaled and the dimensionless times were compared between the experiments. A characteristic length incorporating the onset period due to the special boundary case on the limited open area models has not been derived. It was, therefore, interesting to test if any of the conventional characteristic lengths of different boundary cases would result in a satisfactory match when applied on the limited open area models. The scaled results from the limited open area models were compared with scaled results from two-dimensional models applying one end open and radial outward boundary case, as a reference.

The permeability, porosity, and viscosities are assumed equal between the two dimensional-models, and time is therefore only scaled using the characteristic length i.e.

$$t_d = \frac{1}{L_c^2} * t \quad (64)$$

, where the characteristic length is calculated from the samples size and boundary case. Most of the experiments were at some point strongly affected by delamination, and therefore is only the spontaneous imbibition results until delamination occurred included. Both the fractional imbibed area and the characteristic length were calculated with respect to the position of the saturation front when delamination occurred. The length used in the calculations of the characteristic length is therefore not necessarily equal to the true length of the samples for some of the models, an overview of the length used in the calculations and the time for delamination is included in **Table 11** in **Appendix III**. The radial and spherical outward characteristic lengths were calculated using an outer radius R_{closed} equal to half the width of the models, and the inner open radius R_{open} equal to a radius of a circle with a circumference equal to the width of the limited open area, i.e. $R_{open} = 0.08 \text{ cm}$.

Four different characteristic lengths based on different boundary cases were tested on the limited open area models. **Figure 47** compares the dimensionless time for some of the limited open area experiments when scaled using an OEO characteristic length. The OEO characteristic length results in acceptable scaled results, keeping the spreading in dimensionless time close to a factor of 5, usually regarded as satisfactory correlation (Mason and Morrow, 2013). However, it is evident that the samples with the shortest lengths, sample Onset 15 and Onset 11, is affected by the initial period of the spontaneous imbibition process where the increase in imbibed area is restricted by the limited open area, causing a linear with time increase in the imbibed area. The two experiments matched applying the radial or spherical characteristic lengths, **Figure 48** and **Figure 49**. The period of a linear increase in the imbibed area is relatively shorter for the longer samples, and the affect from this period on the dimensionless time is therefore to some degree suppressed, causing them to have a better match with the Linear One End Open samples towards the end of the spontaneous imbibition process. It is noticeable that the scaled results for the limited open area models are divergent from the Linear and Radial samples during the initial period, likely due to the onset period. This divergence in the initial period is less prominent when a spherical characteristic length is applied, indicating a better match for a spherical boundary case in the initial period, where the limited open area is restricting the spontaneous imbibition. However, the spherical boundary case results in a considerable spreading in the dimensionless time at the end of the spontaneous imbibition process.

The last characteristic length was calculated from the shape factor, equation 54 , giving:

$$L_c = \sqrt{\frac{L * W * b}{\sum_{i=1}^n \frac{b * W_{open}}{L}}} \quad (65)$$

, where h is the thickness of the models and W_{open} is the width of the limited open area and n is the number of open areas. Simplifies for n limited open areas:

$$L_c = \sqrt{\frac{L^2 * W}{n * W_{open}}} \quad (66)$$

This characteristic length using equation (66) resulted in the greatest spreading of all four tested characteristic lengths.

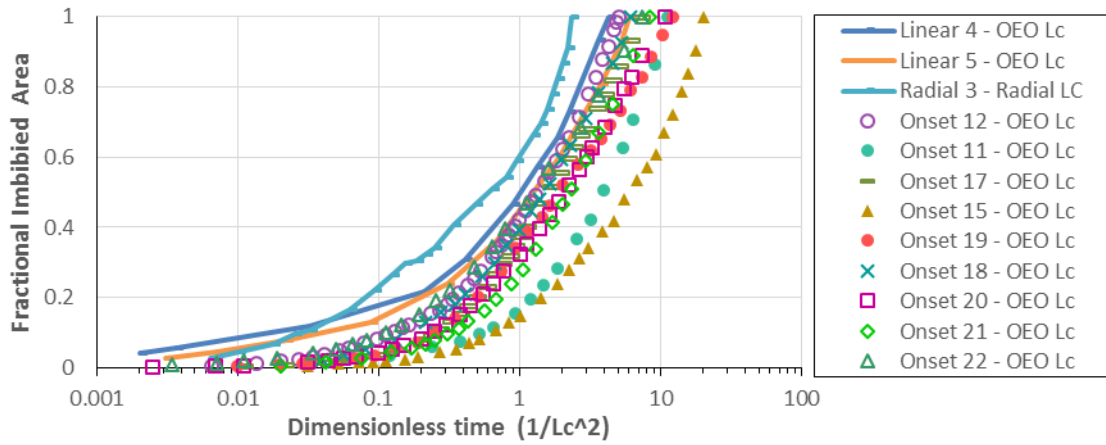


Figure 47: Fractional imbibed area versus dimensionless time. The dimensionless time for the samples with a limited open area (Onset) is calculated using an OEO characteristic length, Table 1. The dimensionless time for the samples with an OEO and radial outward boundary case is calculated with their respective characteristic lengths.

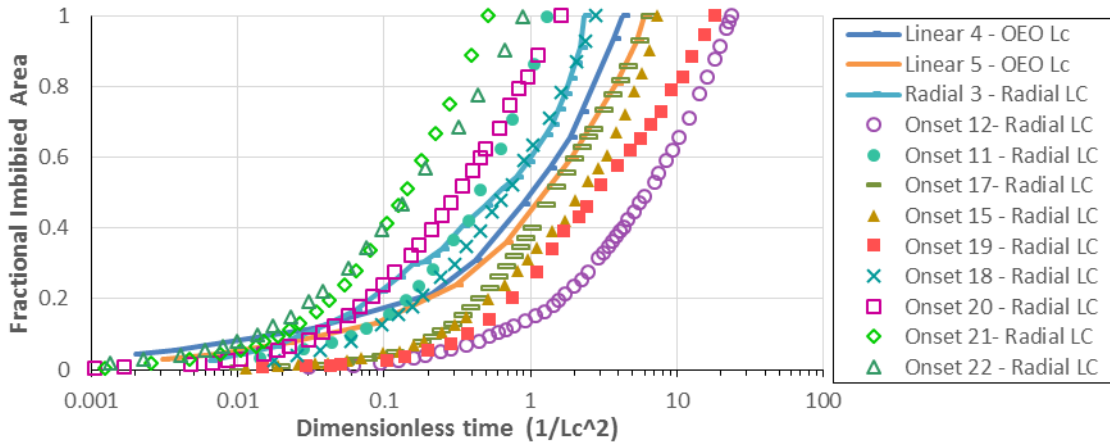


Figure 48: Fractional imbibed area versus dimensionless time. The dimensionless time for the samples with a limited open area (Onset) is calculated using a Radial outward characteristic length, Table 1. The dimensionless time for the samples with an OEO and radial outward boundary case is calculated with their respective characteristic lengths.

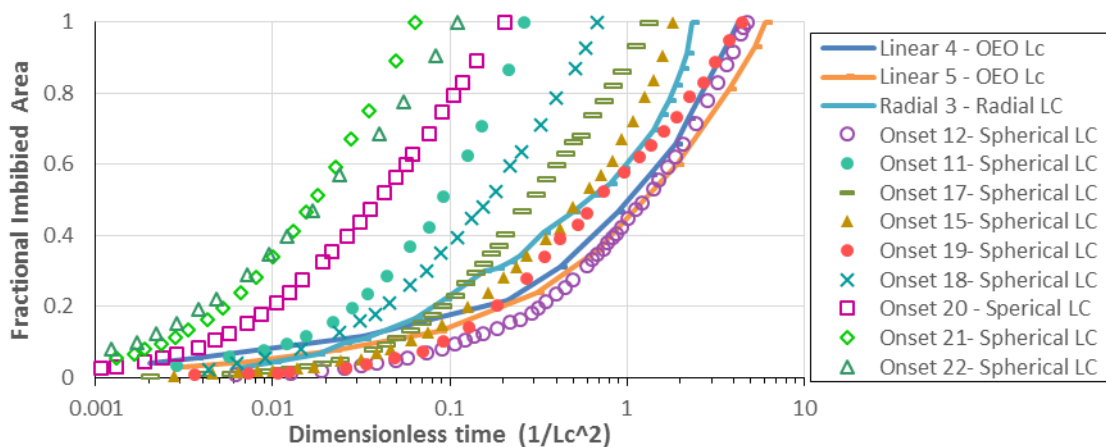


Figure 49: Fractional imbibed area versus dimensionless time. The dimensionless time for the samples with a limited open area (Onset) is calculated using a Spherical outward characteristic length, Table 1. The dimensionless time for the samples with an OEO and radial outward boundary case is calculated with their respective characteristic lengths.

21.2 INDUCTION TIMES

Induction times during spontaneous imbibition experiments are significantly affecting the duration of the experiments and therefore also the dimensionless time. The induction times can be removed from the datasets. However, this can be problematic. As scaling is commonly performed on aged cores, or on cores with closed surface using epoxy resin where the induction time indicates a heterogeneous wettability distribution, a severe experimental artifact when the experiments are assuming a homogeneous wettability.

PART IV. CONCLUSION AND FUTURE WORK

22 CONCLUSIONS

The onset of spontaneous imbibition was investigated using experimental setups where the saturation front shape and profile in porous media were directly visualized: unconsolidated sand packed in transparent imbibition tubes, two-dimensional paperboard models and sandstone core plugs applying PET-CT imaging. The main objective was to investigate the onset period, where deviating saturation fronts and production of the non-wetting phase has been reported. Secondary objectives were to analyze how the phenomenon affects applications of spontaneous imbibition measurements, as scaling, capillary pressure, and wettability.

The term “limited area initialization” was used to describe the onset of spontaneous imbibition from on or a few points on the surface exposed to the wetting fluid. The scaling of spontaneous during a limited area initialization depends on the development of the viscous resistance. The use of two-dimensional paper models allowed for controlled experiments related to this phenomena, where limited initialization areas were kept constant and the number of such sites were varied systematically. Hemispherical outwards displacement fronts were observed from each open area, scaling linearly with time. In a three-dimensional system the initialization area was not constant, measured with PET, and increased with time. Hence, the viscous resistance decreased with time, and the imbibition rate scaled linearly with the square of time.

Heterogenic layered distribution of wettability observed in sand packs with dyed non-wetting phase and in the epoxy-coated core plug was an experimental artifact due presence of wettability-alteration chemicals. Great care should be taken to avoid or correctly compensate for such effects. The presence of a non-uniform wettability, however, allowed an in-depth analysis of its effect in this work. The non-uniform wettability distribution resulted in

- induction periods and limited area initialization with deviated saturation fronts
- the segment shaped saturation front did not converge to a planer shaped front as predicted by the model presented in **Chapter 17.2**.

An improved imbibition tube setup the with possibility to measure counter-current production, performing forced flow experiments, and with a high accuracy regarding the inlet pressure has been developed, with the following key results

- non-zero initial water saturation resulted in self-similar saturation profiles
- The viscosity ratio was varied over 4 order of magnitude and did not affect the onset.
- No correlation between front capillary pressure and the onset of spontaneous imbibition has been found. The onset period was observed at a distinct initial water saturation.

23 FUTURE WORK

The work in this thesis is built on experiences obtained by Vabø (2016) and Haugland (2016) applying imbibition tubes, and unpublished experimental results from Prof. Martin Fernø in capillary driven flow. The imbibition tube experimental setup gives consistent spontaneous imbibition results and incorporates the possibilities to measure permeability, drainage, and forced imbibition. Imbibition tubes are considered to be a valuable method to investigate the effects from wettability altering chemicals on capillary pressure, relative permeability and spontaneous imbibition in future research. The use of the dyed fluid, especially in the non-wetting phase, is very beneficial when observing the saturation change in the imbibition tubes. However, great caution regarding the chemical properties of the dye should be taken, as the sand pack showed high sensitivity from wettability alterations, and series of experiments including contact angle wettability measurements should be performed to find suitable dyes.

The complete physics behind the observed onset phenomenon caused by the heterogeneous wettability distribution is still not known, the observations in this thesis are limited to the effect from a local increase in saturation, causing a pathway for the wetting fluid. The dynamics of the wettability and the capillary pressure should be investigated, as it is unknown how the pathways are formed.

The observation of induction time caused by a heterogeneous wettability is of great concern regarding the measurements of wettability applying the Amoth-Harvey index and should be further investigated. Spontaneous imbibition experiments on aged cores applying PET for visualization should be performed. The effect from heterogeneous wettability can also be tested in imbibition tubes, by packing pre aged sand of different wettability in layers.

PART V. APPENDICES AND BIBLIOGRAPHY

APPENDIX I. UNCERTAINTY ESTIMATION.

The uncertainty in experimental measurements are caused by two sources: The uncertainty related to the observer and the experiments itself, e.g. the method used to estimate the imbibed areas two-dimensional models and the uncertainty of the instruments used, e.g. the step volume in the pump causing small oscillations.

The uncertainty in the imbibed area in two-dimensional models was estimated from the accuracy of determining the position of the saturation front, clarified in **Chapter 12.2**.

The arithmetical mean of the measured pressures during permeability measurements were used in the permeability calculations. The uncertainty in the permeability measurements was calculated as the standard derivations of the oscillations in the pressure due to the step volume in the pump, using equation (69). This was the significant contribution to the uncertainty.

The instrumental uncertainties of the calculated density of the fluids, volume of imbibition tubes, pore volume, porosity, and saturations are calculated sequentially from length, mass, and volumetric measurements. Using equation (67) where multiplication and division of independent variables contributed to the uncertainty, and equation (68) where addition and subtraction contributed. The instrumental uncertainties are found in **Table 10**.

If a value R is calculated using addition or subtraction of a set variables x, y, z, \dots, i , where each variable has an inherent uncertainty $S_x, S_y, S_z, \dots, S_i$, then the uncertainty S_R for the variable R can be calculated by:

$$S_R = \sqrt{\left(\frac{\delta R}{\delta x} S_x\right)^2 + \left(\frac{\delta R}{\delta y} S_y\right)^2 + \left(\frac{\delta R}{\delta z} S_z\right)^2 + \dots + \left(\frac{\delta R}{\delta i} S_i\right)^2} \quad (67)$$

If a value R is calculated as the product or quotient of a set variables $a^2x, b^2y, c^2z, \dots, n^2i$, where x, y, z, \dots, i variables and $a^2, b^2, c^2, \dots, n^2$ are constants and each variable has an inherent uncertainty $S_x, S_y, S_z, \dots, S_i$, then the uncertainty S_R for the variable R can be calculated by:

$$\frac{S_R}{R} = \sqrt{\left(a \frac{S_x}{x}\right)^2 + \left(b \frac{S_y}{y}\right)^2 + \left(c \frac{S_z}{z}\right)^2 + \dots + \left(n \frac{S_i}{i}\right)^2} \quad (68)$$

The standard deviation S is the square root of the sample variance,

$$S = \sqrt{\frac{1}{N-1} \sum_{i=1}^N (x_i - \bar{x})^2} \quad (69)$$

, containing N number of samples values x , \bar{x} is the sample mean.

Table 10: Instrumental uncertainties used in this thesis

Instrument	Parameter	Uncertainty
Weight [gram]	Mass	±0.01
Caliper [cm]	Length	±0.02
Ruler [cm]	Length	±0.1
Graded imbibition tube 35 ml	Volume	±0.05
Graded cylinder 1000 ml	Volume	±10.0
Pressure transduced [bar]	Pressure	± 0.004
Pump [ml/h]	Volumetric flow rate	± 1 ml/h, *

**Contribution from oscillations in pressure was observed to be significantly larger*

APPENDIX II - NOMENCLATURE AND ABBREVIATIONS

Abbreviations	Description
IMBT	Imbibition tube
SI	Spontaneous imbibition
SP	Sand pack
PET	Positron emission tomography
CT	Computer tomography
MRI	Magnetic resonance imaging
OEO	One End Open boundary condition
TEO	Two Ends Open boundary condition
TEOFSI	Two Ends Open Free Spontaneous imbibition boundary condition
WP	Wetting phase
NWP	Non-wetting phase

Nomenclature	Description
A	Cross-sectional area of porous medium
A_f	Area of a linear saturation front
A_r	Area of a radial saturation front
A_s	Area of a spherical saturation front
A_i	Area of an open surface in direction i
C_{spread}	Leverett (1941) pore size distribution
D_f	The distance the saturation front has advanced along the closed side boundary
d	Diameter of a cylindrical sample
$\frac{\partial P_c}{\partial r}$	Pressure gradient during radial and spherical spontaneous imbibition
$\frac{\partial P_c}{\partial x}$	Pressure gradient during linear spontaneous imbibition
$\frac{\partial P_o}{\partial x}$	Non-wetting phase pressure gradient
$\frac{\partial P_w}{\partial x}$	Wetting phase pressure gradient
$\frac{dx}{dt}$	Rate of a linear advancing saturation front
$\frac{dr}{dt}$	Rate of a radial and spherical advancing saturation front
f	Fractional production
K	Absolut Permeability
$k_{r,nw}$	Relative permeability of non-wetting phase
$k_{f,w}$	Effective permeability of wetting phase
$k_{r,nw}$	Relative permeability of non-wetting phase
$k_{r,w}$	Relative permeability of wetting phase
L	Length of a porous medium
l_{A_i}	The actual distance the imbibition front travels from the open surface to the no-flow boundary
L_s	Characteristic length
L_c	Modified characteristic length
P_c	Capillary pressure
$P_{c,f}$	Front capillary pressure
$P_{c,o}$	Capillary back pressure
p_{nw}	Pressure in non-wetting phase
p_w	Pressure in wetting phase
$p_{nw,f}$	Pressure in non-wetting phase at the saturation front
$p_{w,f}$	Pressure in wetting phase at the saturation front
Δp_{nw}	Pressure drop in non-wetting phase

Δp_w	Pressure drop in wetting phase
P_{inlet}	Pressure in inlet
ΔP_H	Pressure contribution due to a height difference
ΔP_R	Pressure contribution due to a viscous resistance
Q	Cumulative production wetting phase
Q_{co}	Cumulative co-current production wetting phase
Q_{cc}	Cumulative counter-current production wetting phase
Q_{cc}/Q	Ratio produced counter-currently to total production
q	Flow rate
q_{nw}	Flow rate of non-wetting phase
q_w	Flow rate of wetting phase
S	Length of circle segment
S_w	Water saturation
$S_{w,i}$	The initial low water saturation before the spontaneous imbibition process
$S_{w,f}$	The water saturation ahead of the saturation front
$S_{w,sp}$	The water saturation after spontaneous imbibition
S_{A_i}	Distance from surface A_i to the center of the sample
t	Time
t_{end}	Time for when spontaneous imbibition ceases
t_f	Normalized time
t_d	Dimensionless time
V_b	The bulk volume of a sample
V_{osp}	The volume of oil produced during spontaneous imbibition
V_{ot}	The total volume of oil produced
V_{wt}	The total volume of water produced
V_{wsp}	The volume of water produced during spontaneous imbibition
W	Width of a porous medium
x	Length to the front position during a linear displacement
x_f	Normalized front position
x_{tube}	Length of a imbibition tube
α	The angle inscribed between the limited open area and the ends of the segment shaped front and the
δ_o	Amott oil Indice
δ_w	Amott water Indice
ϕ	Porosity
μ	Viscosity
μ_{gm}	Geometrical mean viscosity
μ_{nw}	Non-wetting phase viscosity
μ_w	Wetting phase viscosity
θ	Contact angle
ρ	Density
σ	Interfacial tension
ppm	Parts per million
wt. %	Weight percent

APPENDIX III ADDITIONAL RESULTS

Table 11: An overview of different times for transformation for the limited open area experiments. The size of the samples and time for when the spontaneous imbibition was completed and the time and how far the saturation front had advanced (delamination length) when delamination occurred is also included. The time for transformation is excluded for the samples with multiple limped open areas. However, the time for merging areas are included for those samples.

Experiment	Size parameters [cm] \pm 0.1	Delamination time (Hour: Minute) Delamination length [cm] *	Completed time (Hour: Minute)	Radial - Segment time (Hour: Minute)	Segment - Planar time (Hour: Minute)
One limited open area					
Onset 1	$L = 9.1$ $W = 3.9$	03:42 $L_{DL} = 4.1$	07:37	00:20	02:07
Onset 2	$L = 8.9$ $W = 3.9$		5:43	00:14	01:01
Onset 3	$L = 17.4$ $W = 4.2$	01:36 $L_{DL} = 4.5$	28:55	00:18	00:59
Onset 11	$L = 8.5$ $W = 8.5$	02:44 2.7	12:40	04:11	12:40
Onset 12	$L = 8.5$ $W = 17.0$		49:13	03:16	12:35
Onset 15	$L = 6.5$ $W = 6.5$	08:20 $L_{DL} = 3.5$	14:80	02:17	14:80
Onset 17	$L = 8.5$ $W = 25.5$	13:30 $L_{DL} = 7.5$	73:30	03:48	14:30
Onset 18	$L = 6.5$ $W = 13.0$	03:07 $L_{DL} = 3.9$	15:14	01:10	07:50
Onset 19	$L = 6.5$ $W = 19.5$	20:24 $L_{DL} = 7.1$	37:44	01:35	14:25
	Size parameters (cm)	Delamination time (Hour: Minute) Delamination length (cm)	Completed time (Hour: Minute)	Merging areas time (Hour: Minute)	
Multiple numbers of open areas					
Onset 20	$L = 20$ $W = 16$	14:17 $L_{DL} = 6.4$	35:50	00:52	
Onset 21	$L = 20$ $W = 16$	04:30 $L_{DL} = 4.0$	26:30	00:35	
Onset 22	$L = 20$ $W = 16$	07:47 $L_{DL} = 5.6$	27:00	00:08	

*The time for delamination affects the time for transformation if it occurs before it. Delamination length L_{DL} is calculated from the area imbibed at the time t_{DL} divided on the width W of the sample, and is, therefore, assuming a planer-shaped saturation front.

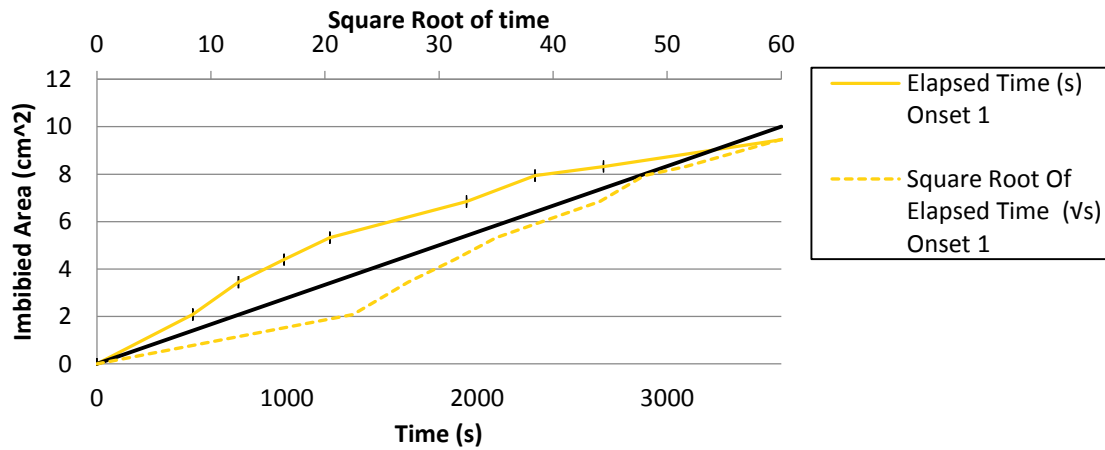


Figure 50: Limited open area spontaneous imbibition experiment Onset 1. The figure shows imbibed area versus time as solid lines, and versus square root of time as dotted lines, for the first hour of the spontaneous imbibition process. The uncertainty of the imbibed area is included.

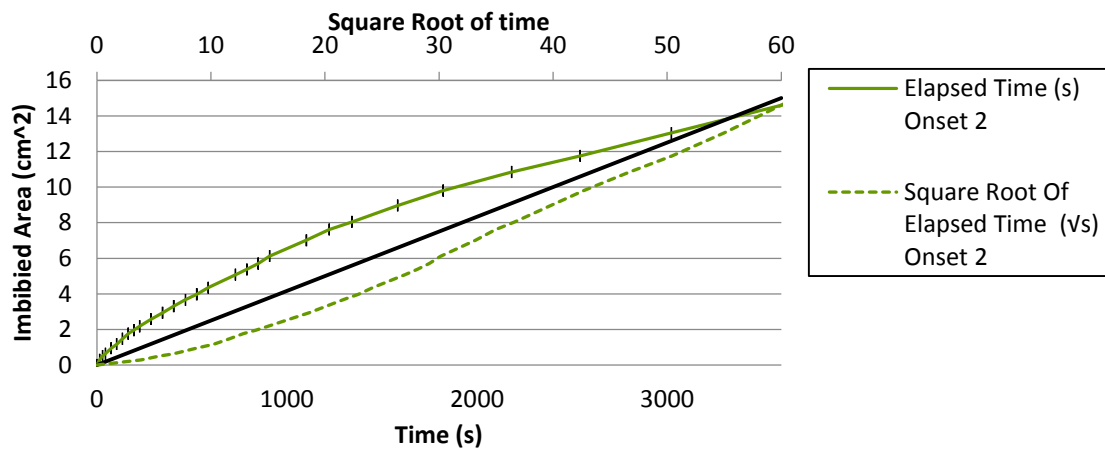


Figure 51: Limited open area spontaneous imbibition experiment Onset 2. The figure shows imbibed area versus time as solid lines, and versus square root of time as dotted lines, for the first hour of the spontaneous imbibition process. The uncertainty of the imbibed area is included.

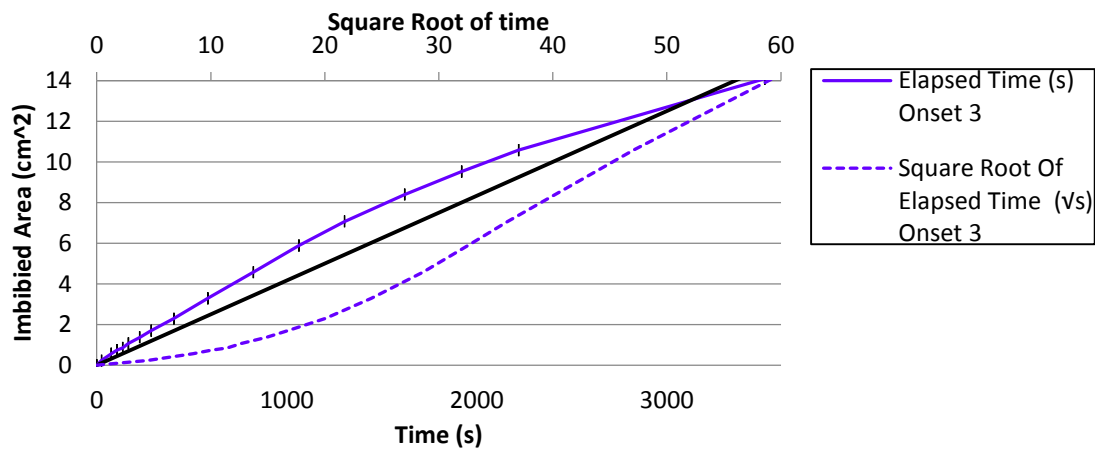


Figure 52: Limited open area spontaneous imbibition experiment Onset 3. The figure shows imbibed area versus time as solid lines, and versus square root of time as dotted lines, for the first hour of the spontaneous imbibition process. The uncertainty of the imbibed area is included.

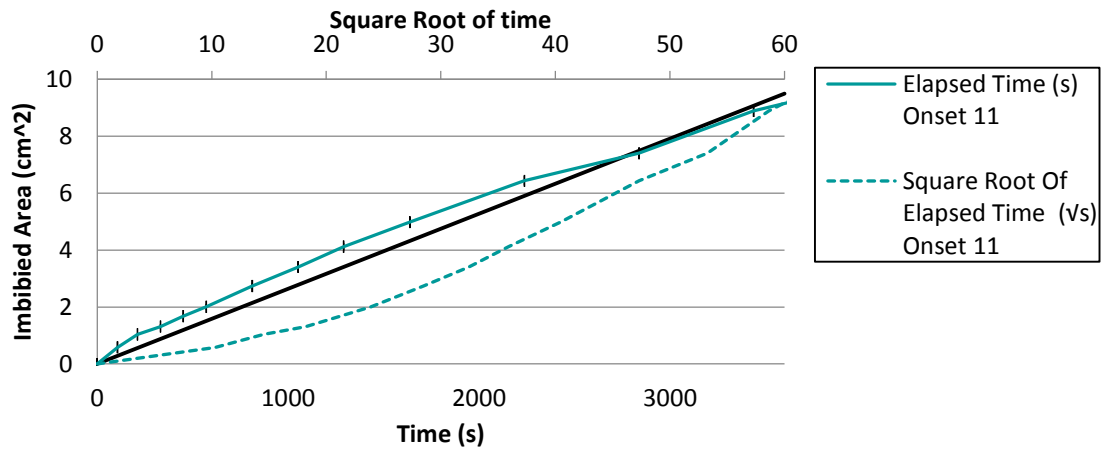


Figure 53: Limited open area spontaneous imbibition experiment Onset 11. The figure shows imbibed area versus time as solid lines, and versus square root of time as dotted lines, for the first hour of the spontaneous imbibition process. The uncertainty of the imbibed area is included.

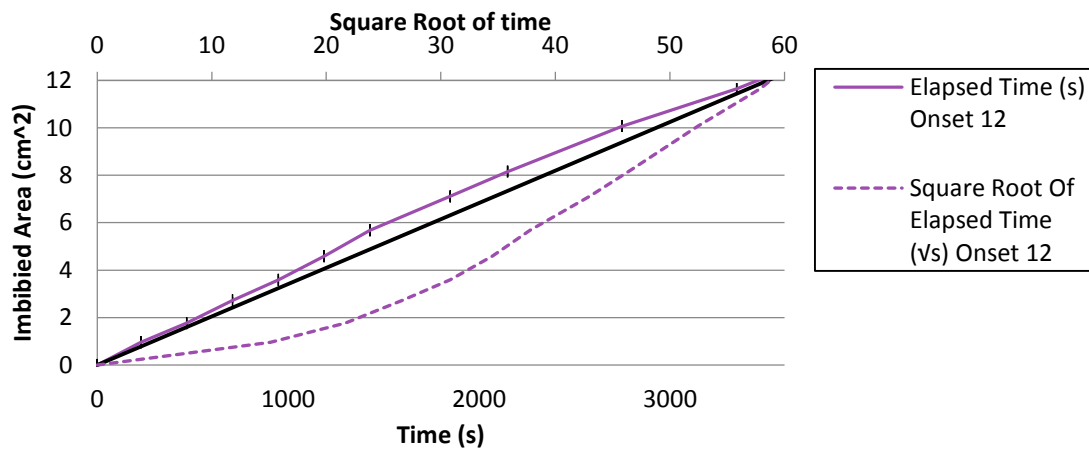


Figure 54: Limited open area spontaneous imbibition experiment Onset 12. The figure shows imbibed area versus time as solid lines, and versus square root of time as dotted lines, for the first hour of the spontaneous imbibition process. The uncertainty of the imbibed area is included.

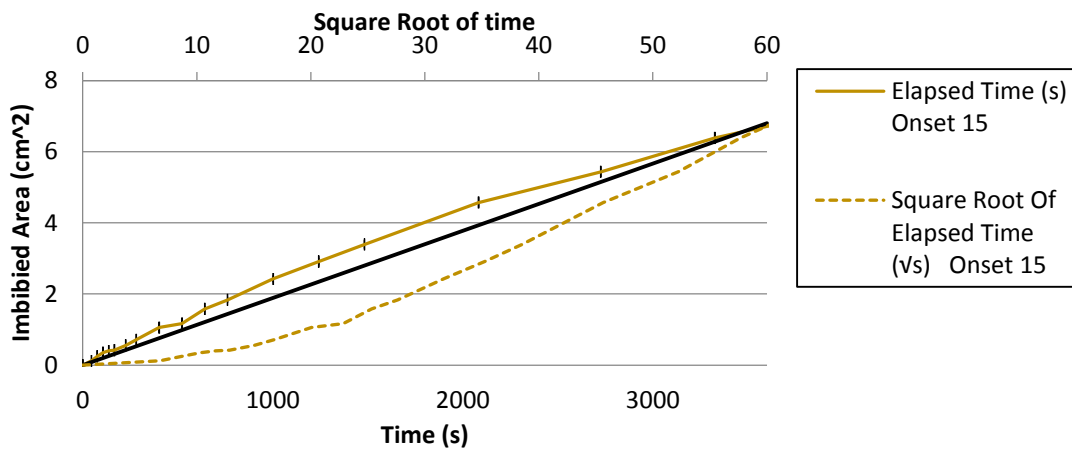


Figure 55: Limited open area spontaneous imbibition experiment Onset 15. The figure shows imbibed area versus time as solid lines, and versus square root of time as dotted lines, for the first hour of the spontaneous imbibition process. The uncertainty of the imbibed area is included.

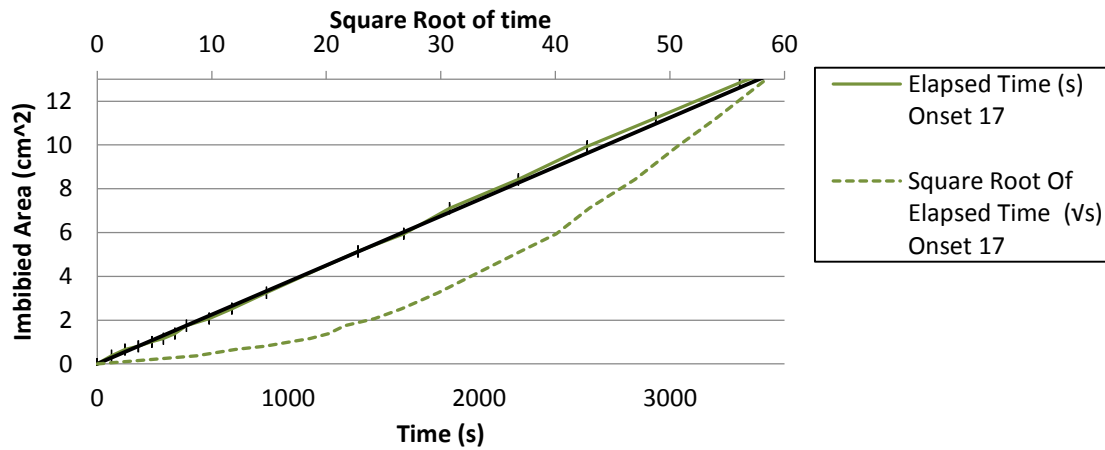


Figure 56: Limited open area spontaneous imbibition experiment Onset 17. The figure shows imbibed area versus time as solid lines, and versus square root of time as dotted lines, for the first hour of the spontaneous imbibition process. The uncertainty of the imbibed area is included.

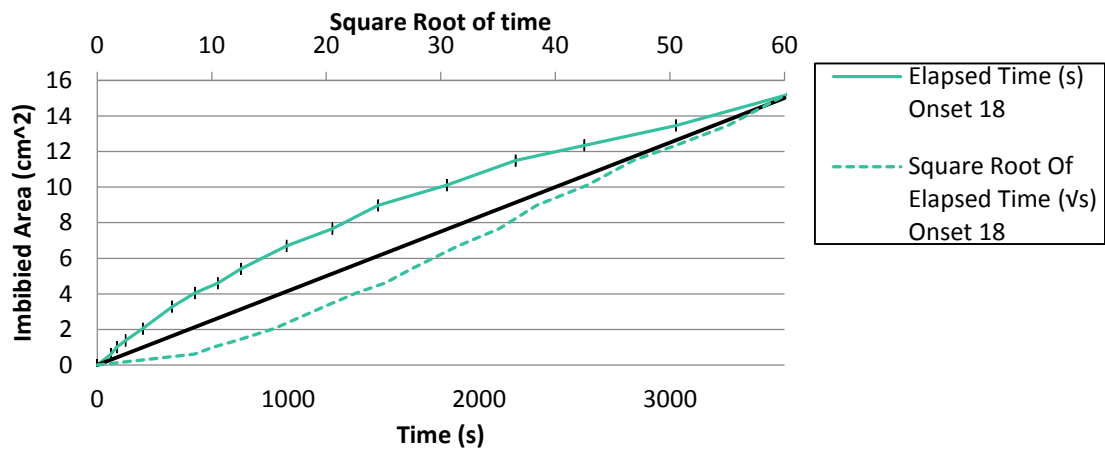


Figure 57: Limited open area spontaneous imbibition experiment Onset 18. The figure shows imbibed area versus time as solid lines, and versus square root of time as dotted lines, for the first hour of the spontaneous imbibition process. The uncertainty of the imbibed area is included.

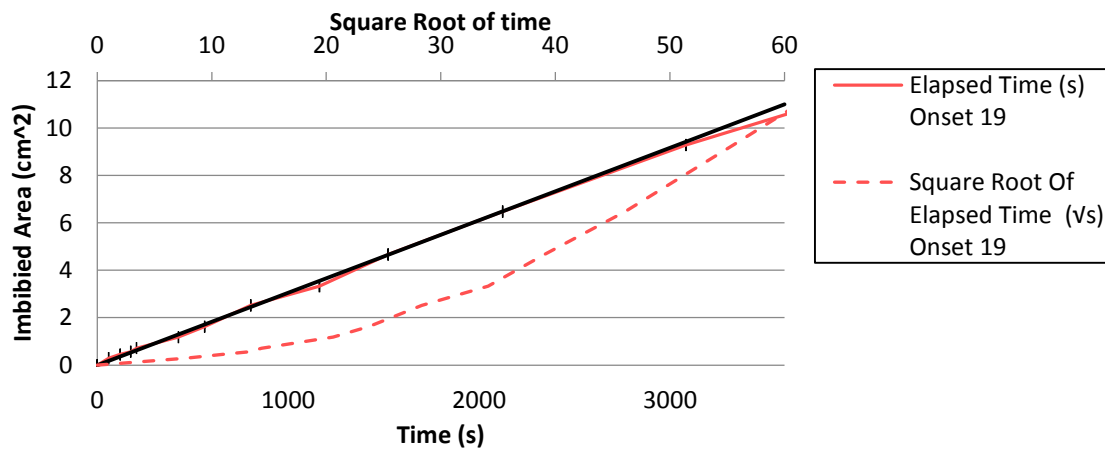


Figure 58: Limited open area spontaneous imbibition experiment Onset 19. The figure shows imbibed area versus time as solid lines, and versus square root of time as dotted lines, for the first hour of the spontaneous imbibition process. The uncertainty of the imbibed area is included.

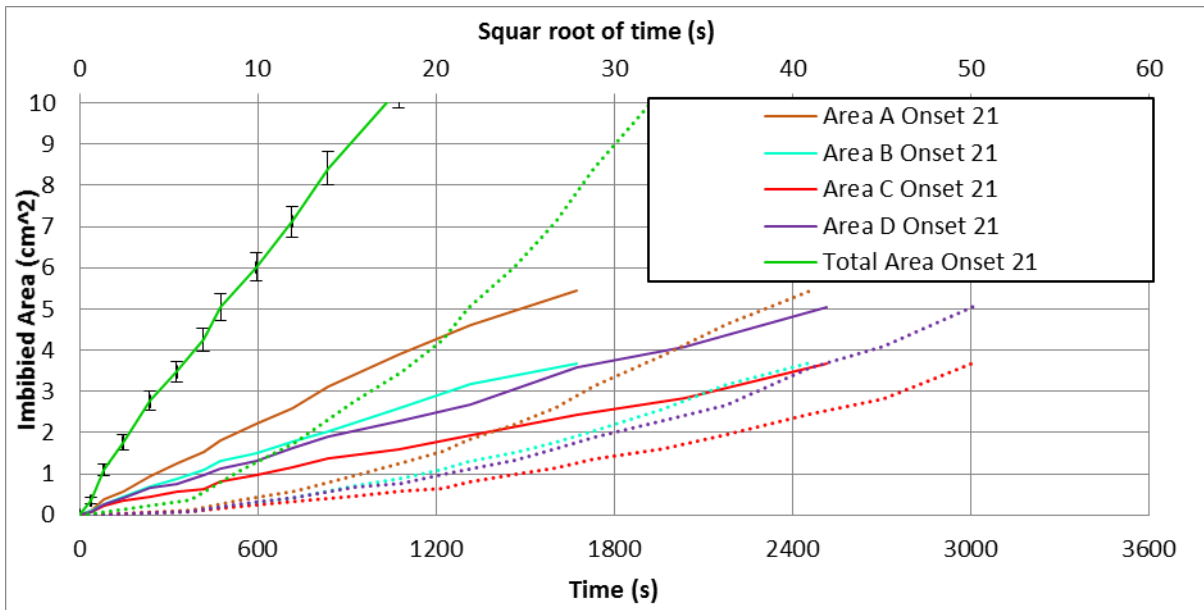


Figure 59: Limited open area spontaneous imbibition experiment Onset 21, with four open areas. The figure shows the combined and separate size of the four imbibed areas formed at the four limited open areas, versus time and the square root of time. The versus time curves are solid lines, and the versus square root of time curves are dotted lines. The vertical gridlines do not connect the two horizontal axes. The vertical axis is adjusted to present the individual areas. The absolute uncertainty in the total area is included.

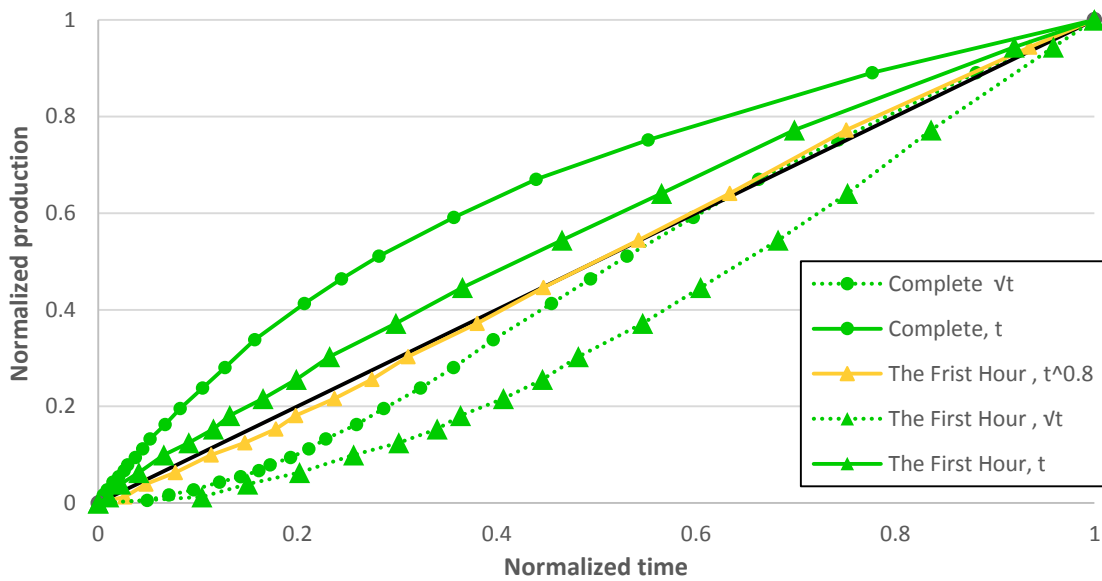


Figure 60: Limited open area spontaneous imbibition experiment Onset 21, with four open areas. The figure shows normalized imbibed area versus normalized time as solid lines, and versus normalized square root of time as dotted lines. The normalization is with respect to the time for delamination (round markers) and for the first hour of the experiment (triangular markers). The yellow line is a fitted curve showing that the imbibed area is linear with the time $t^{0.8}$, for the first hour of spontaneous imbibition.

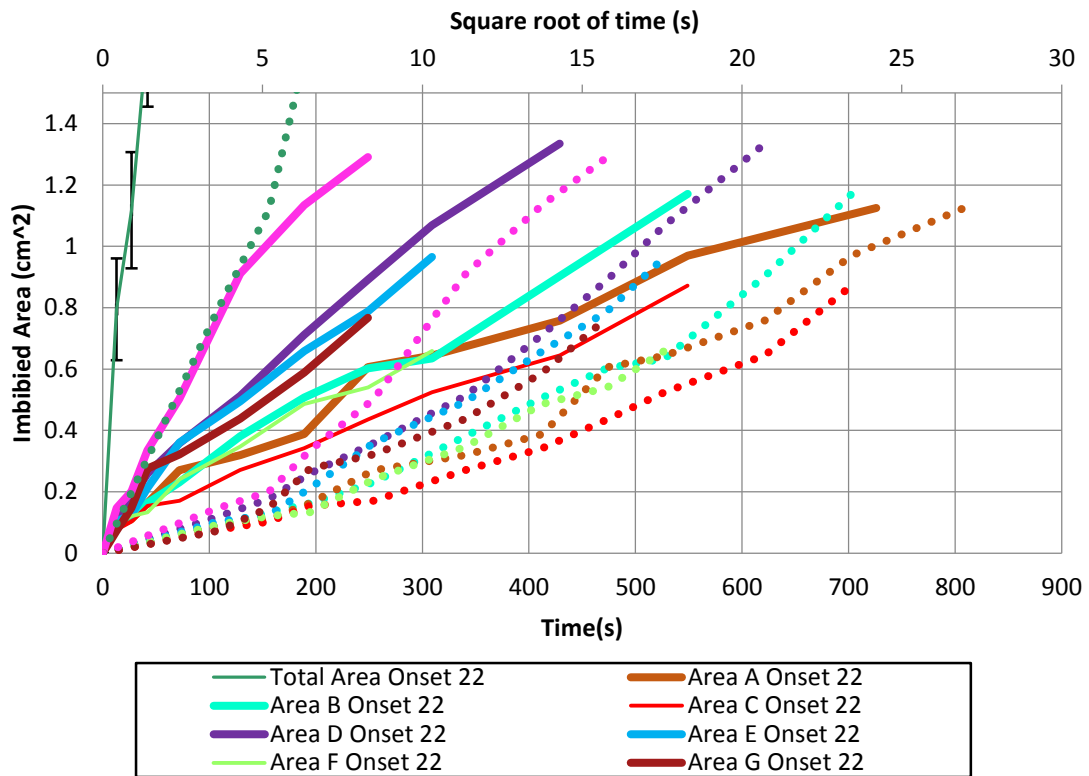


Figure 61: Limited open area spontaneous imbibition experiment Onset 22, with eight open areas. The figure shows the combined and separate size of the eight imbibed areas formed at the eight limited open areas, versus time and the square root of time. The versus time curves are solid lines, and the versus square root of time curves are dotted lines. The vertical gridlines do not connect the two horizontal axes. The vertical axis is adjusted to present the individual areas. The absolute uncertainty in the total area is included.

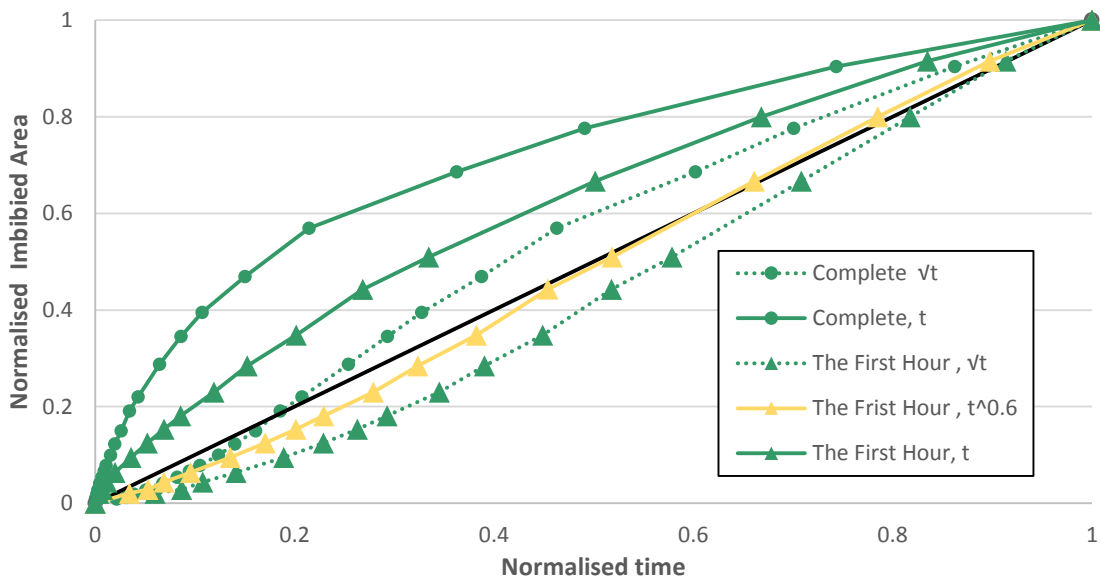


Figure 62: Limited open area spontaneous imbibition experiment Onset 22, with eight open areas. The figure shows normalized imbibed area versus normalized time as solid lines, and versus normalized square root of time as dotted lines. The normalization is with respect to the time for delamination (round markers) and for the first hour of the experiment (triangular markers). The yellow line is a fitted curve showing that the imbibed area is linear with the time $t^{0.8}$ for the first hour of spontaneous imbibition.

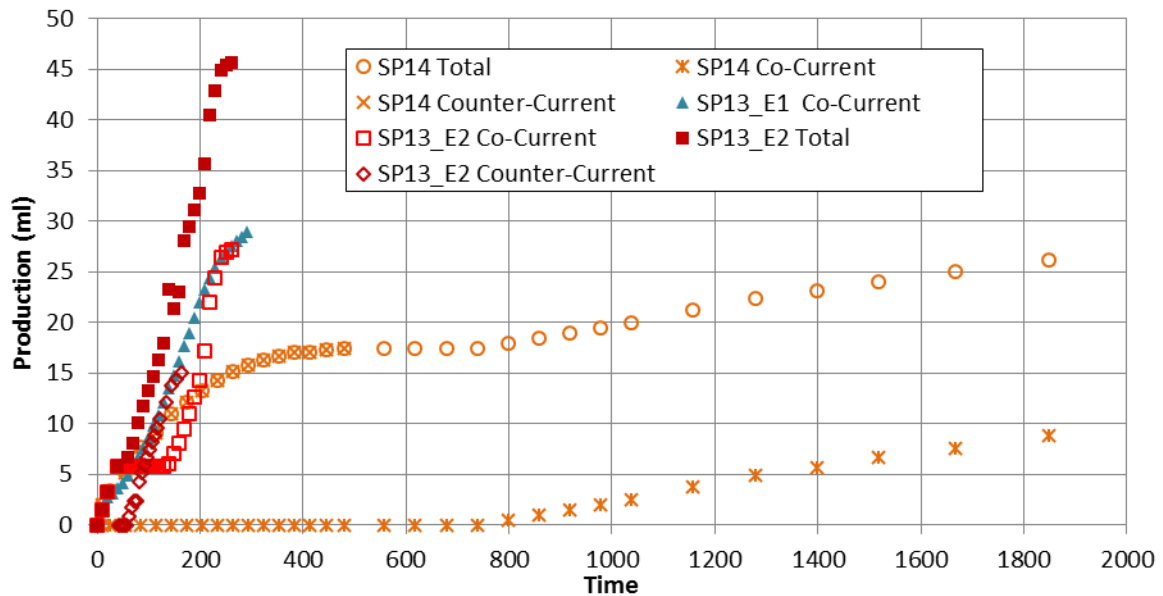


Figure 63: Produced volume of non-wetting phase during spontaneous imbibition into the two collapsed sand packs. Two spontaneous imbibition experiments were performed on sand pack SP13. Continuously measurements of counter-current production during the spontaneous imbibition process SP13_E1 was not performed, the total counter-current production was 19.0 ml and the total production including co- and counter- production was 44.4 ml.

Table 12: Overview of additional measurements from the imbibition tubes.

Experiment	Weight Sand [g] ±0.01	Pore Volume * [ml]	Volume Drainage * [ml] ±0.05	Volume Co- currently [ml] ±0.05	Volume Counter- currently [ml] ±0.05	Volume Total * [ml] ±0.05
SP2	254.2	62.33		52.5	6.4	46.1
SP3	251.21	59.49		49.9	0	49.9
SP4	260.17	62.94		46.5	2	48.5
SP5	259.61	63.93		36.3	0	36.3
SP6	256.27	61.98		47.5	0	47.5
SP7	250.67	60.67		49.7	0	49.7
SP8	258.37	59.70	44.9			
SP9	217	65.18	45.5	54.7	3.6	54.8
SP10_E1	225	64.61	46.0	43.3	3.5	43.3
SP10_E2	225	64.61	50.4	37.5	3.5	37.5
SP11	210	68.425	52.8	30.4	3.5	30.4
SP12	232	60.65	44.8	28.9	19.0	44.4
SP13_E1	232	60.65	52.3	27.2	18.5	42.2
SP13_E2	230	62.54		17.4	12.3	26.2
SP14	222	62.64				
SP15	78.9	23.77	18.4	25.3	3.5	25.3
SP16_E1	78.9	23.77		13.9	3.5	13.9
SP16_E2	79	25.2	18.9	26.0	3.5	26.0
SP17_E1	79	25.2	45.5	7.0	3.5	7.0
SP17_E2	217	65.18	46.0	54.7	3.6	54.8

* Dead volume is subtracted.

BIBLIOGRAPHY

- Akin, S., Schembre, J., Bhat, S. and Kovscek, A., 2000. Spontaneous imbibition characteristics of diatomite. *Journal of Petroleum Science and Engineering*, 25(3): 149-165.
- Anderson, W.G., 1986a. Wettability Literature Survey- Part 1: Rock/oil/brine interactions and the effects of core handling on wettability. *Journal of Petroleum Technology*, 38(11): 1125-1144.
- Anderson, W.G., 1986b. Wettability Literature Survey- Part 2: Wettability Measurement. *Journal of Petroleum Technology*, 38(11): 1246-1262.
- Anderson, W.G., 1987. Wettability Literature Survey- Part 5: The Effects of Wettability on Relative Permeability. *Journal of Petroleum Technology*, 39(11): 1453-1468.
- Aslannejad, H. et al., 2017. Characterizing the hydraulic properties of paper coating layer using FIB-SEM tomography and 3D pore-scale modeling. *Chemical Engineering Science*, 160: 275-280.
- Baldwin, B.A. and Spinler, E.A., 2002. In situ saturation development during spontaneous imbibition. *Journal of Petroleum Science and Engineering*, 35(1–2): 23-32.
- Behbahani, H. and Blunt, M.J., 2005. Analysis of Imbibition in Mixed-Wet Rocks Using Pore-Scale Modeling. *SPE Journal*, 10(4): 466-474.
- Behbahani, H.S., Di Donato, G. and Blunt, M.J., 2006. Simulation of counter-current imbibition in water-wet fractured reservoirs. *Journal of Petroleum Science and Engineering*, 50(1): 21-39.
- Beuther, P.D., Veith, M.W. and Zwick, K.J., 2010. Characterization of Absorbent Flow Rate in Towel and Tissue. *Journal of Engineered Fibers and Fabrics*, 5(2): 1-7.
- Bourbiaux, B.J., 2009. Understanding the Oil Recovery Challenge of Water Drive Fractured Reservoirs, International Petroleum Technology Conference, Doha, Qatar, 7-9 December.
- Bourbiaux, B.J. and Kalaydjian, F.J., 1990. Experimental Study of Cocurrent and Countercurrent Flows in Natural Porous Media. *SPE Reservoir Engineering*, 5(3).
- Brown, R.J.S. and Fatt, I., 1956. Measurements Of Fractional Wettability Of Oil Fields' Rocks By The Nuclear Magnetic Relaxation Method, Fall Meeting of the Petroleum Branch of AIME. Society of Petroleum Engineers, Los Angeles, California, 14-17 October.
- Donaldson, E.C., Chilingarian, G.V. and Yen, T.F., 1989. Enhanced oil recovery, II: Processes and operations. Elsevier.
- Donaldson, E.C., Thomas, R.D. and Lorenz, P.B., 1969. Wettability Determination and Its Effect on Recovery Efficiency. *SPE Journal*, 9(1): 13-20.
- Dong, M., Dullien, F.A., Dai, L. and Li, D., 2005. Immiscible displacement in the interacting capillary bundle model Part I. Development of interacting capillary bundle model. *Transport in Porous media*, 59(1): 1-18.

- Fernø, M.A., Haugen, Å., Brattekkås, B., Mason, G. and Morrow, N.R., 2015a. Quick And Affordable SCAL: Spontaneous Core Analysis, International Symposium of the Society of Core Analysts. The Society of Core Analysts, St. John's, Canada.
- Fernø, M.A., Haugen, Å., Brattekkås, B., Morrow, N.R. and Mason, G., 2015b. Spontaneous Imbibition Revisited: A New Method to Determine K_r and P_c by Inclusion of the Capillary Backpressure, 18th European Symposium on Improved Oil Recovery, EAGE, Dresden, Germany, 14-16 April.
- Fernø, M.A., Haugen, Å. and Graue, A., 2011. Wettability effects on the matrix–fracture fluid transfer in fractured carbonate rocks. *Journal of Petroleum Science and Engineering*, 77(1): 146-153.
- Fernø, M.A. et al., 2013. Magnetic resonance imaging of the development of fronts during spontaneous imbibition. *Journal of Petroleum Science and Engineering*, 101: 1-11.
- Fernø, M.A., Torsvik, M., Haugland, S. and Graue, A., 2010. Dynamic laboratory wettability alteration. *Energy & Fuels*, 24(7): 3950-3958.
- Fischer, H. and Morrow, N.R., 2006. Scaling of oil recovery by spontaneous imbibition for wide variation in aqueous phase viscosity with glycerol as the viscosifying agent. *Journal of Petroleum Science and Engineering*, 52(1–4): 35-53.
- Forrest, C.F., 1993. *The Reservoir Engineering Aspects of Waterflooding*, 3. American Institute of Mining, Metallurgical and Petroleum Engineers, 134 pp.
- Gess, J.M., 1996. The sizing of paper with rosin and alum at acid pHs. In: J.C. Roberts (Editor), *Paper Chemistry* Chapman & Hall, 120-139, London, UK pp. 120-139.
- Graue, A., Aspenes, E., Bognø, T., Moe, R.W. and Ramsdal, J., 2002. Alteration of wettability and wettability heterogeneity. *Journal of Petroleum Science and Engineering*, 33(1–3): 3-17.
- Haugen, Å., Fernø, M., Mason, G. and Morrow, N., 2015. The Effect of Viscosity on Relative Permeabilities Derived from Spontaneous Imbibition Tests. *Transport in Porous Media*, 106(2): 383-404.
- Haugen, Å., Fernø, M.A., Mason, G. and Morrow, N.R., 2014. Capillary pressure and relative permeability estimated from a single spontaneous imbibition test. *Journal of Petroleum Science and Engineering*, 115: 66-77.
- Haugland, H.K., 2016. *Spontaneous Imbibition in Sand*, University of Bergen.
- Kazemi, H., Gilman, J.R. and Elsharkawy, A.M., 1992. Analytical and Numerical Solution of Oil Recovery From Fractured Reservoirs With Empirical Transfer Functions *SPE Reservoir Engineering*, 7(2): 219-227.
- Kirby, B., 2010. *Micro- and nanoscale fluid mechanics : transport in microfluidic devices*. Cambridge University Press, New York, 536 pp.
- Krumbein, W.C. and Monk, G.D., 1942. Permeability as a Function of the Size Parameters of Unconsolidated Sand. 151(1): 153-163.
- Leverett, M.C., 1941. Capillary Behavior in Porous Solids. 142(1): 152-169.

- Li, Y., Mason, G., Morrow, N.R. and Ruth, D.W., 2009. Capillary Pressure at the Imbibition Front During Water–Oil Counter-Current Spontaneous Imbibition. *Transport in Porous Media*, 77(3): 475-487.
- Li, Y., Morrow, N.R. and Ruth, D., 2003. Similarity solution for linear counter-current spontaneous imbibition. *Journal of Petroleum Science and Engineering*, 39(3–4): 309-326.
- Li, Y., Ruth, D., Mason, G. and Morrow, N.R., 2006. Pressures acting in counter-current spontaneous imbibition. *Journal of Petroleum Science and Engineering*, 52(1–4): 87-99.
- Ma, S., Morrow, N.R. and Zhang, X., 1997. Generalized scaling of spontaneous imbibition data for strongly water-wet systems. *Journal of Petroleum Science and Engineering*, 18(3): 165-178.
- Ma, S., Zhang, X. and Morrow, N.R., 1995. Influence of Fluid Viscosity On Mass Transfer Between Rock Matrix And Fractures, 46th Annual Technical Meeting of The Petroleum Society of CIM. Petroleum Society of Canada, , Alberta, Canada, 14-17 May.
- Mark, A. et al., 2012. Modeling and simulation of paperboard edge wicking. *Nordic Pulp & Paper Research Journal*, 27(2): 397-402.
- Masch, F.D. and Denny, K.J., 1966. Grain size distribution and its effect on the permeability of unconsolidated sands. *Water Resources Research*, 2(4): 665-677.
- Mason, G., Fernø, M.A., Haugen, Å., Morrow, N.R. and Ruth, D.W., 2012. Spontaneous counter-current imbibition outwards from a hemi-spherical depression. *Journal of Petroleum Science and Engineering*, 90–91: 131-138.
- Mason, G. et al., 2010. Oil production by spontaneous imbibition from sandstone and chalk cylindrical cores with two ends open. *Energy & Fuels*, 24(2): 1164-1169.
- Mason, G., Fischer, H., Morrow, N.R. and Ruth, D.W., 2009a. Spontaneous counter-current imbibition into core samples with all faces open. *Transport in porous media*, 78(2): 199-216.
- Mason, G., Fischer, H., Morrow, N.R., Ruth, D.W. and Wo, S., 2009b. Effect of sample shape on counter-current spontaneous imbibition production vs time curves. *Journal of Petroleum Science and Engineering*, 66(3–4): 83-97.
- Mason, G. and Morrow, N.R., 2013. Developments in spontaneous imbibition and possibilities for future work. *Journal of Petroleum Science and Engineering*, 110: 268-293.
- Mattax, C.C. and Kyte, J.R., 1962. Imbibition Oil Recovery from Fractured, Water-Drive Reservoir. 2(2): 177-184.
- McCabe, W.L., Smith, J.C. and Harriot, P., 2005. *Unit Operations Of Chemical Engineering*. Mc Graw Hill, Singapore
- McCaffery, F.G., 1973. The effect of wettability on relative permeability and imbibition in porous media, University of Calgary.
- Meng, Q., Liu, H. and Wang, J., 2015. Entrapment of the Non-wetting Phase during Co-current Spontaneous Imbibition. *Energy & Fuels*, 29(2): 686-694.

- Meng, Q., Liu, H., Wang, J. and Liu, H., 2017. Effect of fluid viscosity on correlation of oil recovery by linear counter-current spontaneous imbibition. *Journal of Petroleum Science and Engineering*, 151: 341-347.
- Meng, Q., Liu, H., Wang, J. and Pang, Z., 2016. Asymmetry Characteristics of Oil Production by Spontaneous Imbibition from Cores with Two Ends Open. *Transport in Porous Media*, 113(3): 735-751.
- Mirzaei-Paiaman, A., Kord, S., Hamidpour, E. and Mohammadzadeh, O., 2017. Scaling one- and multi-dimensional co-current spontaneous imbibition processes in fractured reservoirs. *Fuel*, 196: 458-472.
- Morrow, N.R., Ma, S., Zhou, X. and Zhang, X., 1994. Characterization of Wettability From Spontaneous Imbibition Measurements, 45th annual technical meeting of the Petroleum Society of CIM, Calgary, Canada, 12-15 June.
- Morrow, N.R. and Mason, G., 2001. Recovery of oil by spontaneous imbibition. *Current Opinion in Colloid & Interface Science*, 6(4): 321-337.
- Morrow, N.R. and McCaffery, F., 1978. *Displacement studies in uniformly wetted porous media*, 289. Academic Press, New York City.
- Morrow, N.R. and Xie, X., 2001. Oil Recovery By Spontaneous Imbibition From Weakly Water-wet Rocks. 42(2): 313-322.
- Nutting, P.G., 1925. Chemical Problems in the Water Driving of Petroleum from Oil Sands. *Industrial & Engineering Chemistry*, 17(10): 1035-1036.
- Oko, A., 2014. Spontaneous imbibition and colloidal aspects of inkjet printing. Doctoral Thesis, KTH Royal Institute of Technology, 89 pp.
- Pooladi-Darvish, M. and Firoozabadi, A., 2000. Cocurrent and countercurrent imbibition in a water-wet matrix block. *SPE Journal*, 5(01): 3-11.
- Rangel-German, E.R. and Kovscek, A.R., 2002. Experimental and analytical study of multidimensional imbibition in fractured porous media. *Journal of Petroleum Science and Engineering*, 36(1-2): 45-60.
- Salathiel, R.A., 1973. Oil Recovery by Surface Film Drainage In Mixed-Wettability Rocks. *Journal Of Petroleum Engineering*, 25(10): 1216-1224.
- Salminen, P., 1988. Studies of water transport in paper during short contact times, Laboratory of Paper Chemistry. Department of Chemical Engineering. Åbo Akademi, Åbo Akademi.
- Schmid, K.S. and Geiger, S., 2012. Universal scaling of spontaneous imbibition for water-wet systems. *Water Resources Research*, 48(3): 13.
- Shaw, D.J., 1992. 4 - Liquid-gas and liquid-liquid interfaces, *Introduction to Colloid and Surface Chemistry (Fourth Edition)*. Butterworth-Heinemann, Oxford, pp. 64-114.

- Unsal, E., Mason, G., Morrow, N. and Ruth, D., 2007. Co-current and counter-current imbibition in independent tubes of non-axisymmetric geometry. *Journal of colloid and interface science*, 306(1): 105-117.
- Vabø, T., 2016. Viscosity Effects on Imbibition Rate and Front Behavior during Co-Current Spontaneous Imbibition in Unconsolidated Porous Media, University of Bergen.
- Viksund, B., Morrow, N., Ma, S., Wang, W. and Graue, A., 1998. Initial water saturation and oil recovery from chalk and sandstone by spontaneous imbibition, *Proceedings, 1998 International Symposium of Society of Core Analysts*, . Citeseer, The Hague, Netherlands.
- Wardlaw, N.C. and Yu, L., 1988. Fluid topology, pore size and aspect ratio during imbibition. *Transport in Porous Media*, 3(1): 17-34.
- Washburn, E.W., 1921. The dynamics of capillary flow. *Physical review*, 17(3): 273-283.
- Wickramathilaka, S., Mason, G., Morrow, N.R., Howard, J.J. and Stevens, J.C., 2010. Magnetic Resonance Imaging Of Oil Recovery During Spontaneous Imbibition From Cores With Two-Ends Open Boundary Condition *International Symposium On Reservoir Wettability*. Society of Core Analysts, Calgary ,Canada, 6-9 September.
- Xiao, J., Stone, H.A. and Attinger, D., 2012. Source-like Solution for Radial Imbibition into a Homogeneous Semi-infinite Porous Medium. *Langmuir*, 28(9): 4208-4212.
- Zeppieri, S., Rodríguez, J. and López de Ramos, A.L., 2001. Interfacial Tension of Alkane + Water Systems. *Journal of Chemical & Engineering Data*, 46(5): 1086-1088.
- Zhang, X., Morrow, N.R. and Ma, S., 1996. Experimental Verification of a Modified Scaling Group for Spontaneous Imbibition. *SPE Reservoir Engineering*, 11(4): 280-285.